

Large Eddy Simulations of high Reynolds number Complex Flows with Synthetic Inlet Turbulence

by

Sunil Shankarrao Patil

A dissertation submitted to the faculty of
Virginia Polytechnic Institute and State University
in partial fulfillment of the degree of

Doctor of Philosophy

in

Mechanical Engineering

Dr. Danesh K. Tafti, Chair
Dr. Srinath V. Ekkad
Dr. Mark R. Paul
Dr. Roger L. Simpson
Dr. Uri Vandsburger

January 24, 2011
Blacksburg, Virginia, USA

Keywords: Large-eddy simulation, wall layer modeling, synthetic eddy method

Sunil Patil © 2011

Abstract

Large Eddy Simulations of high Reynolds number Complex Flows with Synthetic Inlet Turbulence

Sunil Shankarrao Patil

The research was motivated by the desire to use Large Eddy Simulations (LES) to calculate liner heat transfer in industrial scale gas turbine combustors, which operate at high Reynolds numbers and high Swirl numbers. LES has several challenges which need to be surmounted for general application to complex high Reynolds number turbulent flows. The primary challenge in wall bounded flows is the need for very fine grids in the vicinity of walls, which makes LES impractical at high Reynolds numbers. An additional challenge is the accurate representation of inlet turbulent conditions for developing flows such that the computational domain size is limited to the immediate region of interest. The generalization of solutions to surmount these issues in complex geometries and grids is yet another challenge.

To meet these challenges, a novel formulation, implementation, and validation of a two layer velocity and temperature zonal wall model along with the implementation of the synthetic eddy method in a generalized coordinate system LES framework is presented in this thesis. The wall model greatly alleviates the grid requirements, whereas the synthetic eddy method provides accurate turbulent inlet boundary conditions. The methods are validated in turbulent channel flow up to a Reynolds number of 2×10^6 , a backward facing step at $Re=40,000$, before application to a model swirl combustor at $Re=20,000$ with a Swirl number of 0.43 and flow and heat transfer in an industrial scale can combustor at $Re=80,000$ and Swirl number of 0.7. The integrated zonal

near wall approach for velocity and temperature is then successfully used to investigate flow and heat transfer in a statistically three-dimensional flow of a ribbed duct passage used for the internal cooling of turbine blades. The zonal wall model is further modified to take in to account the effects of surface roughness and successfully used to investigate flow in a rod roughened channel at high Reynolds numbers up to 60,000.

In all cases it is shown that the zonal wall model used with the synthetic eddy method for inlet turbulence generation can result in large savings in computational cost without any significant loss in accuracy when compared to wall resolved LES and experiments. In a turbulent channel flow at $Re=45,000$, computational complexity was reduced by a factor of 285 using wall modeled LES, whereas in a statistically three-dimensional flow and heat transfer in a ribbed duct, at $Re=20,000$, the computational complexity was reduced by a factor between 60 and 140. In a swirl dominated can combustor at $Re=20,000$, the reduction was more modest at a factor of 9.

To Aai and Baba

Acknowledgements

Working on my PhD dissertation was a challenging experience. I would like to thank first my advisor, Dr. Danesh Tafti. He consistently motivated me towards success and provided support when needed. He was always there for us in the lab and I am grateful for his guidance in making this dissertation a success.

I am thankful to Solar Turbines, Inc. for funding this research. I also appreciate feedback and support from Hee-Koo Moon, Partha Dutta, Yong Kim, and Ram Sreenivasan (Design Engineers from Solar Turbines, Inc., San Diego, CA) during Dry Low Emission combustor investigation. The LES calculations were performed on Virginia Tech's Terascale computing facility, System-X. The support is gratefully acknowledged.

I would like to thank my committee members Dr. Srinath Ekkad, Dr. Mark Paul, Dr. Roger Simpson, and Dr. Uri Vandsburger for providing constructive feedback. I would like to thank all my lab mates: Mohammad, Pradeep, Sai, Naresh, Jose, Kohei, Amit, Jonathan, Nagi, Surjo, Vivek, Sukhi, and Kevin for making the lab a fun place to work.

I highly appreciate work of Santosh Abraham, and Teddy Sedalor for carrying out experimental validation of highly complex gas turbine combustor geometries which I numerically investigated. Special thanks to Dr. Ekkad, who guided the whole experimental investigation and also helped in critically reviewing 3 conference papers and 2 journal papers which I wrote with him.

I also thank all my roommates: Manas, Mohit, Arpit, and Vikram. They made my stay at Blacksburg enjoyable with many pleasant memories to cherish in future. I greatly enjoyed their company and I am thankful for their friendship.

Finally I would like to thank my family: Aai, Baba, Tai, and Dada. They offered me unconditional love and the best support one can ever wish for.

Table of Contents

| | |
|--|-----|
| Abstract..... | iii |
| Acknowledgements | v |
| Table of Contents | vii |
| List of Figures | x |
| List of Tables | xv |
| Chapter 1 Background, Motivation and Objectives | 1 |
| Chapter 2 RANS Investigation of Convective Heat Transfer in Dry Low Emission (DLE) Gas Turbine Combustors | 12 |
| 2.1 Computational Methodology..... | 13 |
| 2.2 Results..... | 14 |
| 2.2.1 Validation of Computational Model | 14 |
| 2.2.2 Flow-field Characteristics..... | 17 |
| 2.2.3 Effect of Reynolds number..... | 18 |
| 2.2.4 Effect of Swirl Strength..... | 20 |
| 2.3 Conclusions | 22 |
| 2.4 Tables..... | 24 |
| 2.5 Figures | 26 |
| Chapter 3 Governing Equations and Numerical Implementation | 38 |
| 3.1 Governing Equations and Numerical Method | 38 |
| 3.2 Numerical Implementation and Algorithm | 41 |
| 3.3 Parallel Implementation | 43 |
| 3.4 Wall Modeling..... | 44 |
| 3.4.1 Modified Two Layer Model for Complex Geometries | 47 |
| 3.4.2 Zonal Two Layer Heat Transfer Model..... | 50 |
| 3.5 Turbulent Inlet Boundary Condition..... | 52 |
| 3.5.1 Synthetic Eddy Method Formulation | 55 |
| 3.6 Figures | 57 |
| Chapter 4 Validation of Wall Model and Synthetic Eddy Method | 59 |
| 4.1 Fully Developed Turbulent Channel Flow..... | 59 |
| 4.2 Developing Turbulent Channel Flow..... | 61 |

| | |
|--|-----|
| 4.3 Flow over a Backward Facing Step | 62 |
| 4.4 Summary and Conclusions | 66 |
| 4.5 Tables | 67 |
| 4.6 Figures | 68 |
| Chapter 5 Large Eddy Simulations of Swirling Flows in Gas Turbine Combustors..... | 77 |
| 5.1 Introduction | 78 |
| 5.2 Experimental Swirl Combustor | 80 |
| 5.2.1 Computational Domain | 81 |
| 5.2.2 Inlet Flow Profiles..... | 82 |
| 5.2.3 Grid Resolution..... | 82 |
| 5.2.4 Effect of Inflow Boundary Conditions | 84 |
| 5.2.5 Flow Predictions | 85 |
| 5.3 Hybrid RANS-LES Simulation of an Industrial Scale Gas Turbine Combustor..... | 89 |
| 5.3.1 Computational Domain | 89 |
| 5.3.2 Inlet Flow Profiles..... | 90 |
| 5.3.3 Reynolds number 50,000..... | 91 |
| 5.3.4 Reynolds number 80,000..... | 95 |
| 5.4 Summary and Conclusions | 98 |
| 5.5 Tables..... | 100 |
| 5.6 Figures | 101 |
| Chapter 6 Large Eddy Simulation with Zonal near Wall Treatment of Rib Roughened Ducts and Channels | 116 |
| 6.1 Internal Cooling Rib Ducts | 117 |
| 6.1.1 Introduction | 117 |
| 6.1.2 Computational Domain | 119 |
| 6.1.3 Grid resolution | 119 |
| 6.1.4 Computational Details..... | 121 |
| 6.1.5 Ribbed Duct Flow at $Re_{DH}=20,000$ | 122 |
| 6.1.6 Ribbed Duct Flow at $Re_{DH}=60,000$ | 126 |
| 6.2 Two Layer Wall Model for Large Eddy Simulations of Flow over Rough surfaces..... | 129 |
| 6.2.1 Background and Introduction | 129 |

| | |
|---|-----|
| 6.2.2 Roughness Modification to Two Layer Wall Model..... | 134 |
| 6.2.3 Computational Details..... | 135 |
| 6.2.4 Mean Flow Velocity Prediction..... | 136 |
| 6.2.5 Reynolds Stress Prediction..... | 136 |
| 6.3 Conclusions..... | 139 |
| 6.4 Tables..... | 141 |
| 6.5 Figures..... | 144 |
| Chapter 7 Summary and Conclusions..... | 158 |
| Appendix A Nomenclature..... | 161 |
| Appendix B Large Eddy Simulation of in Fully Developed Turbulent Channel Flow with Heat Transfer at $Re_\tau=590$ | 164 |
| Appendix C Large Eddy Simulations of Confined Weakly Swirling flows with Synthetic Inlet Turbulence..... | 166 |
| Appendix D Detailed Flow Predictions in Experimental Swirl Combustor..... | 172 |
| Appendix E Additional Flow Predictions in Backward Facing Step..... | 178 |
| Appendix F Simulation Code GenIDLEST..... | 181 |

List of Figures

| | |
|--|----|
| Figure 2.1 Computational domain consisting periodic segment (sector angle = 18°) of swirl nozzle and can combustor | 26 |
| Figure 2.2 Computational domain consisting of swirl nozzle and periodic segment (sector angle = 30°) of annular combustor | 26 |
| Figure 2.3 Computational grid details for annular combustor configuration. (a) mesh on the swirler vanes (b) mesh in the passage between the two vanes (c) head on view of overall mesh in the swirler and annular combustor | 28 |
| Figure 2.4 Comparison of numerical predictions for can combustor liner wall heat transfer augmentation with experiments using different turbulence models at $Re=50,000$ | 29 |
| Figure 2.5 Nusselt number augmentation for $Re=50,000$ and $Re= 80,000$ along the can combustor liner wall | 29 |
| Figure 2.6 Nusselt number augmentation on (a) concave liner wall, and (b) convex liner wall of the annular combustor..... | 30 |
| Figure 2.7 (a) Flow streamlines (b) contours of normalized axial velocity, and (c) contours of normalized turbulent kinetic energy in a meridional plane in the can combustor..... | 31 |
| Figure 2.8 Axial vorticity iso-contour (value = 1000) in can combustor colored with axial velocity..... | 32 |
| Figure 2.9 (a) Flow streamlines, and (b) contours of normalized axial velocity in a meridional plane in the annular combustor | 33 |
| Figure 2.10 Effect of Reynolds number on can combustor liner wall heat transfer augmentation | 34 |
| Figure 2.11 Variation of peak heat transfer augmentation ratio on can combustor liner wall with Reynolds number | 34 |
| Figure 2.12 Variation of normalized turbulent kinetic energy with Reynolds number near shear layer impingement location on can combustor liner wall..... | 35 |
| Figure 2.13 Flow streamlines in can combustor for (a) $Re = 80,000$ and (b) $Re = 500,000$ | 35 |

| | |
|--|-----|
| Figure 2.14 Variation in normalized turbulent kinetic energy with increase in Reynolds number near shear layer impingement location on the annular combustor liner wall | 36 |
| Figure 2.15 Generic representation of swirler-combustor configuration..... | 36 |
| Figure 2.16 Variation of peak heat transfer augmentation with Reynolds number for can and annular combustor..... | 37 |
| Figure 3.1 Virtual grid for wall model, embedded in LES grid (W represent wall node, and P the off wall outer LES node)..... | 57 |
| Figure 4.1 Turbulent channel flow results with two layer wall model for $Re_\tau=590$ (a) mean velocity predictions (b) turbulence statistics..... | 68 |
| Figure 4.2 Turbulent channel flow results with two layer wall model for $Re_\tau=2000$ (a) mean velocity predictions (b) turbulence statistics..... | 69 |
| Figure 4.3 Mean non-dimensional temperature prediction with two layer wall model for $Re_\tau=590$ | 70 |
| Figure 4.4 Mean velocity prediction with two layer wall model for $Re_\tau=20,000$ | 70 |
| Figure 4.5 Profiles of (a) mean streamwise velocity, and (b) Reynolds stresses at the inlet plane | 71 |
| Figure 4.6 Evolution of Reynolds stresses in streamwise direction | 72 |
| Figure 4.7 Evolution of wall shear stress along the streamwise direction on the channel wall.... | 73 |
| Figure 4.8 Backward facing step geometry of Driver and Seegmiller [68]..... | 74 |
| Figure 4.9 Prediction of mean streamwise velocity at various axial locations..... | 74 |
| Figure 4.10 Predictions of Reynolds stresses (a) u_{rms} (scale 1:30) (b) v_{rms} (scale 1:30) (c) Reynolds shear stress (scale 1:500) | 75 |
| Figure 4.11 Skin friction predictions downstream of the step expansion..... | 76 |
| Figure 4.12 Mean flow streamlines in the computational domain..... | 76 |
| Figure 5.1 Computational domain for experimental swirl combustor (a) sketch with dimensions (R_1 is the reference length scale, $R_2=1.94R_1$, $H=0.94R_1$) (b) frontal view, and (c) side view of the mesh in 3D computational mesh..... | 101 |

| | |
|---|-----|
| Figure 5.2 Measured and predicted mean velocity and turbulent stress profiles at inlet of the computational domain ($x/H=-2.1$) | 102 |
| Figure 5.3 Grid sensitivity study : Time averaged mean swirl velocity at streamwise location $x/H=2.1$ ($Re=20,000$ $S=0.43$) | 103 |
| Figure 5.4 Effect of inlet turbulence : Time averaged profiles of axial velocity (scale 1:1), swirl velocity (scale 1:1), variance of axial velocity (scale 1:4), and variance of swirl velocity (scale 1:10) at representative axial location ($x/H=2.1$) | 104 |
| Figure 5.5 Time averaged profiles of (from left to right) axial velocity ($\langle u \rangle / U_b$), swirl velocity ($\langle u_\theta \rangle / U_b$), variance of axial velocity ($\langle u'u' \rangle / U_b^2$), variance of swirl velocity ($\langle u'_\theta u'_\theta \rangle / U_b^2$), Reynolds shear stress ($\langle u'u'_r \rangle / U_b^2$) for $Re=20,000$ and $S=0.43$ at (a) $x/H=0.17$, (b) $x/H=2.1$, and (c) $x/H=6.3$ | 105 |
| Figure 5.6 Instantaneous streamlines in (a) azimuthal plane ($z/H=0$), (b) $x/H=1$, and (c) $x/H=5$ | 106 |
| Figure 5.7 Schematics of experimental setup of Patil et al. [82]. From left to right: swirler, nozzle extension channel, can combustor | 107 |
| Figure 5.8 3D computational domain for LES of an industrial can combustor (a) frontal view, and (b) side view of the 3D mesh | 107 |
| Figure 5.9 Profiles of mean velocity (normalized by bulk mean velocity in combustor) and turbulent kinetic energy (normalized by square of bulk mean velocity in combustor) at the inlet plane of the LES computational domain ($x/H=-0.5$) | 108 |
| Figure 5.10 (a) Mean flow streamlines in the azimuthal plane ($z=0$) (b) contours of axial velocity (normalized by bulk mean combustor velocity) in azimuthal plane ($z=0$) | 109 |
| Figure 5.11 Variation of normalized mean velocity components and Reynolds stresses at (a) $x/D=0.1$ (b) $x/D=0.45$ (c) $x/D=2$ (scale 6:1) | 110 |
| Figure 5.12 Heat transfer augmentation ratio (Nu/Nu_0) along the liner wall | 111 |
| Figure 5.13 (a) Mean flow streamlines in the azimuthal plane ($z=0$) (b) contours of axial velocity (normalized by bulk mean combustor velocity) in azimuthal plane ($z=0$) | 112 |

| | |
|--|-----|
| Figure 5.14 Variation of mean velocity components and Reynolds stresses at (a) $x/D=0.1$ (b) $x/D=0.45$ (c) $x/D=2$ (scale 6:1) | 113 |
| Figure 5.15 Normalized Reynolds normal stresses and axial velocity in the shear layer near the peak heat transfer location | 114 |
| Figure 5.16 Heat transfer augmentation ratio (Nu/Nu_0) along the liner wall | 115 |
| Figure 6.1 Computational domain for ribbed duct..... | 144 |
| Figure 6.2 Mean flow streamline distribution in the z-symmetry ($z=0.5$) plane | 145 |
| Figure 6.3 Contours of mean spanwise flow velocity near smooth wall ($z=0.05$) | 145 |
| Figure 6.4 Reynolds stresses at center plane ($z=0.5$) ($Re=20,000$) | 146 |
| Figure 6.5 Turbulent kinetic energy at center plane ($z = 0.5, x'/e=4.5$)..... | 147 |
| Figure 6.6 Contours of Nusselt augmentation on (a) smooth wall, and ribbed wall, and (b) ribs | 148 |
| Figure 6.7 Comparison of Nusselt augmentation with experimental data of Rau at al. [99] on (a) ribbed wall at center plane, $y=0, z=0.5$ (b) smooth wall at $e/2$ upstream of the rib, $z=0, x=0.4$ | 149 |
| Figure 6.8 Mean flow streamline distribution in the z-symmetry plane ($z=0.5$) | 150 |
| Figure 6.9 Reynolds stresses at center plane of the duct ($z = 0.5, x'/e = 8.5$)..... | 150 |
| Figure 6.10 Turbulent kinetic energy at center plane of the duct ($z = 0.5, x'/e=8.5$) | 151 |
| Figure 6.11 Comparison of Nusselt augmentation with experimental data of Han at al. [100] at center plane of the duct ($z=0.5, y=0$) | 151 |
| Figure 6.12 Contours of Nusselt augmentation on smooth wall, rib, and ribbed wall | 152 |
| Figure 6.13 Experimental rod roughened geometry of Bakken et al. [102] | 152 |
| Figure 6.14 Comparison of predicted mean flow velocity from WMLES with experimental data of Bakken et al. [102] and smooth log law ($Re_\tau=600$)..... | 153 |
| Figure 6.15 Comparison of predicted mean flow velocity from WMLES with experimental data of Bakken et al. [102] ($Re_\tau=1200$) | 153 |
| Figure 6.16 Comparison of predicted mean flow velocity from WMLES with experimental data of Bakken et al. [102] ($Re_\tau=3200$) | 154 |

| | |
|--|-----|
| Figure 6.17 Comparison of predicted mean flow velocity from WMLES with experimental data of Bakken et al. [4] ($Re_{\tau}=6000$) | 154 |
| Figure 6.18 Skin friction coefficient variation with Reynolds number | 155 |
| Figure 6.19 Reynolds normal stress and shear stress distribution ($Re_{\tau}=600$)..... | 155 |
| Figure 6.20 Reynolds normal stress and shear stress distribution ($Re_{\tau}=1200$)..... | 156 |
| Figure 6.21 Reynolds normal stress and shear stress distribution ($Re_{\tau}=3200$)..... | 156 |
| Figure 6.22 Reynolds normal stress and shear stress distribution ($Re_{\tau}=6000$)..... | 157 |

List of Tables

| | |
|---|-----|
| Table 2.1 Numerical calculation summary | 24 |
| Table 2.2 Boundary conditions | 25 |
| Table 4.1 Turbulent channel flow calculation summary | 67 |
| Table 5.1 Calculation summary for experimental swirl combustor..... | 100 |
| Table 6.1 Ribbed duct calculation summary..... | 141 |
| Table 6.2 Heat transfer and friction data comparison with Rau et al. [99] (Re=20,000) | 142 |
| Table 6.3 Calculation and grid resolution summary for flow in rod roughened channel | 143 |

Chapter 1

Background, Motivation and Objectives

Both the desire for better efficiency and the need for lower emissions have reduced the amount of cooling air that the combustion engineer has available for combustor liner cooling in modern gas turbine engines. As combustors are designed to reduce emissions, there is insufficient liner cooling available as more air is utilized in the premixing process and reaction zones to maintain as low a temperature as possible. Due to this requirement, the effectiveness of backside cooling techniques involving impingement, convection, or surface enhancement techniques becomes more critical (Chin et al. [1], Metzger et al. [2], Andrews et al. [3], Fric et al. [4], Schulz [5], Arellano et al. [6] and Smith and Fahme [7]). Due to longer operating cycles for power turbines, the combustor liner needs to meet durability targets of 30,000 hours. To avoid liner failure from over-heating, it is extremely important to accurately quantify the liner heat load in the lean premixed combustor environment. Also, the cooling techniques for the low NO_x combustor liner require more backside cooling and less or almost no film cooling. The lack of knowledge of the local gas side convective heat transfer distribution on the combustor liner makes effective cooling of liners more difficult. Current industry practice used for liner cooling is based on peak heat load (quantified based on the peak combustion temperature) rather than local near wall conditions. This conservative approach requires very high cooling rates on the liner wall, thus requiring complicated cooling designs and high coolant flow rates. This also creates overcooled and undercooled spots in certain locations resulting in huge thermal gradients and significant thermal stresses. This issue is more complicated considering that the peak heat load estimate itself has significant uncertainty.

Several articles that focus on the development of Dry Low Emissions (DLE) combustors for industrial gas turbine engines have been published. Studies by Smith et al. [8], Vandervort et al. [11], White et al. [12] and Roberts et al. [13] have focused on development of low NO_x combustors with the viewpoint of producing lower emissions. Although the designs of these combustors vary, all of them use minimal film cooling. Arellano et al. [6] presented a study on an effective backside cooling scheme for an ultra-lean premixed combustion system. The augmented backside cooled liner in their study, eliminates film cooling in the combustor primary zone and uses trip strip turbulators along the cold side of the liner to enhance heat transfer and thermal barrier coatings on the gas side liner wall to reduce the heat load. Behrendt et al. [14] recently designed a test rig for the characterization of advanced combustor cooling concepts for gas turbine combustors. Their test rig was intended to allow investigations at elevated pressures and temperatures representing realistic operating conditions of future low emission combustors. Lu et al. [15] recently studied the effect of different swirl angles for a DLE combustor on flow and heat transfer distributions.

Typically, a swirler is used in industrial gas turbines to impart a high degree rotation of flow at the combustor primary zone which helps to promote better air-fuel mixing and to induce a recirculatory flow in the primary zone. During the real lean-burn engine operation, gaseous fuel is injected from a series of fuel nozzles mounted on bluff bodies to premix with main stream intake air. The premixed gaseous fuel-air mixture is then ignited and the flame is stabilized at the recirculation zone behind bluff bodies. Due to the wakes or recirculation vortices, which are caused by turbulent flow boundary layer separation on the surface of the bluff body, the flow

transitions to a highly turbulent state so as to provide more energy to the flow and also to help better air-fuel mixing. Furthermore, the recirculation zone behind the bluff body contributes as a flame stabilizer to help trap the flame at high speed flow conditions.

Most of the studies investigating swirling jet structure involved measurement of mean velocities and turbulence quantities. Gore and Ranz [16] characterized the recirculation zone in swirling flows with varying geometric conditions. Reduction in jet centerline velocity was observed indicating the existence of an axial pressure gradient. They concluded that the jet spread angle is a function of applied swirl. Chigier and Chervinsky [17] also observed the jet spread angle to be a function of applied swirl. Brum and Samuelson [18] reported two-component Laser Doppler Velocimetry (LDV) measurements in an axisymmetric combustor model with coaxial swirling jets. Vu and Gouldin [19] reported hot wire measurements in an axisymmetric combustor. In recirculation zones, tangential velocities were found to be very small while levels of turbulence and dissipation rate were very high. Rhode and Lilley [20] performed mean flow-field studies in axisymmetric combustor geometries with swirl. Various flow-field configurations with different side wall angles and swirl vane angles were investigated to characterize the time-mean streamlines, recirculation zone and regions of high turbulence. The length and width of the recirculation zone was found to increase with increase in swirl vane angle until a critical angle was reached, after which any further increase in swirl shortened the length but further increased the width. The major effect of side wall expansion angle was to shorten the corner recirculation region, with no major effect on the central recirculation region.

Ferrell et al. [21] reported experiments with five-hole pitot probe velocity measurements and flow visualization.

Bailey et al. [22] conducted experimental and numerical simulations to characterize heat transfer on F class combustor liner cooled by impingement jets and cross flow between liner and sleeve. Calculations were performed using various Reynolds Averaged Navier-Stokes (RANS) based turbulence models with different near wall treatments. Raj and Ganeshan [23] studied the effect of various geometric parameters like vane angle, vane number, hub to tip ratio on flow development downstream of the swirler. They characterized swirl flow by the size of the recirculation zone, mass trapped in it and axial pressure drop. Fernando et al. [24], Grinstein and Fureby [25] reported Large Eddy Simulation (LES) studies of flow in swirl combustors. Paik and Sotiropoulos [26] performed detached eddy simulations of moderately high Reynolds numbers turbulent swirl flows through an abrupt expansion.

In summary, considerable work has been done in investigating combustor backside cooling schemes and in understanding the aerodynamics of swirl flow. The research presented in this thesis started with the aspiration to predict the effect of swirling flow on the local convective heat load imposed on combustor liners to support the development of more effective cooling schemes to maintain improve combustor durability with minimal cooling air. The challenge in predicting liner heat transfer in industrial swirl combustors stems from the highly turbulent flows generated by high Swirl numbers greater than 0.6 at high Reynolds numbers between 50,000 to 800,000. The high Reynolds number flows prompted initial calculations with the RANS method which proved to be adequate in predicting the liner heat transfer in comparison to experiments.

The research then attempted to extend this initial success with RANS into the domain of Large-Eddy Simulations which proved to be problematic because of the high grid densities required to accurately resolve the combustor liner boundary layers. The unreasonable near wall grid requirements was further exacerbated by the need to accurately represent the swirl flow entering the combustor requiring that the swirl injector also be included in the LES calculation domain. It became apparent that in order for LES to be a viable tool in predicting combustor liner heat transfer, two critical issues, near wall resolution, and the ability to accurately specify time-dependent turbulent inlet conditions had to be surmounted.

The bulk of this thesis deals with developments in resolving these two issues and is the main contribution of this work. The main objectives, therefore, are to develop wall modeling capabilities within the framework of LES to preempt the dense grids needed in near wall regions at high Reynolds numbers, and to evaluate techniques for the generation for inlet turbulent boundary conditions such that inlet boundaries can be placed in close proximity to regions of interest. While the utility of these developments is clear in combustor liner heat transfer problems, these also have far ranging implications in the prediction of all types of complex turbulent flows.

The thesis is organized as follows:

- Investigation using RANS prediction techniques in high swirl can and annular combustors under representative industrial conditions is carried out in Chapter 2. The combustor and swirler geometries and conditions were provided by Solar Turbines. Different turbulent models are evaluated for predicting high Swirl number flows. The

- location and magnitude of peak heat transfer on the liner wall is investigated and explained in relation to the flow physics, Reynolds number and Swirl number.
- Governing equations and numerical details used for LES simulations are described in Chapter 3. A literature review was conducted on the use of LES wall models and the generation of turbulent inlet boundary conditions. The developments and implementation of these techniques within the framework of the in-house software GenIDLEST is explained.
 - The efficacy of the wall model and inlet turbulence generation is systematically validated in Chapter 4. First, the wall model is tested in a fully-developed channel flow for Reynolds number up to 2×10^6 , followed by validation of the inlet turbulence generation method to generate sustained spatially and temporally correlated turbulence in a developing turbulent channel flow. Finally, both techniques are validated together in a backward facing step geometry at $Re=40,000$.
 - In Chapter 5, swirl dominated flows are revisited in can combustors at high Reynolds numbers with LES. First, the wall model and the inlet turbulence boundary condition are extensively validated against available experimental data in a model can combustor at $Re=20,000$ and a Swirl number of 0.43. The industrial scale can combustor geometry of Solar Turbines is then simulated at $Re=80,000$ and a Swirl number of 0.7. The calculations show excellent agreement with the experimental distribution of liner heat transfer, vindicating the objectives of this research effort.

- Efficacy of the wall modeled LES is further demonstrated in Chapter 6 in a ribbed duct geometry used in internal cooling passages. Two Reynolds numbers are investigated, $Re=20,000$ and $60,000$. It is clearly demonstrated by comparison with past wall resolved LES efforts that the wall model reduces the computational complexity by at least an order of magnitude without any significant loss in accuracy. The wall model is then extended to the simulation of rough surfaces. Comparison with available experiments at high Reynolds numbers shows that the roughness modified wall model successfully predicts the effect of roughness on the mean as well as turbulent flow-field.
- Summary of the thesis with concluding remarks is presented in Chapter 7.

The thesis makes the following engineering and scientific contributions to the literature.

- The zonal two-layer wall model is formulated in the generalized coordinates LES framework with novel treatment for the effective tangential velocity. This formulation reduces the calculation time in the inner layer significantly and is most suitable for complex geometries involving body fitted and unstructured meshes. This formulation is extended further to account for near wall heat transfer and surface roughness.
- The integrated zonal treatment for velocity and temperature is used to investigate successfully the complex three dimensional flow in an internal ribbed cooling turbine duct geometry for the first time.

- Flow in the rod roughened channel is investigated at high Reynolds numbers. This is a first of kind study where a two-layer roughness model is formulated in the LES framework and showed to successfully account for effects of roughness on mean flow and turbulent statistics.
- The efficacy of inlet turbulence generation and the wall model to reduce the computational resources and overall calculation time is demonstrated in a backward facing step flow at a high Reynolds number, $Re=40,000$, which is the highest Reynolds number LES in a backward facing step geometry.
- The use of the synthetic eddy method to accurately represent the inlet turbulence in complex turbulent swirling flows at different swirl strengths is demonstrated in an experimental swirl combustor and industrial scale can combustor. The synthetic eddy method with a zonal wall model is used for the first time to investigate the swirling flow-field in a combustor. It is shown that the accurate generation of inflow turbulent conditions is important to the flow predictions inside the combustor.
- Liner wall heat transfer is characterized in an industrial Dry Low Emission combustor. This is the first of a kind RANS study where the effect of realistic engine condition Reynolds numbers on the liner wall heat transfer is studied. Two different configurations, can and annular combustors with engine scale swirlers generating different swirl strengths were investigated. A comparative study between these two configurations is performed with a proposed definition of a modified Swirl number.

This study will provide guidelines to combustor designers for developing more efficient cooling schemes for industrial gas turbine combustors.

- A first of a kind hybrid RANS-LES simulation is performed in an industrial gas turbine can combustor. Inflow time-dependent boundary conditions are generated using results from upstream RANS data for LES calculations embedded in the region of interest. The zonal near wall treatment, used to characterize the liner wall heat transfer and its interaction with the swirling flow is found to accurately calculate heat transfer coefficient distribution on the liner wall. This study will encourage the use of such hybrid RANS-LES techniques in industries to study the complex time dependent turbulent features in regions of interest.

Following is the list of peer reviewed conference papers and journal papers written as an integral part of this dissertation.

Conference papers

- Patil S., Abraham S., Tafti D., and Ekkad S., 2009. "Experimental and numerical investigation of convective heat transfer in gas turbine can combustor," paper No. GT2009-59377, ASME IGTI Turbo Expo 2009, Orlando, FL.
- Patil S., Sedalor T., Tafti D., and Ekkad S., 2010. "Study of flow and heat transfer in Dry Low Emission gas turbine combustor," paper No. GT2010-22986, ASME IGTI Turbo Expo 2010, Glasgow, UK.

- Patil S., and Tafti D., 2011. "Wall modeled large-eddy simulation of backward facing step with synthetic inlet turbulence at high Reynolds number," Paper No. 896435, AIAA Aerospace and Science Meet, Orlando, FL.
- Patil S., and Tafti D., 2011. "Large-eddy simulation with zonal near wall treatment of flow and heat transfer in a ribbed duct for internal cooling of turbine blades," paper No. GT2011-45749, ASME IGTI Turbo Expo 2011, Vancouver, Canada.
- Patil S., and Tafti D., 2011. "Large-eddy simulation of flow and convective heat transfer in a gas turbine can combustor with synthetic inlet turbulence," paper No. GT2011-46561, ASME IGTI Turbo Expo 2011, Vancouver, Canada.

Journal papers

- Patil S., Abraham S., Tafti D., Ekkad S., Kim Y., Dutta P., Moon H., Srinivasan R., 2011. "Experimental and numerical investigation of convective heat transfer in gas turbine can combustor," Journal of Turbomachinery, 133(1).
- Patil S., Sedalor T., Tafti D., and Ekkad S., 2011. "Study of flow and heat transfer in a Dry Low Emission annular gas turbine combustor," Journal of Turbomachinery, Under Review.
- Patil S., and Tafti D., 2011. "Wall modeled large-eddy simulation of complex high Reynolds number flows with synthetic inlet turbulence," International Journal of Heat and Fluid Flow, to be submitted.

- Patil S., and Tafti D., 2011. "Large-eddy simulation of flow in a rod roughened channel using a two-layer roughness wall model," Short note, AIAA Journal (to be submitted)

Chapter 2

RANS Investigation of Convective Heat Transfer in Dry Low Emission (DLE)

Gas Turbine Combustors

The objective of this chapter is to characterize combustor liner wall heat transfer and investigate the effect of Reynolds number and Swirl number on liner wall convective heat transfer coefficient in a can and annular type gas turbine combustor configuration at realistic engine conditions. An engine scale swirler is used to simulate the actual flow conditions downstream of the swirler. The Reynolds numbers vary between 50,000 to 840,000 and the Swirl number between 0.7 to 0.98. The numerical calculations investigated RANS (Reynolds Averaged Navier-Stokes) based turbulence models to predict the swirling flow and surface heat transfer coefficients. For comparison, different turbulence models, such as, standard, realizable and RNG (Re-Normalization Group theory) k - ϵ , SST (Shear Stress Transport) are tested. It is shown that for a given Swirl number, the location of peak heat transfer augmentation is quite independent of the Reynolds number, whereas the augmentation ratio decays considerably as the Reynolds number increases. Different swirl strengths in different configurations play a major role in the value of the heat transfer augmentation and its decay with an increase in Reynolds number. The study is unique in that these trends on combustor liner gas side wall heat transfer have never been captured and explained in the literature and have important implications on the design of liner wall cooling systems.

2.1 Computational Methodology

A full three dimensional incompressible steady state analysis was carried out using the commercial software ANSYS-FLUENT [27] to characterize heat transfer on the liner wall as well as to visualize and understand the effect of strong swirl. Figure 2.1 shows the computational domain for can combustor configuration, consisting of a periodic segment of the injector and the can combustor. The flow in a single passage of the injector swirler vanes is simulated. It consists of an annular inlet section, followed by the swirler vanes, the fuel injector followed by a straight section of the injector which opens into the can combustor. The computational domain was mapped using a multi-block structured mesh with total 3.4 million hexahedral cells. Figure 2.2 shows the computation domain for the annular combustor configuration, consisting of a swirler nozzle and a periodic segment of the annular combustor. The flow in a single swirler nozzle with 12 swirler vanes which expands in the annular combustor is simulated. The computational domain for the annular combustor was mapped using a multi-block structured mesh with total 20.5 million hexahedral cells using commercial grid generation software GRIDGEN. Figure 2.3.a displays the grid on the swirler vane wall while Figure 2.3.b shows the mesh in the vane passages. The swirl nozzle consists of about 3 million mesh elements. Figure 2.3.c gives the overall frontal mesh view from upstream of the flow inlet. Near wall orthogonality is maintained as much as possible in both the configurations to improve solution accuracy and convergence characteristics.

For the RANS calculations, two approaches were used to resolve the boundary layer. For lower Reynolds numbers ($Re = 50,000$ and $Re = 80,000$), wall integration was used as the near

wall treatment with y^+ values in the range of 1 to 5. The wall function approach was more economical at high Reynolds numbers with y^+ ranging from 30 to 100. The SIMPLE algorithm is used for pressure velocity coupling with the second order upwind convection discretization scheme for all variables. Table 2.1 summarizes the numerical calculations and Table 2.2 summarizes the boundary conditions used in the numerical investigation. The inlet section of the computational domain was given a boundary condition of mass flow inlet based on Reynolds number. The Reynolds number was increased using higher inlet velocity (for 50,000 and 80,000 case) and higher density (for $Re=200,000$ and above). Periodic boundary conditions were specified in the azimuthal direction, and an outflow condition was used at the combustor exit. The rest of the domain surfaces including vanes were assigned wall (no slip) boundary conditions. A surface heat flux value was specified for the combustor liner wall while all other walls were treated as adiabatic. All the computations were run on the IBM IDataPlex nodes. Each node is dual-socket quad-core with Intel Nehalem processors running at 2.26 GHz with 48 GB of RAM each.

2.2 Results

2.2.1 Validation of Computational Model

A number of different turbulence models were tested for their ability to predict the strongly swirling flow in the combustor. Figure 2.4 compares results of various turbulence models used in the calculations with experimental data for a Reynolds number of 50,000 for the can combustor configuration. The heat transfer coefficient at the liner wall is characterized by

the Nusselt number augmentation ratio, where the baseline Nusselt number is obtained from the Dittus-Boelter correlation for fully-developed turbulent pipe flow with heated walls.

$$Nu_0 = 0.023 \times Re^{0.8} \times Pr^{0.4} \quad (2.1)$$

The circumferentially averaged Nusselt augmentation predictions are plotted versus axial distance normalized by the hydraulic diameter of the combustor. It was found that the RNG model with swirl modification and differential viscosity model [27] predicted the results in best agreement with experiments. The model predicted both the location and magnitude of peak heat transfer in exact agreement with experiments. However, some difference between the model prediction and experiments exist downstream of the peak location. It was found that the SST model over predicted the values of peak heat transfer coefficients while the standard and realizable k- ϵ models under predicted it. Also the peak location is predicted downstream of the experimental measurements. It is clear from this comparison that the RNG model predicts the highly strained swirl flow coming out of the injector with much better fidelity than the other models. Hence, the RNG model is used for investigating the effect of Reynolds number on heat transfer.

Figure 2.5 further compares predictions with experiments at Re=50,000 and 80,000 using the RNG k- ϵ model. It is observed that the predictions compare very well with experiments at Re=80000. More importantly, it is also observed that the location of peak heat transfer remains the same but the magnitude of peak augmentation reduces from approximately 10 to 8. This is explained by investigating the flow-field in the combustor in more detail.

Figure 2.6 compare predictions with the experimental measurements for all three Reynolds number investigated in the range 210,000 and 840,000 for the annular combustor configuration. It is observed that predictions compare reasonably well with experiments. For all three Reynolds numbers, the computational model is able to predict peak heat transfer magnitude and location in close agreement with the experiments. The computational model predicted the magnitude of heat transfer augmentation at the peak location in very close agreement with experiments for Reynolds numbers of 210,000 and 420,000 and in fairly good agreement for higher Reynolds number of 840,000. However, some difference between the model prediction and experiments exist downstream of the peak location. The same trends between prediction and experiments were also observed in can combustor configuration. Overprediction of heat transfer augmentation in the region far downstream of the peak heat transfer location represents that the decay rate of swirl and turbulence is underpredicted in this region by the computational model. The computational model was also able to capture the differences in the magnitude of peak heat transfer augmentation on the convex and concave combustor liner walls. It is important to note that the experimental measurements observed much larger drop in augmentation on concave liner walls for Reynolds number of 840,000. Numerical calculations slightly overpredicted the Nusselt augmentation on the concave liner wall. This might be due to a comparatively coarser near wall mesh resulting in higher values of wall y^+ , though the calculation on this grid did not result in any significant change in convergence characteristics of any conservative variable compared with calculations for the other Reynolds numbers.

2.2.2 Flow-field Characteristics

Figure 2.7 characterizes the flow-field for a Reynolds number of 50,000 in a can combustor configuration. The streamline plot in Figure 2.7 expresses two main features of swirl flow in the combustor geometry, a corner recirculation zone, and a central recirculation zone. The presence of the central recirculation zone indicates that the Swirl number is beyond the critical value of 0.6. The Swirl number is defined as the ratio of axial flux of tangential momentum to axial flux of axial momentum and is calculated as

$$S = \frac{\int r V_{\theta} V_x dr}{R_0 \int V_x^2 dr} \quad (2.1)$$

Its value at an axial plane near the injector exit was found to be 0.7. The computational flow structure is in complete agreement with past studies [20].

Figure 2.7 also shows that the location of the peak heat transfer coincides with the impingement of the highly energetic shear layer issuing from the injector. The flow impingement can be visualized with contours of normalized axial velocity and turbulent kinetic energy. A large augmentation in heat transfer coefficient is observed because of the very high values of axial velocity and turbulent kinetic energy near the impingement location. Furthermore, the spread angle of flow expanding into the can combustor is much higher than that without swirl, which results in flow impingement very close to the inlet of the combustor ($X/D=0.38$) with higher axial velocity. This is the main mechanism responsible for the location and peak magnitude of heat transfer augmentation.

Figure 2.8 visualizes the 3D swirl dominated flow-field by replicating the computation domain in the azimuthal direction to cover the full combustor. The isocontours (value = 1000) of

vorticity colored with axial velocity are shown. Structures of corner recirculation zone, central recirculation zone and precessing vortex core show good qualitative agreement to the experimental visualization provided by Rhode et al. [20] for a similar geometry.

Similar flow structures were observed for the annular combustor configuration and are represented in Figure 2.9. The Swirl number was found to be 0.98, which is significantly higher than the can configuration. This higher swirl strength results in higher shear layer spread angle and hence a shorter corner recirculation zone. This is further explained in later subsections.

2.2.3 Effect of Reynolds number

Figure 2.10 shows the effect of Reynolds numbers ranging from 50,000 – 500,000 on the location and magnitude of the computed heat transfer coefficient along the can combustor liner wall. It is clear that the peak value of heat transfer augmentation reduces with an increase in Reynolds number but the location of the peak value does not change with increasing Reynolds number.

Figure 2.11 shows the variation of peak Nusselt number augmentation with Reynolds number. The numerical values match in very close agreement with experimental results at 50,000, 80,000 and 500,000. Experimental data for 500,000 was reported by Goh [28] on exactly the same geometry. The large drop in augmentation ratio but the invariability of the location of peak heat transfer with Reynolds number is explained in the following manner.

Figure 2.12 shows the variation of turbulent kinetic energy (TKE) normalized with the square of mean velocity in the can combustor at a location near the peak heat transfer. Since in most shear flows, wall heat transfer is largely dependent on the magnitude of near wall turbulent

quantities, the TKE magnitude close to the wall is a good indicator of turbulent activity. The plot shows that the normalized TKE reduces with increase in the Reynolds number, hence explaining why the heat transfer coefficient augmentation ratio decreases with an increase in Reynolds number (it is noted that the heat transfer coefficient increases with Reynolds number). The TKE production in the impinging shear layer is dependent on the Reynolds number as well as the degree of swirl. However, it is noted that even with the increase in Reynolds number the Swirl number remains constant at 0.7 since it is largely dependent on the injector vane geometry. Hence, although turbulent production increases in the impinging shear layer as a result of increased Reynolds number, the normalized value decreases because it is strongly dependent on the Swirl number which remains the same.

The relative invariability of the peak location with Reynolds number can also be explained by the constant Swirl number. The primary reason for this is that the flow pattern established in the combustor is independent of the Reynolds number. Figure 2.13 shows the streamline structure in the combustor for Reynolds numbers of 80,000 and 500,000. It is seen that the overall flow structure changes very little and hence the location of impingement remains fairly constant over the range of Reynolds numbers.

Similar observations are made for annular combustor configuration. Though, for annular combustor configuration, the drop in Nusselt augmentation with increase in Reynolds number is slow. The CFD simulations capture the trend in heat transfer coefficients reasonably well, especially near the peak location. There are some differences between the convex and concave surfaces with the concave surface showing higher heat transfer coefficients than the convex

surface for Reynolds numbers 210,000 and 420,000. This is attributed to the higher levels of turbulent kinetic energy in the impinging shear layer near the concave combustor liner wall as compared to the convex liner wall (see Figure 2.14). Similar to the can combustor, it is also observed that the flow structures in the combustor are mostly independent of the Reynolds number and are mainly a function of Swirl number which remains constant at a value of 0.98 for the Reynolds number range investigated.

2.2.4 Effect of Swirl Strength

The characteristic Swirl number was found to be 0.7 and 0.98 for can and annular combustor configurations, which remained constant for the investigated Reynolds number range for the respective configurations. This difference in swirl strength results in different values of Nusselt augmentation and normalized flow impingement length. To make a comparison between these two configurations of can and annular combustor, a modified Swirl number is proposed as in Equation (2.2).

$$S_m = \frac{\frac{\int r V_\theta V_x dr}{R_0 \int V_x^2 dr}}{\frac{h}{R_0}} \quad (2.2)$$

where, h is the step expansion height as shown in Figure 2.15. This modified Swirl number not only takes into account the swirl strength produced by the swirler but also includes the geometrical features of the combustor in the form of the non-dimensional expansion step height, which is an important parameter influencing the location and the strength of the shear layer impinging on the liner wall. The proposed modified Swirl number enables the comparison of the peak heat transfer augmentation magnitude and location in both can and annular combustor

geometries. The values of this modified Swirl number were found to be 0.47 and 0.67 for the can and annular combustor geometry, respectively. Values of normalized distance (x/D_h) of shear layer impingement and maximum heat transfer augmentation are 0.38 and 0.15 for the can and annular combustor configurations, respectively. This length is 60 percent shorter for the annular combustor compared to the can combustor. (This is in spite of the fact that the hydraulic diameter of the annular combustor is only 35 percent larger than that of the can combustor.) The higher values of the modified Swirl number in the current study results in a higher spread angle which further results in a shorter impingement length. The spread angle for annular combustor shear layer is about 6° higher than that of the can combustor.

Figure 2.16 compares the peak value of heat transfer coefficient enhancement with Reynolds number for both the concave and convex surfaces of annular combustor with that of the can combustor. It is observed that for the Reynolds number of 200,000 and higher, both the convex and concave surface in the annular combustor configuration show a slower decay than that observed for the can combustor liner wall. Also it is important to note that for the same Reynolds number, for example 420,000, the value of peak heat transfer augmentation is much higher for both convex and concave surfaces in the annular combustor than in the can combustor study. This also can be attributed to the higher modified Swirl number in the annular combustor configuration. The modified Swirl number seems to be playing a more dominant role than Reynolds number in the annular combustor configuration. The higher modified Swirl number not only results in higher heat transfer augmentation but also results in a smaller decrease at high Reynolds number in annular combustor compared to the can combustor configuration.

2.3 Conclusions

Numerical calculations are performed to investigate the convective heat transfer characteristics of dry low emission gas turbine combustor liners under cold flow conditions. RANS based turbulence models were tested to predict the swirling flow and surface heat transfer coefficients in an engine scale can and annular combustor. The RNG turbulence model was best suited for the swirl dominated flow. Results for peak heat transfer augmentation factor and location were in close agreement with experimental predictions.

It is observed that the flow-field in the combustor is characterized by an expanding swirling flow which impinges on the liner wall close to the inlet of the combustor. The impinging shear layer is responsible for the peak location of heat transfer augmentation. It is observed that as Reynolds number increases, the peak heat transfer augmentation ratio reduces, while the peak location remains the same. This is attributed to the reduction in normalized turbulent kinetic energy in the impinging shear layer which is strongly dependent on the Swirl number that remains constant with change in Reynolds number. Additionally, since the flow structure in the combustor is also a function of the Swirl number, the peak location does not change with Reynolds number. The size of the corner recirculation zone near the combustor liner remains the same for all Reynolds numbers and hence the location of shear layer impingement and peak augmentation does not change. The interaction of the swirl flow with the different surface curvatures in the annular combustor results in a slightly different heat transfer characteristics on the concave and convex liner walls.

A modified Swirl number based on the step height is proposed for comparing the location and decay of peak heat transfer between the can and annular combustor configurations. It is observed that a larger modified Swirl number results in higher jet spread angle and a shorter impingement length. The higher modified Swirl number results in much higher heat transfer augmentation for the same Reynolds number and results in a slower decay of heat transfer augmentation with increase in Reynolds number.

2.4 Tables

Table 2.1 Numerical calculation summary

| Reynolds number | Combustor configuration | Turbulence model | Near wall treatment | Mesh adaptivity |
|-----------------|-------------------------|---|---------------------|------------------------|
| 50,000 | Can | Standard k- ϵ Realizable k- ϵ RNG k- ϵ SST k- ω RSM | Wall integration | Not applied |
| 80,000 | Can | RNG k- ϵ | Wall integration | Applied based on y^+ |
| 300,000 | Can | RNG k- ϵ | Wall function | Not applied |
| 350,000 | Can | RNG k- ϵ | Wall function | Not applied |
| 400,000 | Can | RNG k- ϵ | Wall function | Applied based on y^+ |
| 500,000 | Can | RNG k- ϵ | Wall function | Applied based on y^+ |
| 210,000 | Annular | RNG k- ϵ | Wall function | Applied based on y^+ |
| 420,000 | Annular | RNG k- ϵ | Wall function | Applied based on y^+ |
| 840,000 | Annular | RNG k- ϵ | Wall function | Applied based on y^+ |

Table 2.2 Boundary conditions

| Computational face | Flow BC | Thermal BC |
|---|---------------------------------|----------------------------------|
| Inlet | Mass inflow / Velocity Inlet | (Ref. Temp = 294K) |
| Outlet | Outflow | - |
| External Periodic | Periodic | Periodic |
| Liner wall | No slip | Surface heat flux specified |
| Hub, casing, vanes and injector pins | No slip | Adiabatic (surface heat flux= 0) |

2.5 Figures

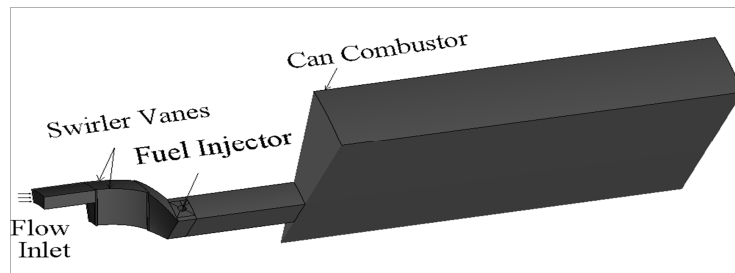


Figure 2.1 Computational domain consisting periodic segment (sector angle = 18°) of swirl nozzle and can combustor

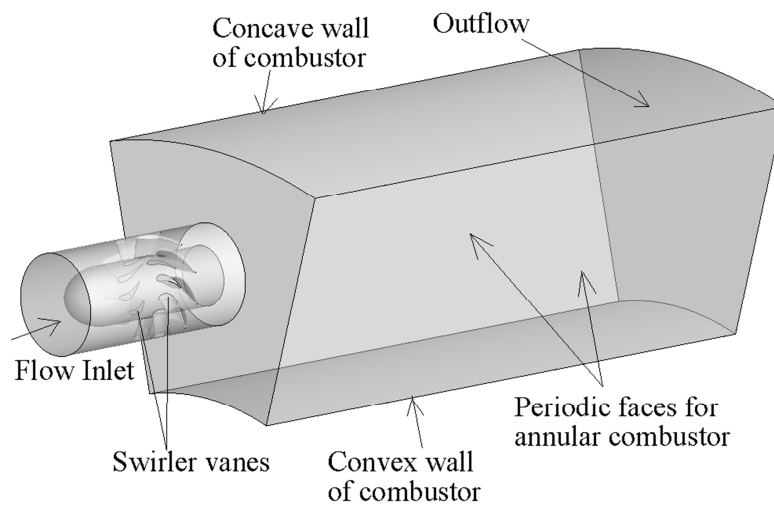
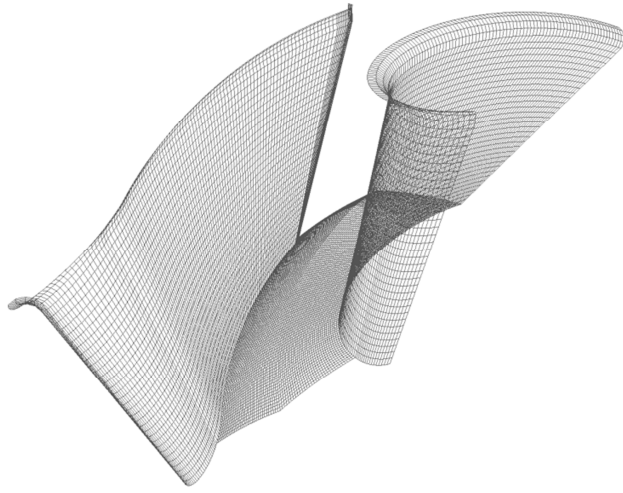
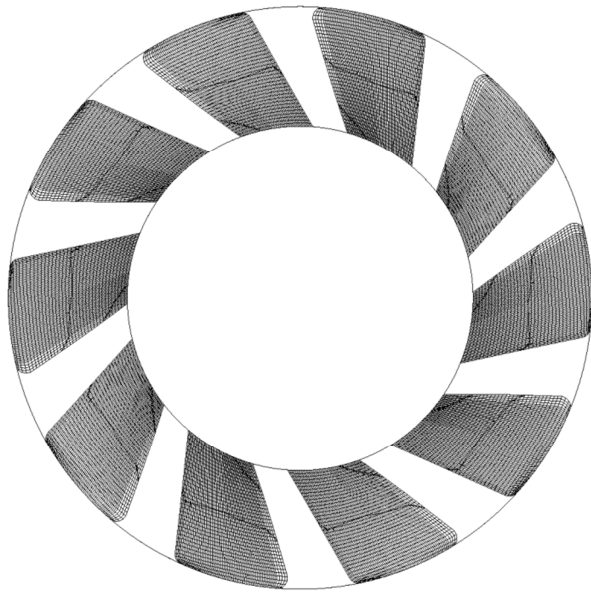


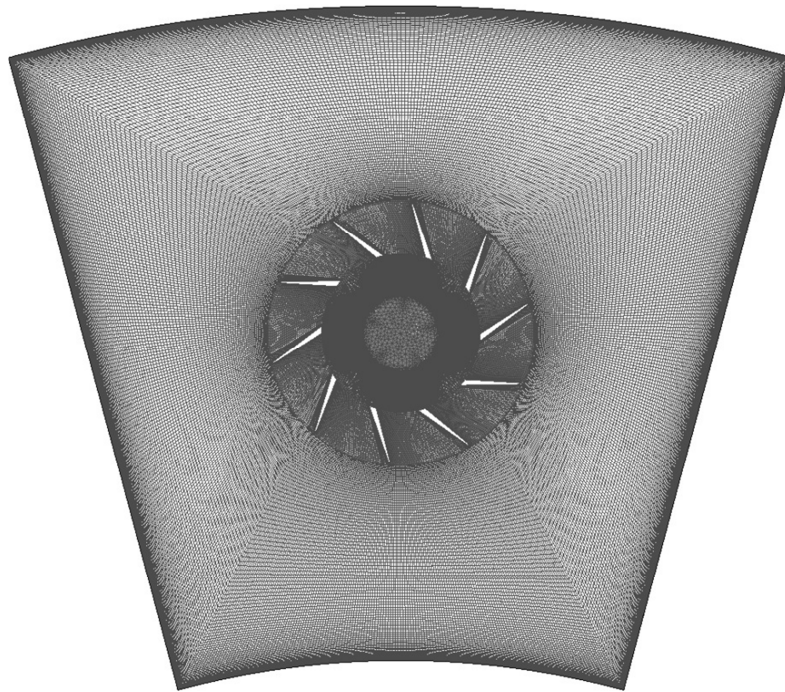
Figure 2.2 Computational domain consisting of swirl nozzle and periodic segment (sector angle = 30°) of annular combustor



(a)



(b)



(c)

Figure 2.3 Computational grid details for annular combustor configuration. (a) mesh on the swirler vanes (b) mesh in the passage between the two vanes (c) head on view of overall mesh in the swirler and annular combustor

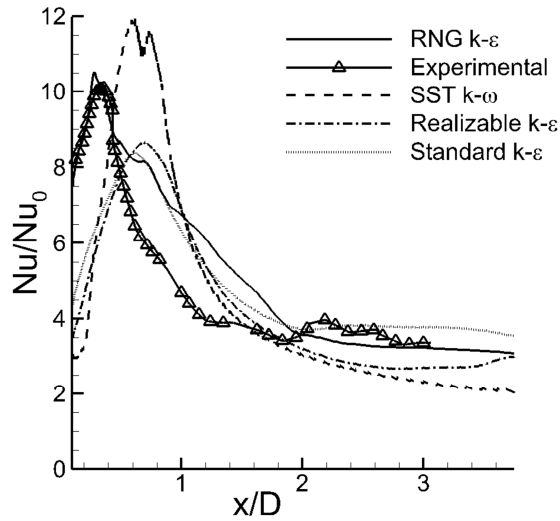


Figure 2.4 Comparison of numerical predictions for can combustor liner wall heat transfer augmentation with experiments using different turbulence models at Re=50,000

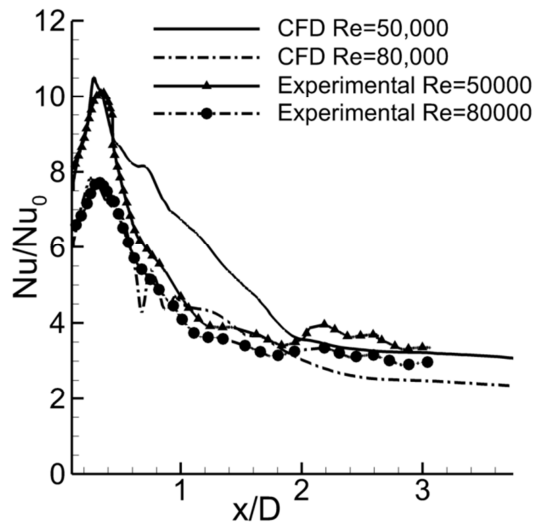
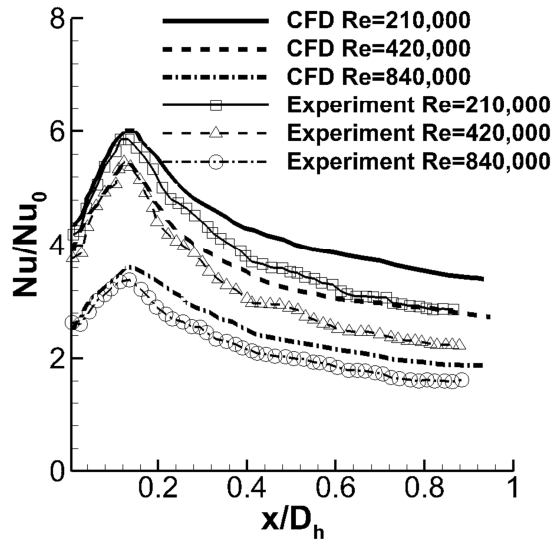
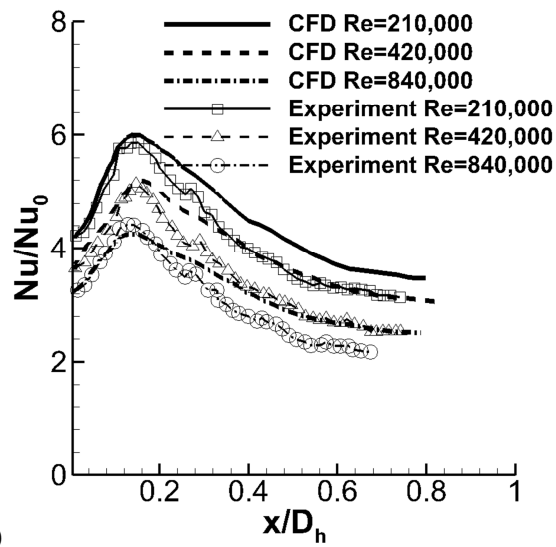


Figure 2.5 Nusselt number augmentation for Re=50,000 and Re= 80,000 along the can combustor liner wall

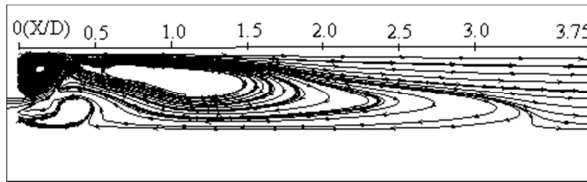


(a)

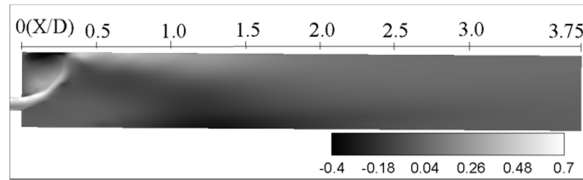


(b)

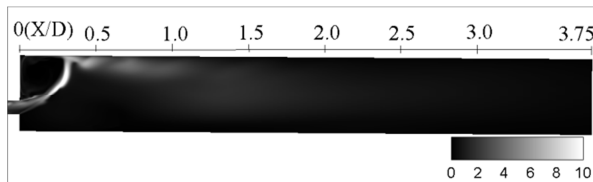
Figure 2.6 Nusselt number augmentation on (a) concave liner wall, and (b) convex liner wall of the annular combustor



(a)



(b)



(c)

Figure 2.7 (a) Flow streamlines (b) contours of normalized axial velocity, and (c) contours of normalized turbulent kinetic energy in a meridional plane in the can combustor

(Re = 50,000)

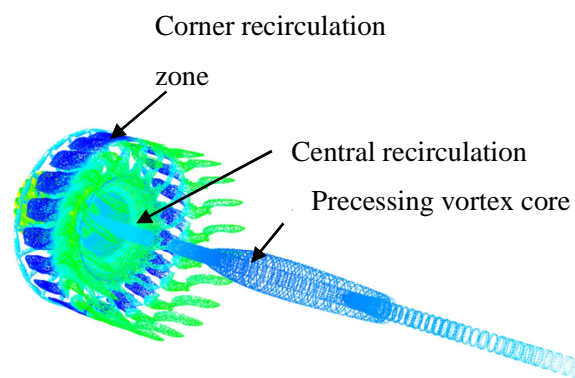


Figure 2.8 Axial vorticity iso-contour (value = 1000) in can combustor colored with axial velocity
(Re=50,000)

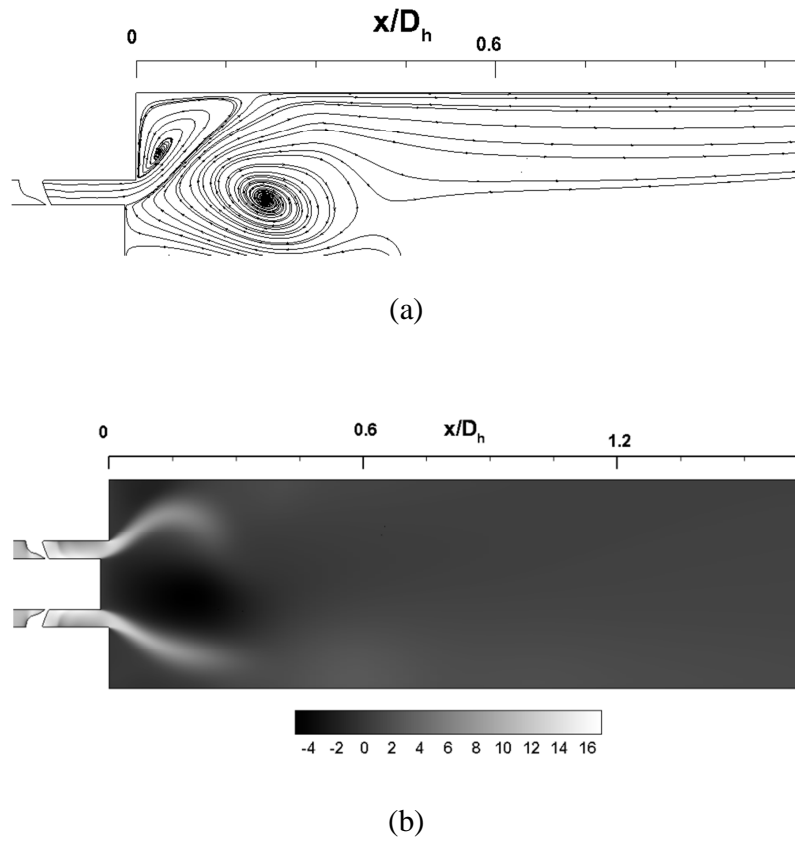


Figure 2.9 (a) Flow streamlines, and (b) contours of normalized axial velocity in a meridional plane in the annular combustor

($Re = 420,000$)

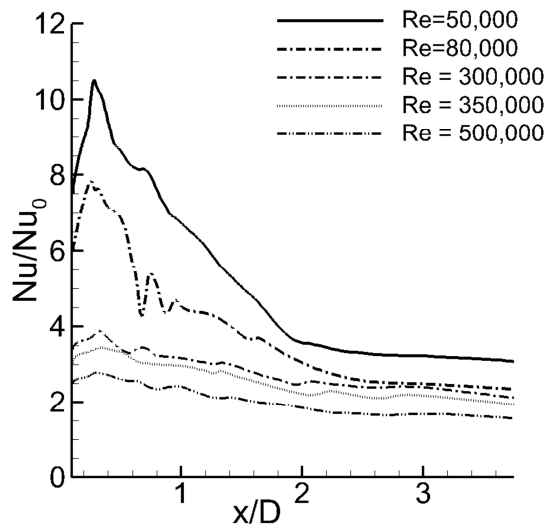


Figure 2.10 Effect of Reynolds number on can combustor liner wall heat transfer augmentation

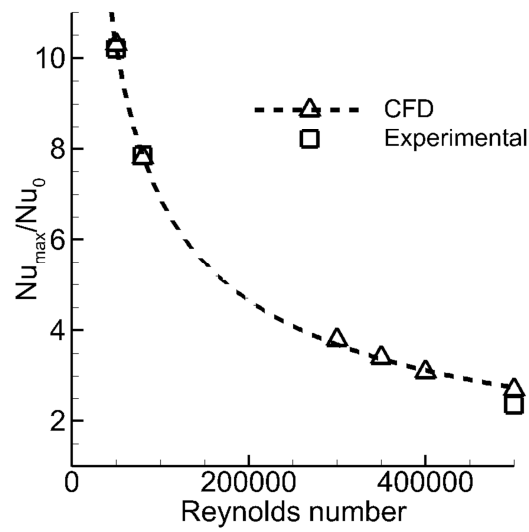


Figure 2.11 Variation of peak heat transfer augmentation ratio on can combustor liner wall with Reynolds number

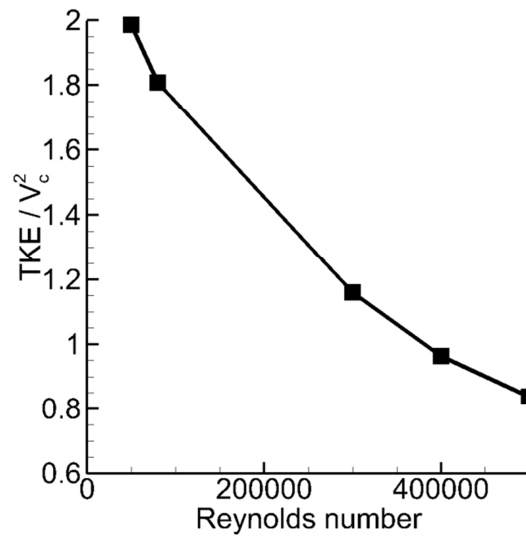
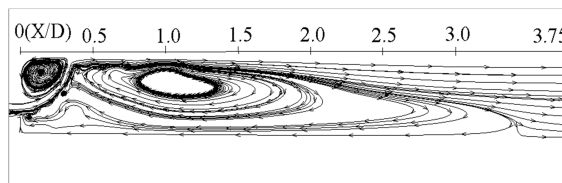
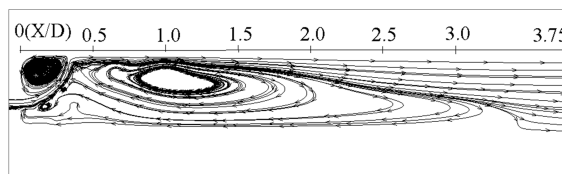


Figure 2.12 Variation of normalized turbulent kinetic energy with Reynolds number near shear layer impingement location on can combustor liner wall



(a)



(b)

Figure 2.13 Flow streamlines in can combustor for (a) $Re = 80,000$ and (b) $Re = 500,000$

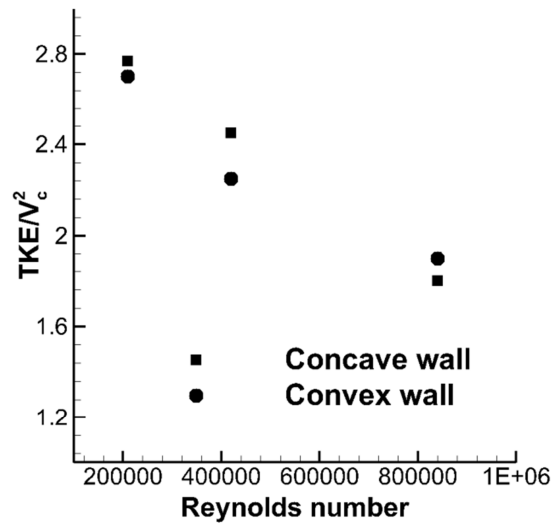


Figure 2.14 Variation in normalized turbulent kinetic energy with increase in Reynolds number near shear layer impingement location on the annular combustor liner wall

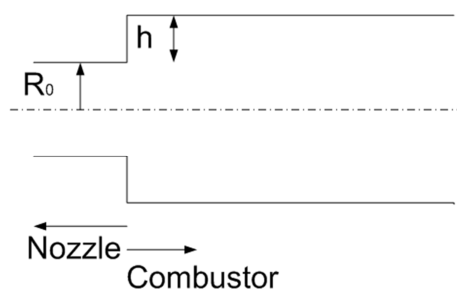


Figure 2.15 Generic representation of swirler-combustor configuration

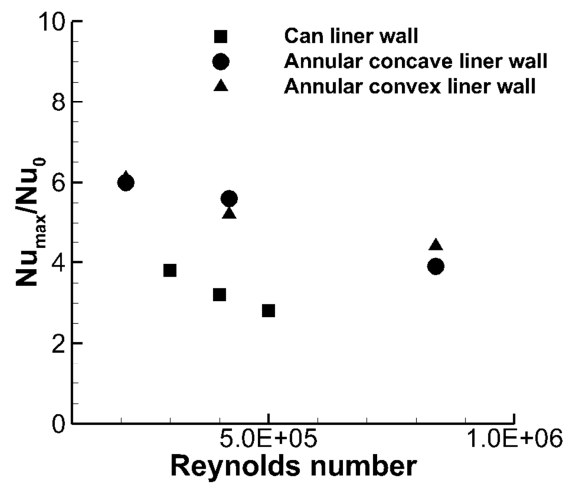


Figure 2.16 Variation of peak heat transfer augmentation with Reynolds number for can and annular combustor

Chapter 3

Governing Equations and Numerical Implementation

The main goal of this chapter is to present the development of the LES wall modeling technique and the implementation of the synthetic eddy method for the generation of inlet turbulence. Peripheral to these goals are the governing equations and the numerical methods employed for the LES of complex flows. The chapter first describes the non-dimensional incompressible mass, momentum, and energy conservation equations in a generalized coordinate system with a brief description of the numerical method employed and the algorithmic considerations. This is followed by the motivation behind different wall modeling techniques used with LES. A notable contribution of this chapter is the generalization of the two layer wall model to complex geometries for both the momentum and energy equations. Different techniques used in the literature for the generation of turbulent inlet boundary conditions are then outlined and the implementation of the synthetic eddy method is described. This chapter forms the theoretical foundation of the LES simulations performed in the following chapters.

3.1 Governing Equations and Numerical Method

The governing equations for unsteady incompressible viscous flow consists of mass, momentum, and energy conservation laws. The equations are mapped from physical (\vec{x}) to logical/computational space ($\vec{\xi}$) by a boundary conforming transformation $\vec{x} = \vec{x}(\vec{\xi})$, where $\vec{x} = (x, y, z)$ and $\vec{\xi} = (\xi, \eta, \zeta)$. The equations are non-dimensionalized by a suitable length scale (L^*) and velocity scale (U^*) and written in conservative non-dimensional form as:

Mass:

$$\frac{\partial}{\partial \xi_j} (\sqrt{g} U^j) = 0 \quad (3.1)$$

Momentum:

$$\frac{\partial}{\partial T} (\sqrt{g} u_i) + \frac{\partial}{\partial \xi_j} ((\sqrt{g} U^j) u_i) = -\frac{\partial}{\partial \xi_j} (\sqrt{g} (\vec{a}^j)_i p) + \frac{\partial}{\partial \xi_j} \left(\left(\frac{1}{\text{Re}} + \frac{1}{\text{Re}_t} \right) \sqrt{g} g^{jk} \frac{\partial u_i}{\partial \xi_k} \right) \quad (3.2)$$

Energy

$$\frac{\partial}{\partial T} (\sqrt{g} \theta) + \frac{\partial}{\partial \xi_j} ((\sqrt{g} U^j) \theta) = \frac{\partial}{\partial \xi_j} \left(\left(\frac{1}{\text{Re Pr}} + \frac{1}{\text{Re}_t \text{Pr}_t} \right) \sqrt{g} g^{jk} \frac{\partial \theta}{\partial \xi_k} \right) \quad (3.3)$$

where \vec{a}^i are the contravariant basis vectors, \sqrt{g} is the Jacobian of the transformation, g^{ij} are the elements of the contravariant metric tensor, $\sqrt{g} U^j = \sqrt{g} (\vec{a}^j)_k u_k$ is the contravariant flux vector, u_i is the Cartesian velocity vector, p is the pressure, and θ is the non-dimensional temperature. The non-dimensional time used is $T^* U^* / L^*$ and the Reynolds number is given by $U^* L^* / \nu$, Re_t is the inverse of the subgrid eddy-viscosity which is modeled as

$$\frac{1}{\text{Re}_t} = C_s^2 (\sqrt{g})^{2/3} |\bar{S}| \quad (3.4)$$

where $|\bar{S}|$ is the magnitude of the strain rate tensor given by $|\bar{S}| = \sqrt{2 \overline{S_{ik} S_{ik}}}$ and the Smagorinsky constant C_s^2 is obtained via the dynamic subgrid stress model [29]. To this end, a second test

filter, denoted by \widehat{G} , is applied to the filtered governing equations with the characteristic length scale of \widehat{G} being larger than that of the grid filter, \overline{G} . The test filtered quantity is obtained from the grid filtered quantity by a second-order trapezoidal filter which is given by $\widehat{\phi} = \frac{1}{4}(\overline{\phi}_{i-1} + 2\overline{\phi}_i + \overline{\phi}_{i+1})$ in one dimension. The resolved turbulent stresses, representing the energy scales between the test and grid filters, $L_{ij} = \widehat{u_i u_j} - \widehat{u_i} \widehat{u_j}$, are then related to the subtest, $T_{ij} = \widehat{u_i u_j} - \widehat{u_i} \widehat{u_j}$, and subgrid-scales stresses, $\tau_{ij} = \overline{u_i u_j} - \overline{u_i} \overline{u_j}$, through the identity, $L_{ij}^a = T_{ij}^a - \widehat{\tau}_{ij}^a$. The anisotropic subgrid and subtest-scale stresses are then formulated in terms of the Smagorinsky eddy viscosity model as:

$$\widehat{\tau}_{ij}^a = -2C_s^2 (\sqrt{g})^{2/3} \widehat{S}_{ij} \quad (3.5)$$

$$T_{ij}^a = -2C_s^2 \alpha (\sqrt{g})^{2/3} \widehat{S}_{ij} \quad (3.6)$$

Using the identity,

$$\widehat{L}_{ij}^a = \widehat{L}_{ij} - \frac{1}{3} \delta_{ij} L_{kk} = 2C_s^2 (\sqrt{g})^{2/3} \left[\alpha \widehat{S}_{ij} - \widehat{S}_{ij} \right] = -2C_s^2 (\sqrt{g})^{2/3} M_{ij} \quad (3.7)$$

Here α is the square of the ratio of the characteristic length scale associated with the test filter to that of grid filter and is taken to be $[\widehat{\Delta}_i / \overline{\Delta}_i = \sqrt{6}]$ for a representative one-dimensional test filtering operation [31]. Using a least-squares minimization procedure of Lilly [30], a final expression for C_s^2 is obtained as:

$$C_s^2 = -\frac{1}{2} \frac{1}{(\sqrt{g})^{2/3}} \frac{L_{ij}^a \cdot M_{ij}}{M_{ij} \cdot M_{ij}} \quad (3.8)$$

The value of C_s^2 is constrained to be positive

3.2 Numerical Implementation and Algorithm

The governing equations for mass, momentum, and energy are discretized with a conservative finite-volume formulation using a second-order central (SOC) difference scheme on a non-staggered grid topology. The SOC discretization has minimal dissipation and has been shown to be suitable for LES computations. The Cartesian velocities and pressure are calculated and stored at the cell center, whereas contravariant fluxes are stored and calculated at cell faces. For the time integration of the discretized continuity and momentum equations, a projection method is used. The temporal advancement is performed in two steps, a predictor step, which calculates an intermediate velocity field, and a corrector step, which calculates the updated velocity at the new time step by satisfying discrete continuity.

Predictor Step

$$\frac{\sqrt{g}^{n+1} \tilde{u}_i - \sqrt{g}^n u_i^n}{\Delta t} = D_i - C_i \quad (3.9)$$

where D_i is the flow diffusion term and C_i is flow convection term. Convection and diffusion terms are treated implicitly by a Crank-Nicolson scheme.

Convection Terms

$$C_i = \frac{\partial}{\partial \xi_j} (\sqrt{g} U^j u_i)^{n+1/2} \quad (3.10)$$

$$C_i = \frac{1}{2} \left[\frac{\partial}{\partial \xi_j} (\sqrt{g} U^j u_i)^n + \frac{\partial}{\partial \xi_j} (\sqrt{g} U^j u_i^{n+1}) \right] \quad (3.11)$$

The contravariant fluxes at time level $n+1$ are linearized using a two-step (n and $n-1$ time level) second order extrapolation as:

$$\sqrt{g} U^{j^{n+1}} = 2\sqrt{g} U^{j^n} - \sqrt{g} U^{j^{n-1}} \quad (3.12)$$

Diffusion Terms

$$D_i = \frac{1}{2} \left[\frac{\partial}{\partial \xi_j} \left(\left(\frac{1}{\text{Re}} + \frac{1}{\text{Re}_t} \right) \sqrt{g} g^{jk} \frac{\partial u_i^n}{\partial \xi_k} \right) + \frac{\partial}{\partial \xi_j} \left(\left(\frac{1}{\text{Re}} + \frac{1}{\text{Re}_t} \right) \sqrt{g} g^{jk} \frac{\partial \tilde{u}_i}{\partial \xi_k} \right) \right] \quad (3.13)$$

Corrector Step

In this step, the continuity equation is used to derive the pressure equation, which is solved to obtain the pressure field at time level $(n+1)$. The procedure used in formulating the pressure equation is represented as follows:

First the intermediate cell face contravariant fluxes are constructed as follows

$$\sqrt{g} \tilde{U}^j = \sqrt{g} (\bar{a}^j)_i \tilde{u}_i \quad (3.14)$$

Then, the correction form of the cell centered Cartesian velocities and cell face contravariant fluxes are written as:

$$u_i^{n+1} = \tilde{u}_i - \Delta t (\bar{a}^j)_i \frac{\partial p^{n+1}}{\partial \xi_j} \quad (3.15)$$

$$\sqrt{g}(U^i)^{n+1} = \sqrt{g}\tilde{U}^i - \Delta t \sqrt{g} g^{ik} \frac{\partial p^{n+1}}{\partial \xi_k} \quad (3.16)$$

Finally, Equation (3.16), in conjunction with Equation (3.1), is used to derive the pressure equation, which takes the form:

$$\frac{\partial}{\partial \xi_j} \left(\sqrt{g} g^{jk} \frac{\partial p^{n+1}}{\partial \xi_k} \right) = \frac{1}{\Delta t} \frac{\partial \sqrt{g} \tilde{U}^j}{\partial \xi_j} \quad (3.17)$$

By using the contravariant fluxes at the cell faces in constructing the pressure equation, the method emulates a staggered grid arrangement. The pressure field at level $n+1$ is then used to correct the nodal Cartesian velocities and the cell face contravariant fluxes using Equation (3.15) and Equation (3.16), respectively.

3.3 Parallel Implementation

The computational code structure employs a multi-block framework which facilitates parallelization. The computational domain is divided into overlapping blocks, which are then distributed to multiple processors, the maximum number of which are limited by the total number of blocks. Each block has a separate data structure and the Message Passing Interface (MPI) is used for data transfer across processors. Further, within each block, virtual cache blocks are used while solving linear systems. A detailed description of the software architecture can be found in Tafti [32].

3.4 Wall Modeling

Large-Eddy Simulation (LES) has been shown to be a relatively accurate and reliable method in predicting anisotropic turbulent flows. Unlike the Reynolds-averaged Navier-Stokes (RANS) treatment of turbulent flows, in which all the turbulent length and time scales are modeled, LES captures all the energy containing, geometry dependent anisotropic eddies in the calculation, leaving only the small near-isotropic scales to be modeled by suitable subgrid-scale models. Hence, by definition, LES is much more receptive to the secondary strains and anisotropies in turbulent production and transport. Although LES only resolves the large-scale unsteady flow dynamics in complex flows, it still requires large computational resources at practical Reynolds number of the order of several hundred thousand to millions. Resolution requirements near the wall increase tremendously with Reynolds number [34]. In wall-proximal flows, the number of computational cells required to resolve the energy producing structures in the near-wall region scale as $Re^{1.8}$, whereas by contrast, the outer layer resolution scales as $Re^{0.4}$. The extremely fine grid in the wall proximal inner layer not only increases the number of grid points in the spatial domain but also limits the time step to very small values by stability and accuracy requirements in the temporal dimension. This adds further to the overall computational cost. Therefore, wall modeled LES is crucial to extend the usefulness of LES to higher Reynolds numbers.

Three approaches for modeling the near wall layer are the use of logarithmic law of the wall based functions, solving a separate set of equations in the near-wall region and simulating this region in Reynolds-averaged sense. Deardorff [35] and Schumann [36] introduced

approximate wall-boundary conditions to model the effect of the near wall layer. They proposed that information from the outer flow can be used to determine the local wall stress, which can then be fed back to the outer LES in the form of the momentum flux at the wall due to normal diffusion. The cost of their calculations was limited to resolving the outer-layer only and was proportional to $Re_L^{0.5}$ for spatially developing flows. Grotzbach [37], Werner and Wengle [38], Piomelli et al. [39], Hoffmann and Benocci [40], and Temmerman et al. [41] used different variants of this approach. The major drawback of this approach is that it needs a value of the mean wall shear stress *a priori* and the plane averaged velocity at the first grid point off the wall has to explicitly satisfy the logarithmic law of the wall. Hence, Schumann's [36] model and its variants work well only in simple equilibrium flows like the fully developed channel and pipe flows.

In recent years, hybrid RANS-LES approach has caught the attention of many researchers in which RANS equations are solved near the wall while the LES filtered Navier-Stokes equations are solved away from the wall. Various methodologies are used to switch between the RANS and LES. Spalart et al. [42] proposed Detached Eddy Simulation (DES) for separated flows in which a characteristic turbulent length scale (distance from the wall) was used as a criterion to switch between the RANS and LES regions in the Spallart-Almaras Model (SA) [42]. The original use of the SA model for DES has been extended to other two-equation turbulence models in which the characteristic turbulent length scale is obtained from the model itself and is not dependent on the distance from the wall (e.g. Strelets [43]) These hybrid RANS-LES models have the capability to simulate complex flows but still suffer from a high grid resolution

requirement in the wall normal direction which requires that the first grid point satisfy $y^+ < 1$, while affording some relief in the grid resolution required in the wall parallel directions. Compatibility of the turbulence conditions at the RANS-LES interface and aliasing effects due to the resolved and modeled turbulence are major challenges in this method. In spite of these issues, this method has been applied to a number of complex flows with good results (e.g. [43]).

Another approach based on a zonal model or two-layer model (TLM) solves boundary layer type equations in the inner layer [50] on a virtual grid in the wall layer. This grid is embedded in the outer LES grid and refined only in the wall normal direction. The method is based on the fundamental assumption that the outer and near wall regions are weakly coupled. In the outer LES grid, the filtered Navier-Stokes equations are solved, while in the inner layer Equation (3.18) is solved on a virtual grid embedded between the first grid point off the wall and the wall.

$$\frac{\partial \bar{u}_i}{\partial t} + \frac{\partial}{\partial x_i} (\bar{u}_n \bar{u}_i) = -\frac{\partial \bar{p}}{\partial x_i} + \frac{\partial}{\partial x_n} \left[(\nu + \nu_t) \frac{\partial \bar{u}_i}{\partial x_n} \right] \quad (3.18)$$

In Equation (3.18), n is the wall normal direction and i takes values 1, 2 or 1, 3 based on the wall orientation. The wall normal velocity u_n is computed using mass conservation in the inner layer. Equation (3.18) is solved using the no-slip boundary condition at the wall, and the velocity at the first grid point off the wall which is calculated from the outer-flow LES. The wall-stress components in the streamwise and spanwise directions, obtained from the integration of Equation (3.18) in the inner layer are used as the boundary conditions for the outer-flow LES calculation. This procedure is costlier than the equilibrium wall models but still very inexpensive compared to the wall layer resolved LES because the inner layer calculations take a very small

percentage of the total cost of the whole calculation. Also the pressure Poisson-equation need not be solved in the inner layer as the pressure field just outside the inner layer is imposed on the inner layer. Balaras and Benocci [50] and Balaras et al. [51] used an algebraic eddy viscosity model to parameterize all scales of motion in the wall layer. The zonal approach has been successfully applied to a variety of problems in recent years. Cabot and Moin [52] simulated the flow over a backward facing step, Wang and Moin [53] studied flow past an asymmetric trailing edge, and Tessicini et al. [54] simulated the three-dimensional flow around a hill-shaped obstruction with the zonal near wall approach.

3.4.1 Modified Two Layer Model for Complex Geometries

The two layer wall model is formulated by solving a reduced set of simplified equations in the inner wall layer. The inner layer equations are solved on a virtual embedded grid between the first off-wall grid point ($y^+ < 50$) and the wall. The coupling between the inner and outer layer is accomplished by using the instantaneous outer flow velocity as a boundary condition to the inner layer, which is used to compute the wall shear stress by solving a suitable set of reduced equations. The wall shear stress is then used as a boundary condition in the solution of the outer layer equations at the first off-wall node.

In Cartesian geometries, the normal and tangential velocities at a surface are aligned with the x, y, z coordinates and with the grid as is implied in Equation (3.18). However, this is not the case in a general body-fitted non-orthogonal grid, in which the local (ξ, η, ζ) coordinates are typically not aligned with the normal and tangent directions at the wall, nor are they aligned with the physical coordinate system (x, y, z) and the Cartesian velocities (u, v, w) . Hence special

consideration has to be given to the application of wall layer modeling. To this effect, we formulate a reduced set of equations in local wall coordinates (n, t) . Instead of solving three separate equations in the inner layer (one for each component of velocity), an effective tangent momentum transport equation is constructed. Under the assumption that the normal and tangential unit vectors vary slowly along the wall, reduced dimensionality boundary layer type equations are written for the transport of normal and tangential momentum in the inner layer as:

$$\frac{\partial u_t}{\partial t} + \frac{\partial u_n}{\partial n} = 0 \quad (3.19)$$

$$\frac{\partial u_t}{\partial T} + \frac{\partial(u_t u_n)}{\partial n} + \frac{\partial(u_t^2)}{\partial t} = -\frac{\partial P}{\partial t} + \frac{\partial}{\partial n} \left[\left(\frac{1}{\text{Re}} + \frac{1}{\text{Re}_t} \right) \frac{\partial u_t}{\partial n} \right] + S_u \quad (3.20)$$

with boundary conditions, $u_t = u_n = 0$ at the wall and $u_t = \|\bar{U}_t\|$ and $u_n = \|\bar{U}_n\|$ at the interface with the outer flow. Here, the pressure gradient is assumed constant in the inner layer and is calculated at the first off-wall grid point.

Equations (3.19) and (3.20) can be solved on a two dimensional virtual grid aligned in the normal and tangential direction in the inner layer. Considerable simplifications result if the convection and time derivative terms in Equation (3.20) are neglected, reducing the number of independent variables to one spatial dimension (n), allowing the solution of a tri-diagonal system of equations at each station along the normal to the wall.

$$\frac{\partial}{\partial n} \left[\left(\frac{1}{\text{Re}} + \frac{1}{\text{Re}_t} \right) \frac{\partial u_t}{\partial n} \right] = \frac{\partial P}{\partial t} \quad (3.21)$$

with $u_t = 0$ at the wall and $u_t = \|\bar{U}_t\|$ at the edge of the inner layer.

The eddy-viscosity is modeled [29] by

$$\begin{aligned}
\frac{1}{\text{Re}_t} &= \frac{\kappa}{\text{Re}} d^+ \left(1 - e^{-d^+/A}\right)^2 \\
d^+ &= \rho u_\tau d / \mu \\
u_\tau &= \sqrt{\|\tau_w\| / \rho}
\end{aligned} \tag{3.22}$$

where κ is the von Karman constant, d is the normal distance from the wall, and $A=19$. The one-dimensional equation is solved iteratively (for u_t and $\|\tau_w\|$) by using a standard tri-diagonal solver for a second-order central difference approximation.

From the solution of Equation (3.21), the magnitude of the tangential shear stress is calculated as

$$\|\tau_w\| = \left(\frac{1}{\text{Re}} + \frac{1}{\text{Re}_t} \right) \frac{\partial u_t}{\partial n} \Big|_{\text{wall}} \tag{3.23}$$

which is then decomposed into the respective directional components as

$$\vec{\tau}_w = \|\tau_w\| \vec{t} = \|\tau_w\| t_x \vec{e}_x + \|\tau_w\| t_y \vec{e}_y + \|\tau_w\| t_z \vec{e}_z \tag{3.24}$$

where \vec{t} is the unit tangential vector and

$$\left(\frac{1}{\text{Re}} + \frac{1}{\text{Re}_t} \right) \frac{\partial u_t}{\partial n} \Big|_{\text{wall}} = \|\tau_w\| t_i \tag{3.25}$$

The calculated stress components at the wall can now be directly incorporated into the discretized momentum equations (Equation 3.2) at the first off-wall grid point in the outer layer. For example, the viscous term in the η -direction in Equation 3.2 can be expressed in terms of a surface normal gradient as shown below.

$$\frac{\partial}{\partial \eta} \left(\left(\frac{1}{\text{Re}} + \frac{1}{\text{Re}_t} \right) \sqrt{g} g^{2k} \frac{\partial u_i}{\partial \xi_k} \right) = \frac{\partial}{\partial \eta} \left(\left(\frac{1}{\text{Re}} + \frac{1}{\text{Re}_t} \right) \sqrt{g^{22}} \sqrt{g} \left(\frac{\partial u_i}{\partial n} \right)_\eta \right) \quad (3.26)$$

where the index 2 refers to the local η -coordinate and n is the surface normal direction.

Applying the finite-volume operator at the first off-wall node

$$\begin{aligned} \frac{\partial}{\partial \eta} \left(\left(\frac{1}{\text{Re}} + \frac{1}{\text{Re}_t} \right) \sqrt{g^{22}} \sqrt{g} \left(\frac{\partial u_i}{\partial n} \right)_\eta \right) = & \left\{ \left(\frac{1}{\text{Re}} + \frac{1}{\text{Re}_t} \right) \sqrt{g^{22}} \sqrt{g} \left(\frac{\partial u_i}{\partial n} \right)_\eta \right\}_{north} \\ & - \left\{ \left(\frac{1}{\text{Re}} + \frac{1}{\text{Re}_t} \right) \sqrt{g^{22}} \sqrt{g} \left(\frac{\partial u_i}{\partial n} \right)_\eta \right\}_{south} \end{aligned} \quad (3.27)$$

If either of the η -faces of the cell is a wall then

$$\left(\frac{1}{\text{Re}} + \frac{1}{\text{Re}_t} \right) \sqrt{g^{22}} \sqrt{g} \left(\frac{\partial u_i}{\partial n} \right)_\eta \Big|_{wall} = \frac{1}{\text{Re}} \frac{\partial u_i}{\partial n} \Big|_{wall} \cdot d\Omega = \|\tau_w\| t_i \cdot d\Omega \quad (3.28)$$

where $d\Omega$ is the cell surface area at the wall and t_i are the directional components of the unit tangential vector to the surface. Substitution of the directional stress in the respective momentum equation completes the coupling between the inner and outer layer. This formulation is much more consistent in complex geometries in lieu of solving for three separate components of tangential velocity in each of the three directions and can be extended to any surface and any grid type.

3.4.2 Zonal Two Layer Heat Transfer Model

An equivalent form to Equation (3.20) can be written for the energy equation in the inner layer as

$$\frac{\partial \theta}{\partial T} + \frac{\partial(u_n \theta)}{\partial n} + \frac{\partial(u_t \theta)}{\partial t} = \frac{\partial}{\partial n} \left[\left(\frac{1}{\text{Re} \cdot \text{Pr}} + \frac{1}{\text{Re}_t \cdot \text{Pr}_t} \right) \frac{\partial \theta}{\partial n} \right] + S_\theta \quad (3.29)$$

In the absence of additional source terms and negligible advection, it can be simplified to

$$\frac{\partial}{\partial n} \left[\left(1 + \frac{\text{Re} \cdot \text{Pr}}{\text{Re}_t \cdot \text{Pr}_t} \right) \frac{\partial \theta}{\partial n} \right] = 0 \quad (3.30)$$

Solution of Equation (3.30) requires the closure model for the turbulent Prandtl number. For the current investigation, the formulation of Kays [55] is used and presented in Equation (3.31).

$$1/\text{Pr}_t = 0.58 + 0.22 \left(\frac{\text{Re}}{\text{Re}_t} \right) - 0.0441 \left(\frac{\text{Re}}{\text{Re}_t} \right)^2 \left\{ 1 - \exp \left[\frac{-5.165}{\left(\frac{\text{Re}}{\text{Re}_t} \right)} \right] \right\} \quad (3.31)$$

This formulation accounts for the higher values of turbulent Prandtl number very close to the wall and its gradual decay away from the wall. Experimental investigations as well as numerical simulations of wall bounded turbulent flows have shown [55] that values of turbulent Prandtl number are higher near wall ($y^+ < 15$) as against to approximately constant value away from the wall. Equation (3.30) is solved in the inner layer zonal mesh in a same way that Equation (3.20) is solved. The temperature at the first LES grid point off the wall and either a specified wall temperature or a surface heat flux are used as boundary conditions for solving Equation (3.30). Treatment of the two different wall boundary conditions is discussed below.

Dirichlet boundary condition

If the temperature at the wall is specified, then Equation (3.30) is solved to obtain the temperature profile in the inner region to obtain the heat flux at the wall. The heat flux at the wall is obtained using Equation (3.32) as

$$q'' = - \left(1 + \frac{\text{Re Pr}}{\text{Re}_t \text{Pr}_t} \right) \frac{d\theta}{dn} \Big|_{\text{wall}} \quad (3.32)$$

This heat flux is used as a boundary condition for the outer LES grid instead of using the specified wall temperature similar to the approach for velocity model.

Neumann boundary condition

If the heat flux at the wall is specified, then there is no change in the energy equation calculation for the outer layer. Equation (3.30) is solved in the inner layer to obtain the accurate wall temperature using the outer LES wall temperature and specified wall heat flux as a boundary condition. The temperature profile obtained from solving Equation (3.30) in the inner layer is used to calculate the wall temperature as follows

$$\theta_{\text{wall}} = \theta_{i2} + \frac{\Delta d}{\left(1 + \frac{\text{Re Pr}}{\text{Re}_t \text{Pr}_t} \right)} \quad (3.33)$$

where, θ_{i2} is the temperature at the first off wall inner layer nodal point, Δd is the non-dimensional distance from the wall, and q'' is the non-dimensional heat flux at the wall.

3.5 Turbulent Inlet Boundary Condition

Another challenge in performing LES is the specification of turbulent inlet boundary conditions, to reproduce “real turbulence” matched to experimental measurements. Traditionally, in the RANS framework, the description of the inlet flow data is limited to *a priori* knowledge of statistical quantities like mean mass flow rate or a mean velocity and turbulent kinetic energy. Instead in unsteady LES computations, it is required that the inlet data have time and space

dependent velocity signals representative of the inflow turbulence. It is also desired that the inflow boundaries in spatially evolving flows be placed as close to regions of interest as possible to reduce the computational effort. This makes accurate specification of inflow data even more critical as downstream predictions depend on it.

The most accurate method for specifying the instantaneous velocity fluctuation for LES or DNS is to run a precursor simulation. These precursor simulations can use periodic boundary conditions in the streamwise direction. The time-dependent flow-field is then scaled to satisfy the requirements of the actual simulation. Kaltenbach et al. [56] and Friedrich and Arnal [57] used the velocity profiles extracted from planes in a precursor periodic channel flow to generate inflow data for a LES of a plane diffuser and a backward-facing step, respectively. This method requires significant amount of computational resources and storage space and leads to the introduction of artificial modes caused by recycling a finite number of frames [58]. Hence, there is a need to develop a generic method to simulate inlet turbulence synthetically without resorting to additional precursor simulations.

Lund et al. [59] proposed a rescaling/recycling method for generating inlet conditions for a zero pressure gradient boundary layer. This method uses the velocity in a plane several boundary layer thicknesses downstream of the inlet (the rescaling station) to calculate the velocity signal at the inlet plane. At the rescaling station, the velocity field is decomposed into a mean and fluctuating part. Then the rescaled velocity is taken as a boundary condition at the inlet. Lund et al. [59] have shown that this procedure results in a spatially evolving boundary layer simulation that generates its own inflow data. Planes of velocity data can be saved from

precursor simulations using this procedure and then used as an inflow boundary condition for the main simulation. Aider and Danet [60] used this procedure to generate inlet conditions for turbulent flow over a backward-facing step. Wang and Moin [61] generated inlet conditions for a hydrofoil upstream of the trailing edge using the same procedure. Sagaut et al. [62] extended this procedure to compressible flows. This new proposed procedure uses rescaling and recycling of the pressure and temperature fluctuations in addition to the usual operations performed in the original method.

Spectral methods for synthetic turbulence generation use Fourier decomposition of the velocity field to increase the energy in the lowest modes of the inlet signal. Batten et al. [63] and Smirnov et al. [64] suggested the use of a limited number of random Fourier modes drawn from a random distribution whose frequencies can be rescaled by the local turbulent length and time scales. These fluctuations are rescaled in order to produce a synthetic signal with the target Reynolds stresses. Davidson [65] proposed a method where isotropic synthetic fluctuations are generated at each time step using Fourier modes. These fluctuations are then correlated in time using a time filter.

In summary, a number of methods have been used in the literature to generate inlet boundary conditions. There is a need for a simple, general, computationally inexpensive method for generating inlet turbulent boundary conditions accurately. In many flows, inlet turbulence has a much larger impact on the accuracy of predictions than the LES model itself and hence it is critical that any developments in wall models be done in conjunction with the accurate representation of inflow turbulence. The method used for simulating the inlet turbulence in the

current study is based on the work of Jarrin et al. [66] which is based on generating coherent structures in the inlet plane of the computational domain defined by a kernel shape function based on the integral length scale.

3.5.1 Synthetic Eddy Method Formulation

The synthetic eddy method uses randomly distributed eddies in an eddy box around the inlet plane with a velocity shape function associated with each eddy [66]. The eddies behave much like real eddies in that they convect in the eddy box based on the mean velocity of the flow. Inlet turbulence is generated by taking the collective effect of all the eddies on the velocity nodes in the inlet plane, conditioned by the target turbulent statistics. The net result is the generation of instantaneous turbulence which is spatially and temporally correlated based on the target integral length scales and the mean velocity profile input into the method.

An eddy box is formed around the inlet plane using the known length scales $l_{i,j}$ of each velocity component i , in each direction j with bounds defined by following two equations.

$$x_j^+ = x_j + \max(l_{ij}) \quad (3.34)$$

$$x_j^- = x_j - \min(l_{ij}) \quad (3.35)$$

The instantaneous velocity signal at each nodal point in the inlet plane is expressed as the cumulative effect of local velocity fluctuations from each eddy around it.

$$u_i(x_j, t) = U_i(x_j) + \sqrt{\frac{1}{N} \sum_{s=1}^N \varepsilon_i^s f_{i,j}^s dx_i^s} \quad (3.36)$$

The shape function f here is represented as

$$f_{l_{i,j}} dx_i^S = \sqrt{vol_c} \frac{1}{l_{i1}} f\left(\frac{x_1 - x_1^S}{l_{i1}}\right) \frac{1}{l_{i2}} f\left(\frac{x_2 - x_2^S}{l_{i2}}\right) \frac{1}{l_{i3}} f\left(\frac{x_3 - x_3^S}{l_{i3}}\right) \quad (3.37)$$

where vol_c is the total volume of the eddy box, N is the number of eddies, ε_i^S is the intensity of each eddy, and x_i^S represents the position of each coherent structure (eddy). Initial placement of the coherent structures is taken from a uniform distribution over the eddy box volume. Intensities of the coherent structures are given as

$$\varepsilon_i^S = r_{ij} c_j^S \quad (3.38)$$

where r_{ij} is the Cholesky decomposition of the target Reynolds stress tensor R_{ij} [67] and c_j^S are independent random variables taken from a distribution with zero mean and variance of unity. In the current study, the shape function f which characterizes the decay of perturbations created by each eddy around its center is represented as

$$f_l(r) = \begin{cases} \sqrt{\frac{3}{2l} \left(1 - \left|\frac{r}{l}\right|\right)} & \text{if } |r| < l \\ 0 & \text{otherwise} \end{cases} \quad (3.39)$$

The eddies are convected through the inflow plane with the bulk mean velocity U_b to ensure that the synthetically generated signal is correlated in time.

$$x_i^S(t + dt) = x_i^S(t) + U_{b,i} dt \quad (3.40)$$

Once the coherent structure is convected outside the eddy box, it is regenerated upstream and its intensities are calculated again.

For the effective and accurate implementation of this method, data regarding the turbulent stress tensor and turbulent integral length scales is required at the inlet plane.

3.6 Figures

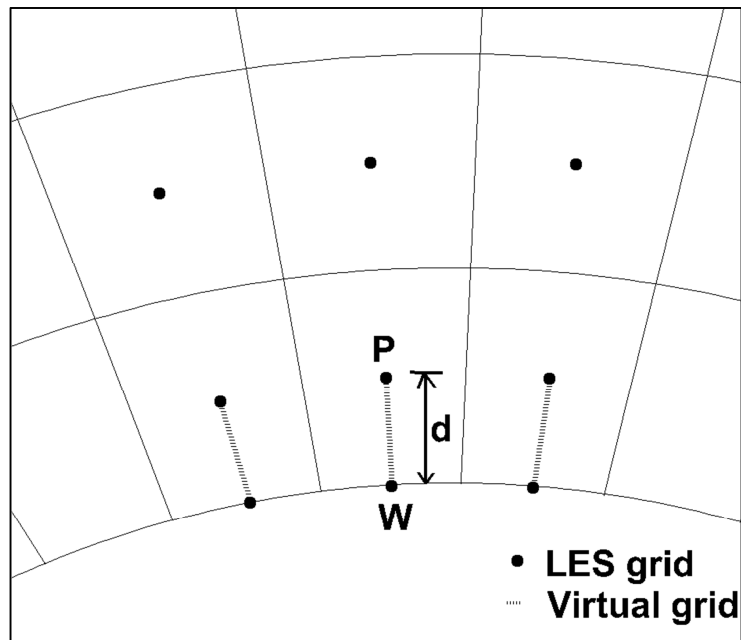


Figure 3.1 Virtual grid for wall model, embedded in LES grid (W represent wall node, and P the off wall outer LES node)

Chapter 4

Validation of Wall Model and Synthetic Eddy Method

The objective of this chapter is to carry out a detailed validation of the two-layer wall model (TLM) and the synthetic eddy method (SEM) in attached as well in flows involving separation. Three different problems are considered, fully developed turbulent channel flow up to a Reynolds number of 2×10^6 , developing channel flow, and flow over a backward facing step at $Re=40,000$. A detailed validation of the wall modeling and synthetic eddy formulation is carried out in a fully developed and developing turbulent channel flow, respectively. Both of these approaches are then applied to the backward facing step geometry of Driver and Seegmiller [68] at a Reynolds number of 40,000. It is the first LES, wall modeled or otherwise, of this geometry at the high Reynolds number of 40,000. Previous LES studies [69-73] have mostly focused on the geometry of Jovic and Driver [74] and Kasagi and Matsunaga [75] at Reynolds number (based on step height) up to 5000. In all cases presented in this chapter, detailed predictions of mean and turbulent quantities are compared to available DNS and experimental data.

4.1 Fully Developed Turbulent Channel Flow

The wall modeled LES (WMLES) formulation is tested and validated in a turbulent channel flow for Reynolds number (Re_τ , based on shear velocity and channel half width) range of 395-20,000. The computational domain spans $2\pi\delta \times 2\delta \times \pi\delta$ in physical x, y, and z direction respectively, where $\delta=1$ is the channel half width. The grid sizes range from $(32 \times 16 \times 32)$ for $Re_\tau=395$ to $(160 \times 96 \times 160)$ for $Re_\tau=20000$. A calculation summary is provided in Table

4.1. For $Re_\tau=395$ and $Re_\tau=590$, DNS data [76] is available, while for $Re_\tau=2000$, wall layer resolved LES data [77] is available for comparison. The number of virtual nodes in the inner layer were varied from 32 for $Re_\tau=395$ to 96 for $Re_\tau=20,000$.

It was observed that for all calculations, the skin friction was predicted within two percent of the Halleen and Johnston [78] correlation for fully developed turbulent channel flow. Furthermore, for $Re_\tau=2000$, the location of the first off wall LES nodal point was varied from $y^+ = 15$ to $y^+ = 70$ to see its effect on the skin friction prediction. It was observed that the predicted skin friction as well as mean velocity profile is not sensitive to the position of the first off-wall nodal point. Figure 4.1 and 4.2 compares the mean streamwise velocity and Reynolds stress profiles along the channel height with DNS [76] and resolved LES results [77] for $Re_\tau=590$, and $Re_\tau=2000$, respectively. The mean streamwise velocity was predicted in exact agreement with the data, while turbulent stresses showed a maximum error of 15%. Heat transfer wall model along with the velocity wall model is also validated at $Re_\tau=590$. Figure 4.3 compares predictions from WMLES with wall resolved temperature profile. Details of wall resolved calculation are available in Appendix B. Prediction of mean temperature profile from WMLES is in good agreement with resolved LES profile. WMLES predicts the Nusselt number to be 108.5 which is in close agreement with resolved LES value of 106 and value of 105.6 obtained from Dittus-Boelter correlation for fully developed turbulent pipe flows. WMLES calculation without heat transfer wall model results in 25% underprediction of Nusselt number compared with Resolved LES. This represents that it is essential to use both velocity and temperature wall model for accurate predictions of heat transfer on coarse near wall meshes. Comparing the

spatio-temporal resolution for wall resolved LES versus the wall modeled LES for $Re_\tau=590$, the computational complexity was reduced by a factor of 285 by using the wall modeled LES.

For higher Reynolds numbers, there is no validation data available and hence only the mean streamwise velocity profile and skin friction are compared with the log law and the friction correlation, respectively. The profile of the mean streamwise velocity shown in Figure 4.4 for $Re_\tau=20,000$ follows the logarithmic law of the wall. For all Reynolds number investigated, the inner layer calculations take less than 7% of the outer LES calculation time.

It is important to note that the LES calculations without a wall model on the coarse meshes used in this study result in a large underprediction of skin friction and result in highly erroneous predictions of mean flow even at relatively low Reynolds numbers. LES calculations without the wall model on the coarse mesh at very high Reynolds number do not converge towards a stable solution.

4.2 Developing Turbulent Channel Flow

The synthetic eddy method is validated in the LES of a developing turbulent channel flow calculation. DNS simulation results [76] for the Reynolds number (Re_τ) based on shear velocity of 395 are used to generate the synthetic eddies and inlet turbulence at the inlet section of the computational domain. The computational domain size is $12\pi\delta \times 2\delta \times \pi\delta$ with a grid of $768 \times 96 \times 128$ computational cells in the streamwise(x), wall normal (y), and spanwise (z) directions, respectively. Turbulent fluctuations obtained from the Reynolds stresses, and length scales calculated from the turbulent kinetic energy and dissipation rate specified by the DNS simulations were used to construct 1000 randomly placed eddies in the inlet box around the inlet

plane. The dynamic Smagorinsky model is used to capture the effects of subgrid scales. Using the SEM procedure described in the previous section, inlet conditions are generated at each time step. A mass conserving outflow boundary condition is used at the outlet of the domain. Periodic conditions are applied in the spanwise (z) direction.

Figure 4.5 shows that the time mean and turbulent profiles at the inlet plane are reproduced accurately by the synthetic eddy method. As the flow moves into the channel the turbulent profiles maintain their shape and form with minimal changes (see Figure 4.6), unlike inlet boundary conditions constructed using white noise or uncorrelated turbulence which would quickly dissipate. Figure 4.7 shows the evolution of the friction coefficient which drops initially by about 3% but maintains the correct value after about 10 channel half widths into the channel. These results validate that the SEM formulation presented in Chapter 3 not only generates a spatio-temporal correlated signal but also maintains the turbulence throughout the channel.

4.3 Flow over a Backward Facing Step

The backward facing step geometry has been used extensively to validate turbulence modeling capability for separating flows. Though it is one of the simplest reattaching flows, the flow-field is still very complex [79]. Simpson [79] has discussed various complex features of this flow. These kinds of flows occur in various practical industrial applications like diffusers and combustion chambers [56]. Figure 4.8 shows the geometry of Driver and Seegmiller [68] used for computations of the flows in backward facing step geometry. The computational domain starts $4H$ upstream of the step, where H is the step height. The grid resolution used was $280 \times 180 \times 96$ in the computational domain shown in Figure 4.8 which extends from $x/H=0$ to

$x/H=25$ in the streamwise direction, $y/H=0$ to $y/H=9$ in the wall normal direction, and $z/H=0$ to $z/H=3$ in the spanwise direction. The flow Reynolds number investigated was 40,000 based on the step height and bulk mean velocity in upstream channel. The resolution used in the current investigation is at least one order of magnitude smaller than the anticipated resolution for a wall layer resolved calculation. The synthetic eddy method is used to generate inlet turbulence based on the mean velocity and Reynolds stress profiles specified by the experimental LDV data at the inlet plane of the computational domain ($x/H=-4$). Driver and Seegmiller [68] reported that the flow at the inflow plane of the computational domain is fully developed. Hence a wall modeled LES of fully developed channel flow at a matching Reynolds number in the larger upstream channel was performed to obtain good estimates of the eddy length scales. These combined with the experimental turbulent stresses were used to generate the inlet turbulence. The two layer wall model was used to model the near wall turbulence. To the best of our knowledge, this is the first LES study presented on this geometry at a Reynolds number of 40,000.

Figure 4.9 and 4.10 shows the mean representations of the inlet boundary condition compared to the measured profiles at $x/H=-4$. There are some minor differences in the rms and stress profiles, but overall the SEM reproduces the same turbulent statistics as the experiments. It is important to note that the correct replication of the inlet boundary conditions is essential to give good predictions downstream. Figure 4.9 compares WMLES predictions of the mean streamwise velocity (averaged in time and spanwise z direction) at 14 different axial locations with experimental LDV data. Excellent agreement between the predictions and the experiments is found at most of the stations. Only near reattachment, a slight underprediction is observed

compared to experiments. Figure 4.10 compares LES predictions of the Reynolds normal stresses and shear stress at 5 representative axial locations in the computational domain. These locations are at the inlet ($x/H=-4$), in the recirculation region ($x/H=3$), near reattachment ($x/H=6$), and in the recovery/attached region ($x/H=10$, $x/H=14$). At $x/H=3$, the maximum value occurs in the separated shear layer from the step, which shifts towards the wall in the reattachment region. Downstream of reattachment, the Reynolds normal stresses and hence the turbulent kinetic energy as well as the Reynolds shear stresses decay at fast rate for several step heights. Other than the slight underprediction of wall normal stresses near reattachment, most predictions are in close agreement with LDV measurements. The same quality of predictions is evident for all of the 21 streamwise measurement locations at which mean and turbulent stresses are available.

Figure 4.11 shows the predicted wall shear stress downstream of the step. Wall shear predictions are in close agreement with the experimental measurements though it is slightly overpredicted in the recirculation region. Cabot and Moin [52] observed similar trends with a zonal wall model investigation of a similar flow with slightly different configuration and at a comparatively low Reynolds number of 14,000. Yoder and Geogiadis [80] investigated various RANS based models in the same geometry. All the $k-\varepsilon$ RANS models were not able to predict even the trends in wall shear correctly. Only WIND-SST model was able to predict the wall shear in fairly good agreement with the data. The friction factor predicted by WMLES reaches a value of zero at a location around 6.3 steps downstream of the separation point comparing extremely well the measured reattachment length of 6.2 by Driver and Seegmiller [68]. Yoder

and Geogiadis [80] reported that all $k-\epsilon$ RANS models underpredict the reattachment length by a large amount. Figure 4.12 shows the mean flow streamlines in the computational domain. Major flow features like, the flow separation, recirculation region, corner vortex rotating in opposite direction, reattachment, flow recovery and their extents are reproduced well.

4.4 Summary and Conclusions

To overcome the limitations of simulating high Reynolds number flows using LES, the current study combines wall modeled LES with the generation of accurate turbulent inlet conditions. A generalized two-layer wall modeling approach for modeling near wall turbulence is used with a synthetic eddy method at the inlet plane to generate the required turbulent fluctuations. While wall modeling reduces the grid requirements in the near wall region, the synthetic eddy method allows the specification of inlet boundary conditions near regions of interest. The two methods are first validated in fully-developed and developing channel flow and then applied to a backward facing step geometry at $Re=40,000$. Comparisons of mean and turbulent quantities with experiments and DNS results, validates the accuracy of both methods in predicting high Reynolds number separated flow with at least an order of magnitude reduction in computational cost.

4.5 Tables

Table 4.1 Turbulent channel flow calculation summary

| Re_τ | Re_{DH} | Y^+ | ΔX^+ | ΔZ^+ | % error in c_f prediction |
|-----------|-----------|-------|--------------|--------------|--------------------------------|
| 395 | 28,164 | 30 | 78 | 39 | 0.28 |
| 590 | 45,448 | 40 | 79 | 39 | 0.32 |
| 2000 | 177,070 | 50 | 120 | 80 | 0.4 |
| 10000 | 1,014,364 | 100 | 300 | 200 | 1.5 |
| 20000 | 2,310,675 | 150 | 780 | 400 | 1.62 |

4.6 Figures

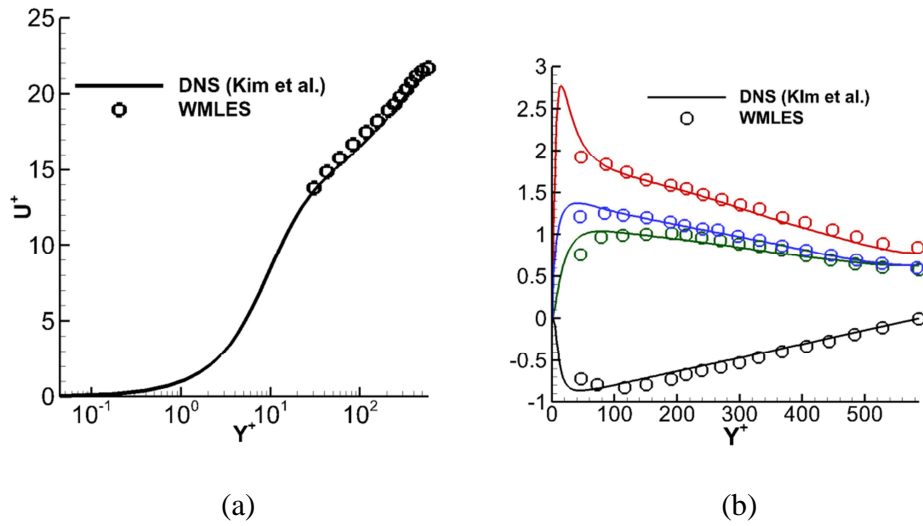


Figure 4.1 Turbulent channel flow results with two layer wall model for $Re_\tau=590$ (a) mean velocity predictions (b) turbulence statistics

(Red- u_{rms} , Green- v_{rms} , Blue- w_{rms} , Black- $u'v'$)

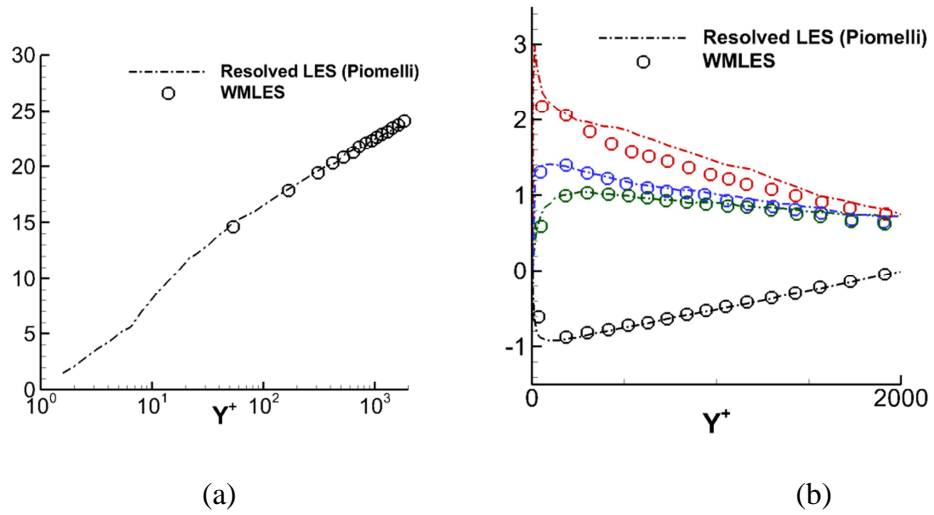


Figure 4.2 Turbulent channel flow results with two layer wall model for $Re_\tau=2000$ (a) mean velocity predictions (b) turbulence statistics
 (red- u_{rms} , Green- v_{rms} , Blue- w_{rms} , Black- $u'v'$)

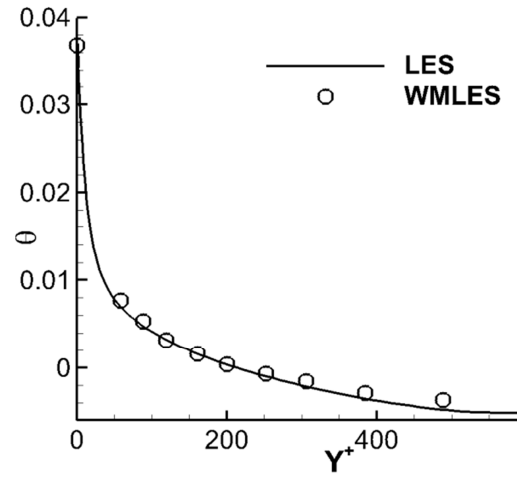


Figure 4.3 Mean non-dimensional temperature prediction with two layer wall model for $Re_\tau=590$

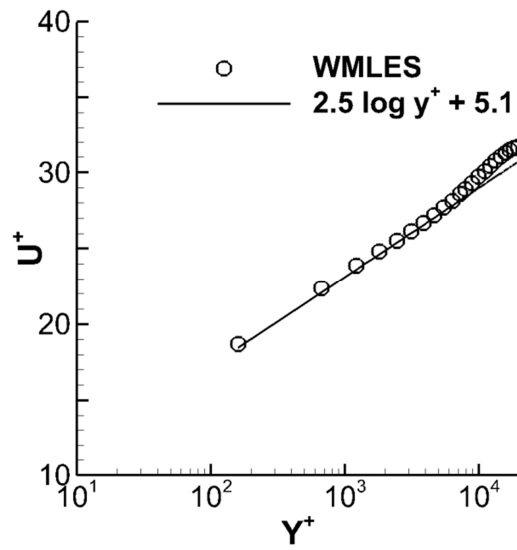


Figure 4.4 Mean velocity prediction with two layer wall model for $Re_\tau=20,000$

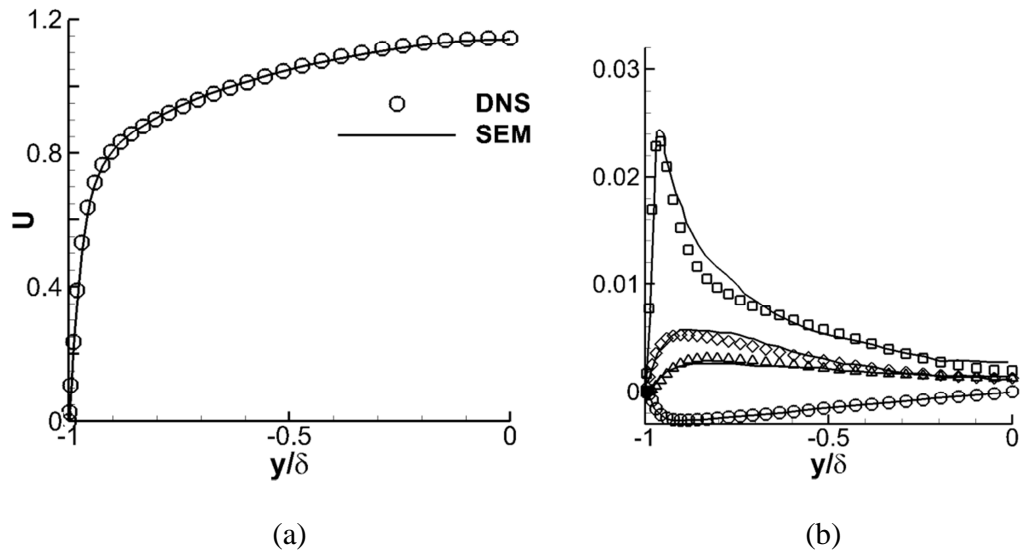


Figure 4.5 Profiles of (a) mean streamwise velocity, and (b) Reynolds stresses at the inlet plane

($\overline{u'u'}$, $\overline{w'w'}$, $\overline{v'v'}$, and $\overline{u'v'}$ in decreasing peak value magnitude order)

(Symbols represent the DNS values, while solid lines represent reproduced values by LES with

SEM. \square - $\overline{u'u'}$, \diamond - $\overline{w'w'}$, Δ - $\overline{v'v'}$, \circ - $\overline{u'v'}$)

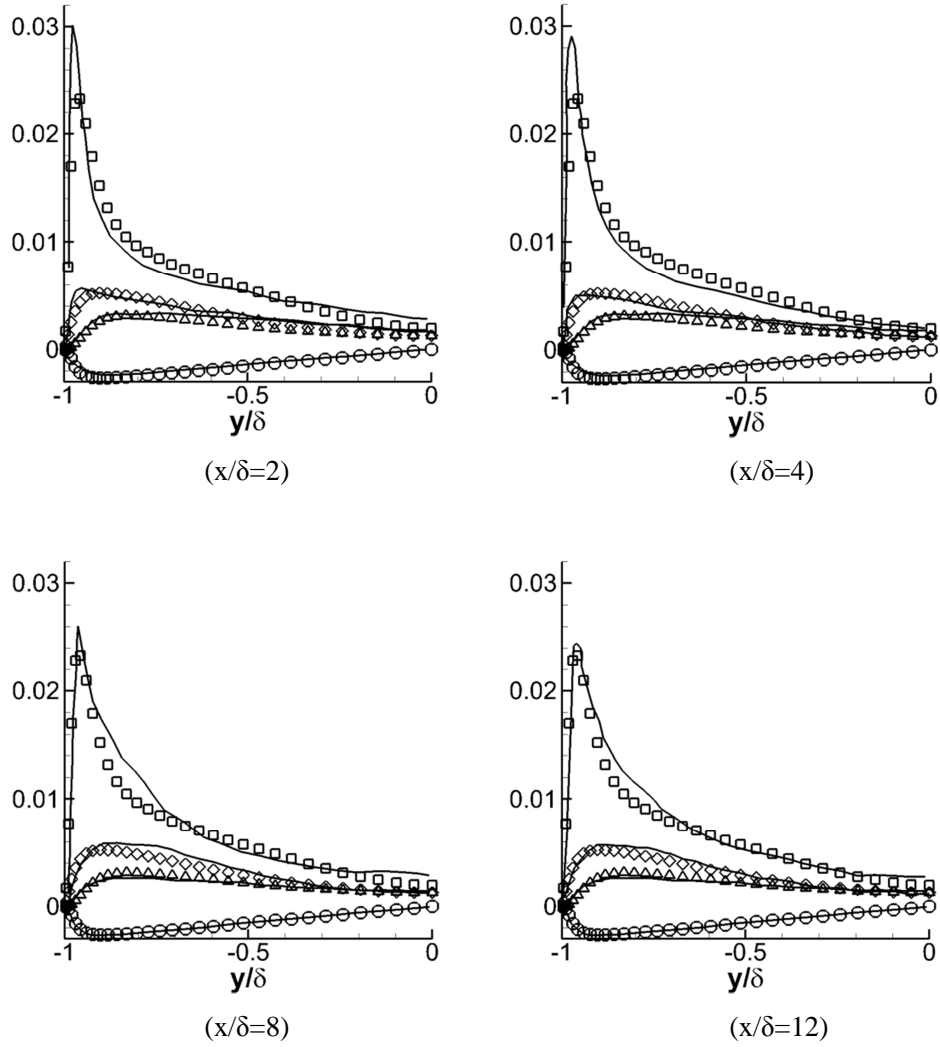


Figure 4.6 Evolution of Reynolds stresses in streamwise direction

(Symbols represent the DNS values, while solid lines represent reproduced values by LES with

SEM at inlet. $\square - \overline{u'u'}$, $\diamond - \overline{w'w'}$, $\Delta - \overline{v'v'}$, $\circ - \overline{u'v'}$)

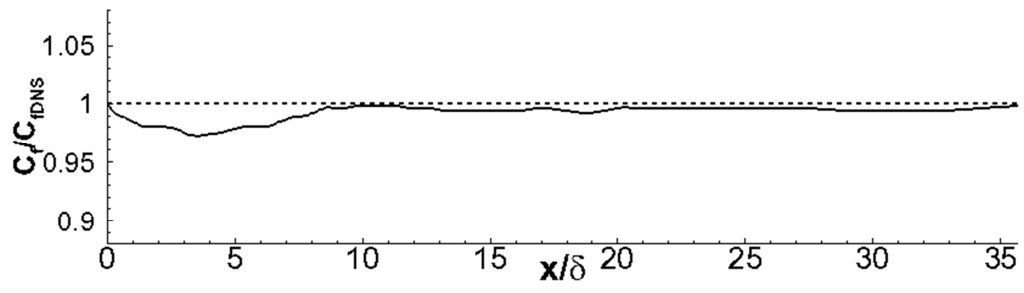


Figure 4.7 Evolution of wall shear stress along the streamwise direction on the channel wall

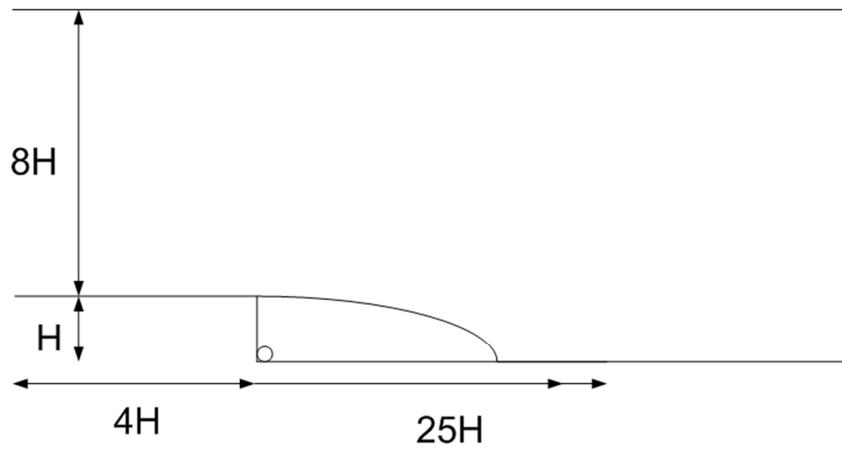


Figure 4.8 Backward facing step geometry of Driver and Seegmiller [68]

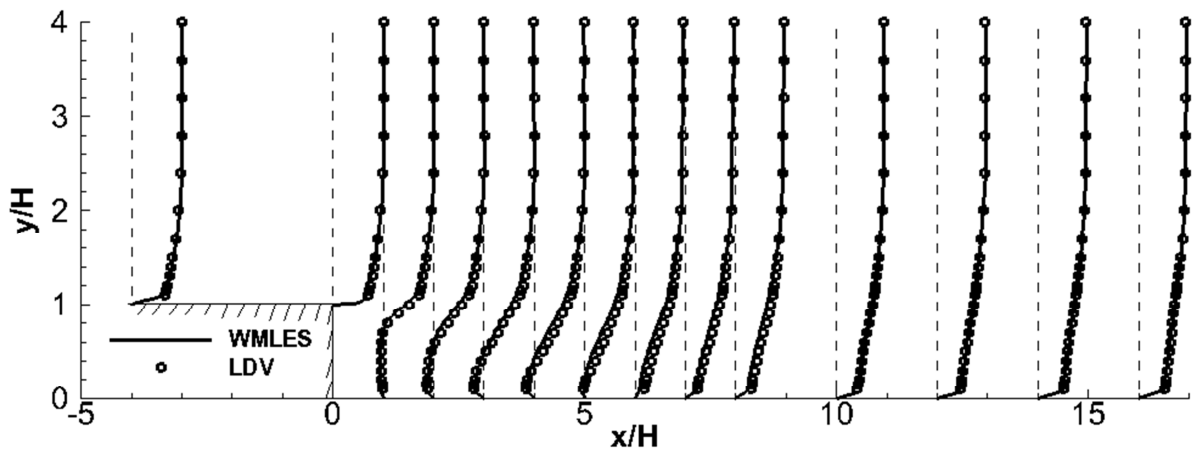


Figure 4.9 Prediction of mean streamwise velocity at various axial locations

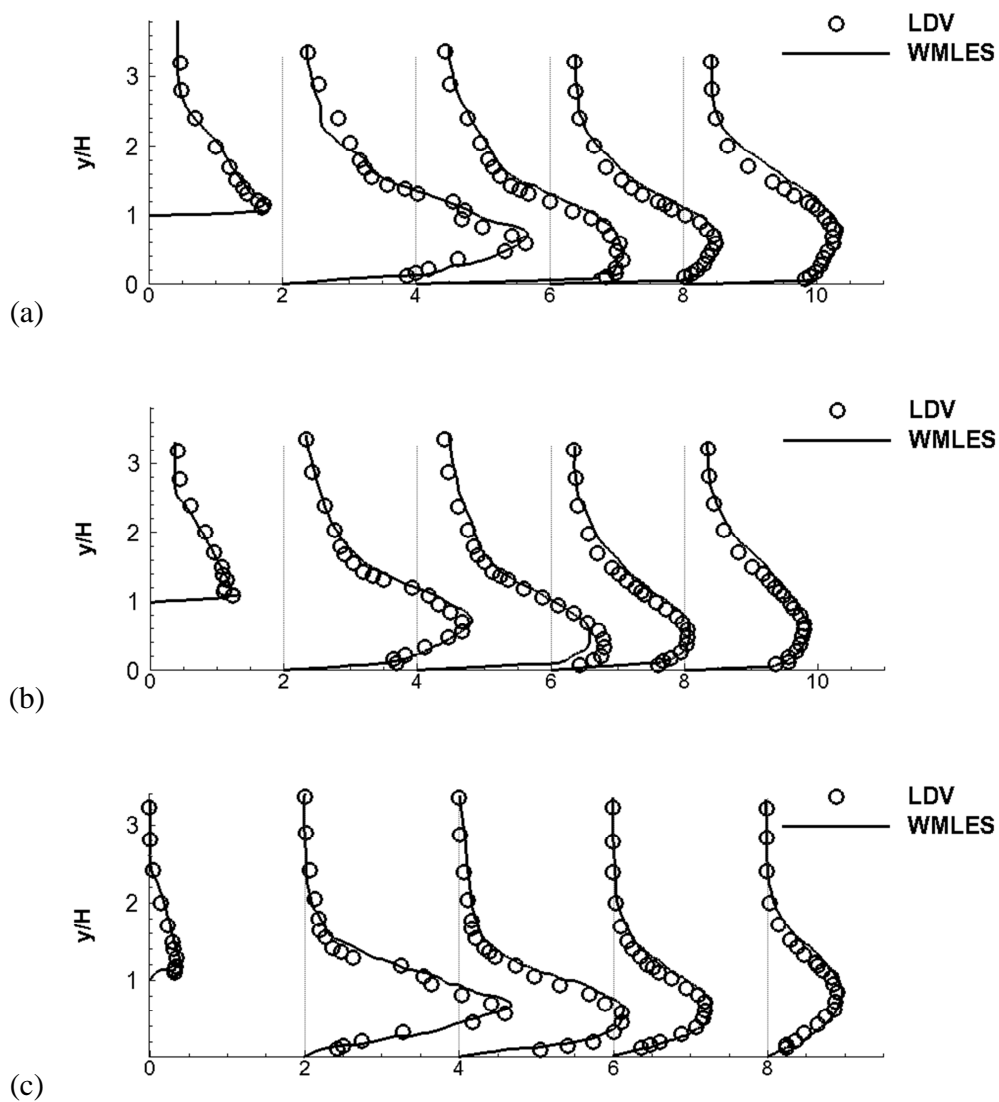


Figure 4.10 Predictions of Reynolds stresses (a) u_{rms} (scale 1:30) (b) v_{rms} (scale 1:30) (c) Reynolds shear stress (scale 1:500)

(Plots at $x/H = -4, 3, 6, 10, 14$ from left to right)

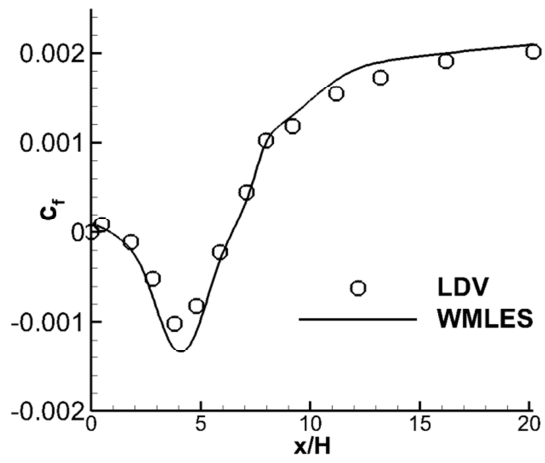


Figure 4.11 Skin friction predictions downstream of the step expansion

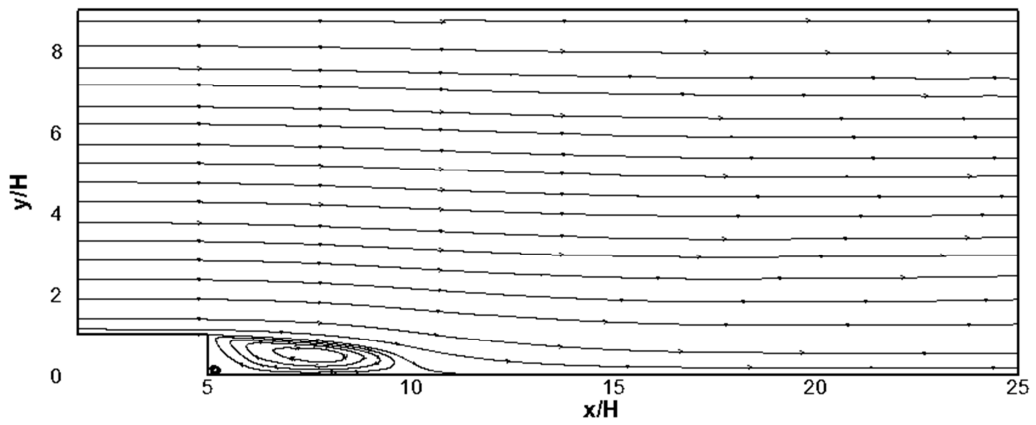


Figure 4.12 Mean flow streamlines in the computational domain

Chapter 5

Large Eddy Simulations of Swirling Flows in Gas Turbine Combustors

The current chapter combines wall layer modeling and the synthetic eddy method (formulated and extensively validated in previous chapters) for performing large-eddy simulations of high Reynolds number turbulent swirling flows. Moderate to highly swirl dominated flow-field in an experimental swirl combustor and an industrial scale can combustor configuration is investigated in the Reynolds number range of 20,000 to 80,000 and corresponding characteristic Swirl number range of 0.43 to 0.7. Flow predictions in the experimental swirl combustor are validated against the detailed experimental measurement data of Wang et al. [81] at twelve axial locations throughout the computational domain. The heat transfer coefficient predictions on an industrial scale can combustor liner wall are validated with the heat transfer experimental data from Patil et al. [82].

Section one gives the background and importance of swirling flows in industrial/engineering applications with relevant literature which deals with their experimental and numerical investigation. Wall resolved and wall modeled calculations at Reynolds number of 20,000 and Swirl number of 0.43 in the experimental swirl combustor geometry of Wang et al. [81] is presented in the second section. Section 3 describes the hybrid RANS-LES simulation performed in an industrial scale can combustor. RANS simulations presented in Chapter 2 are used as precursor simulations to provide the upstream flow information to the LES simulations embedded in the region of interest (can combustor). It is shown that wall modeling and SEM helps in reducing the computational resources and complexity significantly.

5.1 Introduction

Confined swirling flows are important and have wide industrial applications in internal combustion engines, aircraft engines and land based gas turbine combustors, boilers, and industrial burners. Swirling motion in the flow can be developed using a swirler with stationary guide vanes or a tangential flow injection [83]. Strong swirling flows induces an internal recirculation zone which facilitates the fuel-air mixing process, promoting better combustion. Swirl induced internal recirculation zones can also hold the combustion products and radicals in lean premixed combustion to enhance the flame anchoring to the recirculation zone which helps preventing lean blow-off and thermal acoustic instability [81]. Different swirl strengths and combustor geometries result in different recirculation patterns and vortex breakdown regimes. Swirling flows help in reducing the flame length because of higher entrainment and mixing in the shear layer which also improves flame stability and reduces emissions and hence minimizes the burner size [84, 85]. In depth understanding of swirl flow and it's interaction with the combustor liner wall heat transfer is also important in industrial gas turbines to develop better combustor liner cooling schemes [82].

Measurements using hot wire anemometry, Particle Image Velocimetry (PIV) and Laser Doppler Velocimetry (LDV) have been reported on confined swirl flows [81, 86-90]. Experiments can only provide limited data in such a flow-field due to practical limitations but accurate numerical calculations can provide a deeper characterization of many three dimensional complex flow features. But turbulent swirling flows, which are characterized by high strain rates and highly anisotropic turbulence, are difficult to simulate numerically. Several researchers [82,

88, 91-94] have reported Reynolds-averaged Navier-Stokes (RANS) studies on wall bounded swirling flows. RANS models using the Boussinesq hypothesis based on the assumption of isotropic turbulence are inadequate to simulate swirling flows [88]. Other approaches such as large-eddy simulations (LES) have the potential of providing a more physical basis for simulations.

A limited number of studies have been reported in the literature on LES of swirling flows. Grinstein and Fureby [25] presented LES of non-reacting as well as reacting flow in a lean premixed low NO_x model gas turbine combustor and obtained reasonable agreement with experiments. Wang et al. [95] explored various aspects of swirling flow development such as, the central recirculating flow, the precessing vortex core, and the Kelvin-Helmholtz instability in a gas turbine injector. Pierce and Moin [96] investigated a low Swirl number case and obtained promising agreement with experiments, while Kim et al. [97] performed a reactive flow calculation for a high Swirl number case. Garcia-Villalba and Frohlich [98] performed LES of unconfined swirling jets. Most of these studies are at low Reynolds number ($\text{Re} \sim 10^4$) or unconfined flows though recently, Paik and Sotiropoulos [26] performed detached eddy simulations of moderately high Reynolds numbers turbulent swirl flows through an abrupt expansion.

In recent years, industries are showing growing interest in LES. This interest is not to substitute the existing RANS practice but to obtain details of the turbulent flow-field, e.g. aeroacoustic noise generation by vehicles or airfoils in the automotive and aeronautical industries, respectively. Only a small region of interest such as trailing edge of an airfoil or a rear

view mirror of a car needs to be computed by LES. For the embedded LES, upstream conditions can be obtained by performing RANS simulation in the whole geometry at comparatively low computational cost. The major challenge is to generate unsteady inflow data for LES from steady RANS solution. Various methods for developing turbulent inflow conditions are discussed in Chapter 3. The synthetic eddy method (SEM) has the potential to provide a cost effective approach in such situations where it is necessary to limit the size of the embedded LES as close to the region of interest as possible and provide time accurate inflow conditions with available reduced RANS data.

5.2 Experimental Swirl Combustor

This section evaluates the ability of the SEM to represent the inlet turbulence for swirling flows. Time averaged LDV measurement data at approximately two step heights upstream of the combustor is used as input to SEM. The importance of inlet turbulence in swirling flows is investigated by comparing wall resolved LES predictions with a laminar inflow profile versus a SEM generated turbulent inflow profile applied at the inlet plane of the computational domain. The ability of the zonal wall model to represent the near wall region in swirling flows is also evaluated by performing wall modeled LES calculations on relatively coarser meshes as compared to wall resolved calculations. Predictions are compared with the experimental data at various axial locations throughout the computational domain.

5.2.1 Computational Domain

Figure 5.1 describes the computational domain. The computational domain is chosen in the LDV measurement range of the experimental geometry of Wang et al. [81]. The swirl generator is not simulated in the present study. The inflow section of the computational domain is chosen downstream of the swirler and starts at $2.1H$ upstream of the sudden expansion, where H is the expansion step height. Measured mean velocity and turbulent stress profiles at the inlet section are used to simulate the inflow conditions in LES. The computational domain extends till $12H$ downstream of the sudden expansion. Figure 5.1(b) gives the frontal view of the 3D computational mesh while Figure 5.1(c) gives the side view of the mesh. A mass conserving outflow boundary condition is used at the exit of the computational domain. Similar outflow condition in confined swirling flows was used by Wang et al. [81], and Akselvoll and Moin [21] and was found to be appropriate. All the walls are treated as no slip boundaries.

Table 5.1 summarizes the calculations performed. Reynolds number based on inflow section diameter and bulk mean inflow velocity of 20,000 was investigated with wall resolved LES and wall modeled LES (WMLES) at a characteristic Swirl number (S) of 0.43. The Swirl number is calculated following Equation (5.1) which is the ratio of the axial flux of circumferential momentum to the axial flux of axial momentum times the reference inflow section radius. In Equation (5.1), U and U_θ are the mean axial and tangential velocity, respectively. The magnitude of Swirl number is found to be maximum immediately downstream of the sudden expansion.

$$S = \frac{\int_0^R UU_\theta r^2 dr}{R_1 \int_0^R U^2 r dr} \quad (5.1)$$

5.2.2 Inlet Flow Profiles

Figure 5.2 shows the measured time mean averaged velocity and Reynolds stress profiles at the inlet section of the computational domain for a Reynolds number of 20,000 and corresponding characteristic Swirl number of 0.43. Mean velocities are normalized by the bulk flow velocity (U_b) and the Reynolds stresses are normalized by the square of the bulk flow velocity. In this case because of the swirl dominated flow, five Reynolds stresses and three mean velocity components are used to construct the inlet turbulent boundary conditions. These profiles were used in the synthetic eddy method to generate instantaneous velocity profiles at the inflow plane of the computational domain. The reproduced synthetic time averaged mean velocities and Reynolds stresses using wall resolved LES are compared with the respective measured quantities in Figure 5.2. It is observed that the mean velocities and their variances are reproduced very well. Similar observations were noted for the wall modeled LES calculations. It is important to note that all the turbulence quantities predicted downstream of the inflow but before step expansion (at $x/H=-1.05$) are in very close agreement with the experiments. This suggests that the correlations developed by the SEM procedure at the inlet plane are maintained in space and time and do not deteriorate downstream of the inflow plane. SEM is not only able to represent the turbulence at the inlet plane but maintains it in the inflow channel which is crucial in predicting the flow downstream of the sudden expansion.

5.2.3 Grid Resolution

Grid sensitivity studies were performed for the Reynolds number of 20,000 and corresponding characteristic Swirl number of 0.43. Three different grids were tested for resolved

LES calculations with the dynamic Smagorinsky sub-grid scale model. The two high resolution grids had higher near-wall resolution while the third grid is the one used for the WMLES. The WMLES was also tested with two different grids. Table 5.1 gives the summary of different mesh resolutions in the region after the sudden expansion ($0 \leq x/H \leq 12$) used for this grid sensitivity study. Grid 1 (corresponding to Run 1) is the finest grid for wall resolved LES calculations with 9.8 million cells while grid 2 (corresponding to Run 2) is relatively coarse with a total 4.4 million cells. LES calculations on both grid 1 and 2 resulted in predictions without any significant difference. Further coarsening of grid 2 uniformly in all directions results in a deviation from LDV data and hence grid 2 was used for the wall resolved LES calculations.

Grid 3 (corresponding to Run 3) was designed for performing WMLES calculations. It was further refined in the streamwise and circumferential direction to estimate the sensitivity on the predictions. Grid 3 and grid 4 (corresponding to Run 4) resulted in predictions without any significant differences. Further coarsening of grid 4 in all directions uniformly resulted in significant differences with LDV data and hence grid 4 was used in wall modeled LES calculations. Furthermore, LES calculations without any wall model were performed on grid 4 to assess the performance benefits of using the two layer wall model on the coarse grid.

Figure 5.3 presents results of the grid sensitivity study on swirl (tangential) velocity prediction at a representative streamwise location of $x/H=2.1$. Predictions from grids 1 and 2 as well as grids 4 and 5 overlap. The benefit of using the wall model becomes evident in a case where, the LES calculations without wall model on grid 3 produces results which deviate from the experimental results significantly. Use of the no-slip condition on a coarse near-wall mesh

results in erroneous predictions of velocity and Reynolds stresses. Figure 5.3 plots the representative result showing the under prediction of the near wall circumferential velocity. In contrast, use of the two layer wall model helps in predicting all the velocity components and turbulence statistics by providing an accurate representation of wall shear stresses.

Comparing the spatial resolution for wall resolved LES for Run 2 in Table 5.1, and a time step of 1×10^{-4} , Run 4 reduces the computational complexity of the calculation by a factor of 9.

5.2.4 Effect of Inflow Boundary Conditions

As mentioned in Chapter 3, accurate specification of inflow boundary condition is important in performing large-eddy simulations of turbulent flows. This subsection compares the prediction accuracy when turbulent profiles generated by the SEM are used versus the specification of mean profiles without any turbulent fluctuations.

Figure 5.4 compares the predictions from the two different approaches for specifying the inflow conditions at the inlet plane of the computational domain with the LDV data at a representative axial location ($x/H=2.1$). Wall resolved LES calculations were carried out with no-slip boundary condition at the wall on the same grid (Grid 2). Time averaged axial and swirl velocity components and their variances from predictions are compared with the experimental data. It is noted that the use of laminar inflow conditions results in a significant increase in the extent of the recirculation region. This results in predictions of mean flow substantially different than that reported by experiments.

Applying SEM on the other hand, simulates the exact experimental conditions at the inlet plane of the computational domain. All major flow features are reproduced and values of mean velocities and turbulence quantities are in good agreement with the experimental data throughout the computational domain including the representative location shown in Figure 5.4.

5.2.5 Flow Predictions

Swirl flows involve many complex features. The shear layer issuing from the upstream guide pipe separates at the lower edge of the step expansion. This leads to the creation of a corner recirculation zone, which extends from the step expansion to a region where the shear layer impinges on the combustor liner wall. A vortex breakdown process occurs downstream of the expansion which results in an internal recirculation region. The spatial extent of the vortex breakdown process depends on the swirl strength of the issuing shear layer. In this section, through the usage of mean flow-field and turbulence statistics, and flow streamlines, it is demonstrated that the wall resolved and wall modeled LES calculation with synthetic inlet turbulence reproduce these complex swirl flow features. Predictions from these two LES calculations are compared with LDV measurement data at twelve different axial locations in the computational domain. Two of these locations are in the upstream guide pipe while the other ten locations are in the can combustor section. At each axial location, circumferential averaging of the mean flow and turbulent quantities is carried out and their distribution along the radial (wall normal) direction is plotted from the combustor axis to the confining wall. A detailed comparison of all three predicted velocity components and five turbulent Reynolds stresses is presented in Appendix D. For brevity and clarity, predictions only at three representative axial

locations are presented in this chapter. These three locations are chosen to be immediately downstream of the combustor, in the vortex breakdown region, and a location where the turbulent swirl flow starts decaying. Circles represent the LDV measurement data of Wang et al. [81], solid lines, and dashed lines represent predictions from wall resolved and wall modeled LES, respectively.

Time averaged mean velocity profiles are plotted in Figure 5.5. Resolved as well as wall modeled LES calculation were able to predict all three velocity components in close agreement with the LDV data at all stations. The flow impingement or reattachment length is also predicted well. Both methods are able to predict the characteristics of typical weak to moderate swirl flow. Figure 5.5 shows a significant swirl velocity component in the near axis as well as in the shear layer region. LES was able to predict the steep gradients in the swirl velocity accurately in the shear layer as observed in the experiments. It is notable that the wall modeled LES calculation is able to reproduce near wall velocities in all regions of the combustor immediately after the expansion as well as further downstream of it in good agreement with the experiments.

LES calculations are able to predict the variances of all three velocity components at all twelve stations in good agreement with the LDV data. At the first two locations shown in Figure 5.5, the wall modeled LES slightly underpredict the variances compared with the resolved LES. This underprediction is not significant and does not affect predictions further downstream. It is important to note that each variance has significantly different values than the other two indicating strong anisotropies in the flow-field. Figure 5.5 represents that the LES calculations are able to simulate anisotropic turbulence in the flow-field accurately. Also, they predict the

turbulent kinetic energy distribution in the shear layer as well as near the axis of the combustor accurately. Higher magnitude of variances of streamwise and circumferential velocity at the beginning of combustor section, which is one of the characteristics of the swirling flows are captured well by the computations. Reynolds shear stresses are also predicted accurately with LES. Both LES calculations were able to predict the turbulence production in the shear layer as well as in the core region where the vortex breakdown process occurs. Predictions were able to capture the trend, especially the peaks in the Reynolds stress profile in good agreement with the data.

Also, downstream of this internal recirculation zone, the swirl along with turbulence starts decaying. This decay rate is significant and is consistent with the observation reported in the literature [82, 87, 89, 90]. The fast decay in confined flows is due to both the swirling motion and wall friction. Both LES calculations capture these effects accurately.

Figure 5.6 represents instantaneous streamlines from the wall modeled LES calculation. These streamlines shows characteristics of moderate swirl flow. A vortex breakdown process starts near the region of $x/H=1$. An internal recirculation zone is created as a result of this vortex breakdown process. This internal recirculation zone is not axisymmetric and has a bubble shape. The time accurate LES calculations revealed that the shape and position of this internal recirculation zone changes with time. Figure 5.6b represents highly swirling flow in the upstream region of combustor section at $x/H=1$. The center of the large swirling flow is off the axis. At the axis the components of radial and swirl velocities are not zero. The oscillatory motion of the bubble shaped structure with time in the region downstream of the expansion

represents the presence of the precessing vortex core. The swirl strength reduces further downstream. Figure 5.6c represents a decayed swirl flow region at $x/H=5$ downstream of the sudden expansion.

It is notable that the flow developed by the SEM at the inlet plane reproduces the important flow features of swirling turbulent flow, which are significantly different than the non-swirling turbulent flows. Figure 5.5 shows that the values of axial velocities at the center of the combustor axis are quite small compared to the much higher values observed in typical non-swirling flows [82]. The shear layer predicted from LES calculations represents high gradients of the swirl velocity which is also one of the prominent distinguishing feature of swirl flows compared with non-swirling flows. Also, the values of the azimuthal velocities are higher between the axis and shear layer region.

Close agreement of the predictions of mean axial and swirl velocity and their variances with the experimental data in the region downstream of the expansion validate that the vortex breakdown process is predicted accurately by the LES calculations with SEM at the inlet. This is important as the specification of a laminar flow profile a short distance upstream of the expansion is not able to predict the vortex breakdown process and results in a strong jet flow downstream of the expansion which results in distorting the axial velocity and turbulence intensities as reported by Paik and Sotiropoulos [26]. This observation reinforces the argument that it is important to accurately reproduce the inlet turbulence when short development lengths are needed for computational expediency. This is particularly important for practical industrial geometries where there is a need of shorter inlet flow section for various components.

5.3 Hybrid RANS-LES Simulation of an Industrial Scale Gas Turbine Combustor

The major challenges in performing large-eddy simulations on industrial scale gas turbine combustor geometries presented in Chapter 2 were the computational complexities posed by the swirler geometry with unknown upstream inlet turbulence data, and a large overall mesh required to resolve the near wall layer to accurately characterize the liner wall heat transfer. In this section, use of wall layer modeling to mitigate near wall grid resolution requirements and use of the synthetic eddy method to reduce the computational complexity and cost of LES simulations is presented. The major focus of the study presented here is to accurately characterize the liner wall heat transfer using an integrated near wall velocity and temperature zonal model with SEM used to specify the upstream flow conditions to the LES domain embedded in the region of interest (can combustor).

5.3.1 Computational Domain

Figure 5.7 shows the sketch of the experimental and computational geometry. Two computational domains are identified – one which was used by Patil et al. [82] for RANS calculations (red box), which included the swirler in the computational geometry, and the other shorter domain (blue box) which is used in the current LES simulations. The details of the RANS simulations can be found in Patil et al. [82] (also presented in Chapter 2). In order to reduce the computational complexity and cost, the LES domain is selected in the region of interest, which includes the can combustor and a section $0.5H$ upstream of it as shown in Figure 5.7. At the inlet plane of the LES domain, data is extracted from the RANS solution and interpolated onto the LES grid and used for synthetically generating the inlet turbulence.

Figure 5.8 shows the frontal and side view of a three dimensional mesh inside the LES computational domain. A block structured mesh with hexahedral cells is formed using GRIDGEN software tool. The Reynolds number of 50,000 and 80,000 based on the diameter of the can combustor and bulk mean velocity inside it, are investigated. The characteristic Swirl number defined by equation (5.2) has a value of 0.7 at the inlet of the LES domain for the simulations performed.

$$S = \frac{\int_{R_i}^{R_o} UU_{\theta} r^2 dr}{R_o \int_{R_i}^{R_o} U^2 r dr} \quad (5.2)$$

where R_i and R_o are outer and inner radii of the swirl nozzle. The computational mesh consists of $240 \times 138 \times 160$ grid points in the axial, radial, and circumferential directions, respectively. The values of Y^+ on the combustor liner wall were observed to be in the range of 30-60 for the calculations performed. A convective outflow boundary condition is used at the exit of the can combustor which is 20 step heights downstream of the expansion into the can combustor. All the walls were treated as no-slip boundaries. A constant heat flux thermal boundary condition is specified at the combustor liner wall while all other walls are treated as adiabatic with zero heat flux.

5.3.2 Inlet Flow Profiles

Three components of mean velocity and Reynolds stresses are extracted from the RANS solution of Patil et al. [82]. Reduced data is available from the RANS data of Patil et al. [82] in the form of mean velocity, turbulent kinetic energy and its dissipation rate. Figure 5.9 shows the profiles of the three velocity components and turbulent kinetic energy. Mean velocities are

normalized by the bulk mean flow velocity (U_b) and the turbulent kinetic energy is normalized by the square of the bulk mean flow velocity in the combustor. Reynolds normal stresses are extracted from the RANS solution using the following Equation (5.3)

$$R_{ii} = \overline{u_i'^2} = \frac{2}{3} k \quad (5.3)$$

where $i=1,2,3$. The length scales of coherent structures at the inlet plane are calculated using Equation (5.4).

$$l = c_\mu \frac{k^{3/2}}{\varepsilon} \quad (5.4)$$

where k is the turbulent kinetic energy and ε is the dissipation rate of the turbulent kinetic energy and value of constant $c_\mu = 0.0845$. The near wall length scale was limited by the local grid size of the LES, as the length scale calculation based on Equation (5.4) might go to zero at the near wall cell. This limiting criterion also guaranteed that the synthetic coherent structures can be discretized by the LES grid.

5.3.3 Reynolds number 50,000

Flow-field Characteristics

A detailed flow-field analysis is carried out to study various characteristics of the swirl dominated flow inside the combustor and its interaction with the liner wall. Figure 5.10 shows the distribution of the mean axial velocity normalized by the bulk mean combustor velocity in the azimuthal plane ($z=0$). The figure expresses many important mean flow features of the swirl dominated field in the combustor discussed in the previous section. A vortex breakdown process occurs immediately after the step expansion resulting in a swirl induced internal recirculation

region. The separated shear layer from the step attaches on the liner walls about a step height after the expansion. This reattachment length is much shorter than the one observed in non-swirling flows (typical value of reattachment length for non-swirling flows is around 6 step heights) and weak or moderate swirling flows and is a direct consequence of the high swirl in the shear layer. The reattachment length normalized by the step expansion height in this flow is less than half compared to the moderate swirling flow studied in the previous section. Higher swirl strength results in higher spread angle of the shear layer coming out of the swirl nozzle and expanding into the combustor.

To further quantify and analyze the flow-field in the combustor, variation of all three components of the velocity and Reynolds stresses averaged in the circumferential direction was studied throughout the combustor at several axial locations. Figure 5.11 represents the variation of mean axial and swirl velocity, variances of axial velocity and swirl velocity, Reynolds shear stress and turbulent kinetic energy along the radial direction at three representative streamwise locations. These locations are chosen as immediately after the expansion ($x/D=0.1$), near the impingement location ($x/D=0.4$), and further downstream in the region ($x/D=2$) of decaying turbulent swirling flow.

Figure 5.11(a) represents the mean velocity and Reynolds stresses immediately after the step expansion. Mean axial as well as circumferential velocity show significantly higher values in the range of r/D of 0.15 to 0.22 expressing the presence of the shear layer. The mean axial velocity reaches significantly high negative values in the corner circulation bubble near the combustor liner ($r/D=0.5$). It also has slight negative values in the region of $r/D=0$ to $r/D=0.15$

which represents the swirl induced recirculation bubble shown in Figure 5.10(a). The variances of all three velocity components differ considerably from each other. This was observed to a greater extent up to at least four step heights after the expansion. This indicates high turbulence anisotropy in the flow-field. The values of variances of swirl velocity and radial velocity were observed to be significantly high near the step expansion. This is another differentiating feature between swirling and non-swirling flows. This also reflects in the significantly higher values of turbulent kinetic energy seen in Figure 5.11.

Figure 5.11(b) shows that the axial velocity has a very high magnitude near the region of shear layer impingement at the liner wall. The value of swirl velocity is also significantly higher at this location. It is also important to note that the variances of axial and swirl velocity are very high in this region. The turbulent kinetic energy shown in Figure 5.11(b) also exhibits a very high value near $r/D=0.5$ (liner wall).

After the flow impingement location, the turbulent swirling flow was observed to decay at a very fast rate. Figure 5.12(c) represents the mean velocity and Reynolds stresses further downstream. The peak values of axial and swirl velocity are reduced significantly at this location. More importantly, the variances of the mean velocity and swirl velocity have significantly lower values. This indicates the faster decay of the turbulent swirling flow. This observation is consistent with previous observations in the literature [82, 87, 89, 90] and also observed in the moderate swirling flow studied in the previous section.

Liner Wall Heat Transfer

Figure 5.12 compares the predictions from WMLES calculation for Reynolds number of 50,000 with the heat transfer experimental data from Patil et al. [82]. The heat transfer coefficient at the liner wall is characterized by the Nusselt number augmentation ratio, where the baseline Nusselt number is obtained from the Dittus-Boelter correlation for fully-developed pipe flow with heated walls as expressed in Equation (5.5).

$$Nu_0 = 0.023 \times Re^{0.8} \times Pr^{0.4} \quad (5.5)$$

Circumferentially averaged values of Nusselt augmentation are plotted versus the axial distance normalized by the diameter of the can combustor. It can be observed from Figure 5.12 that the predictions of the heat transfer coefficients are in very good agreement with the experimental data. The heat transfer augmentation increases from the beginning of the combustor (immediately after step expansion), reaches a maximum value and then decays at a fast rate. The wall modeled LES predictions follow the trend of heat transfer coefficients measured by the experiment. More importantly, the value of peak heat transfer augmentation predicted by the WMLES is in very close agreement with the experiment. It is also important to note that the location of peak heat transfer predicted by WMLES is in exact agreement with the experimental findings and occurs in the region of shear layer impingement which results in large velocity gradients at the liner wall and high turbulent intensities. The close agreement between experiments and predictions validate all the major components used in the simulations, i.e., accurate reconstruction of instantaneous velocities at the inlet to the computational domain by the SEM using data from a precursor RANS simulation, and accurate modeling of the inner layer velocity and temperature field by the wall model.

5.3.4 Reynolds number 80,000

Flow-field Characteristics

Figure 5.13(a) represents the mean flow streamlines for Reynolds number of 80,000 in azimuthal plane ($z=0$). The streamline pattern is very similar to the one observed for Reynolds number of 50,000. Major flow features exhibit similar behavior for both the Reynolds numbers. A vortex breakdown process occurs immediately downstream of the step expansion resulting in an internal recirculation region. The extent of this internal recirculation region is the same as for the low Reynolds number ($Re=50,000$). More importantly, the size of the corner recirculation zone remains exactly the same for this higher Reynolds number. The spread angle of the highly energetic shear layer issuing from the swirl nozzle is also the same for both the Reynolds numbers. This results in the impingement location of the shear layer on the liner wall to be exactly the same for both Reynolds numbers. Figure 5.13(b) represents the contours of the time averaged mean axial velocity normalized by the bulk mean combustor velocity in the azimuthal plane ($z=0$). The distribution of the normalized axial velocity also behaves the same as for Reynolds number of 50,000. These flow features point out that for the Reynolds number range investigated, the major flow features in the combustor are held fixed by the Swirl number which is constant at a value of 0.7. This observation is consistent with the findings of Patil et al. [82] who noted that even an order of magnitude further increase in Reynolds number does not change the location of shear layer impingement.

Figure 5.14 represent the variation of mean velocity components and Reynolds stresses at three representative streamwise locations. Mean velocity components were normalized by the

bulk mean combustor velocity while the Reynolds stresses are normalized by the square of bulk mean combustor velocity. These quantities are circumferentially averaged and plotted against the radial co-ordinate normalized by the combustor diameter. The variation of mean velocity and their variances follow trends similar to that observed for a Reynolds number of 50,000. This is consistent with the observation previously made that the major flow structures are not dependent on the Reynolds number.

The values of normalized Reynolds stresses are nearly the same as for the lower Reynolds number. This indicates that even though the turbulence production increases with Reynolds number, the normalized values of Reynolds stresses do not increase. The values of turbulent intensities are high near the impingement location which leads to the peak in heat transfer. Figure 5.15 represent the normalized Reynolds normal stresses and axial velocity near the peak location. It is observed that the values of normalized wall normal and azimuthal turbulence intensities near the peak heat transfer location are a little lower for Reynolds number of 80,000. This is also associated with the slightly lower magnitudes of normalized axial velocity.

The turbulent swirling flow starts decaying after the impingement location. The decay rate is fast as observed for the lower Reynolds numbers. From Figure 5.14(c), we can observe that the values of turbulence intensities are very low representing the decayed turbulent swirl flow.

Liner Wall Heat Transfer

Figure 5.16 shows the distribution of Nusselt number augmentation on the combustor liner wall. The heat transfer coefficient distribution correlates with the flow patterns observed. The trends in Nusselt augmentation are similar to Reynolds number 50,000 case. LES is able to predict the trends and magnitudes of heat transfer coefficient in close agreement with the experimental data. It is important to note that the peak Nusselt augmentation has reduced from a value 10.2 to approximately 8. As observed in the flow-field analysis, the normalized turbulence intensities in the wall normal and azimuthal direction are lower for Reynolds number of 80,000. This is also associated with the lower normalized axial velocity in the shear layer near the peak location. These are the major reasons for the drop in the peak heat transfer augmentation with the increase in Reynolds number. The location of peak heat transfer on the other hand remains the same for both Reynolds number. This can be correlated with the observation made in the flow-field analyses that the size of the corner recirculation zone, shear layer spread angle and flow impingement location on the liner wall remains same for both Reynolds number. This is because for the Reynolds number range investigated, the same Swirl number holds the flow features in the combustor constant. Good agreement of the heat transfer coefficient value on the combustor liner wall with the experiments shows that the near wall treatment both for velocity and temperature presented in Chapter 3 is able to accurately represent the inner wall layer in complex turbulent swirling flows at high Reynolds numbers.

5.4 Summary and Conclusions

Wall resolved as well as wall modeled LES calculations are carried out in an experimental swirl combustor at Reynolds numbers of 20,000 and characteristic Swirl number 0.43. Experimental profiles of the time averaged mean velocity and Reynolds stresses are used as input to the synthetic eddy method procedure for generation of inlet conditions. Good agreement of the predictions with the experiments validates that the LES with synthetic turbulence at the inlet can simulate the anisotropic complex swirling flow accurately. It is also shown that specifying the laminar inflow profile in such flows results in erroneous predictions of mean flow and turbulent quantities. The SEM formulation in the current study reproduces all the major swirling flow features. Wall modeled LES calculations were able to predict the profiles of mean velocity, its variances and Reynolds shear stresses in good agreement with the measured data. The use of wall resolved calculation with the same inflow turbulence generation method and subgrid scale model helps in isolating and quantifying the effect of the wall model. It was observed that LES calculation on a grid used with the wall model, but with a no-slip boundary condition resulted in erroneous predictions of the flow profiles.

A hybrid RANS-LES simulation was performed in an industrial scale gas turbine can combustor. Wall modeled LES calculations are performed in the can combustor with SEM used to generate upstream inflow data from a precursor RANS solution. It is observed that the flow-field in the combustor is characterized by a highly energetic shear layer, swirl induced central recirculation zone, corner recirculation zones and fast decay of swirl and turbulence downstream of shear layer impingement on the liner wall. An impinging shear layer, resulting in a steep

velocity gradient and high turbulent intensities, is responsible for very high values of heat transfer augmentation at the peak location. It is observed that at higher Reynolds number the values of normalized turbulence intensities in the wall normal and spanwise direction are lower. This, together with a lower normalized axial velocity in the shear layer near the peak location causes a drop in Nusselt augmentation with the increase in Reynolds number. The major flow structures are held constant by a fixed Swirl number for both Reynolds numbers. This results in very similar flow structure in the combustor with no change in the peak heat transfer location. This successful RANS-LES study demonstrates that the wall modeling and synthetic eddy method helps in reducing the computational complexity and resource requirements in complex flows at high Reynolds numbers.

5.5 Tables

Table 5.1 Calculation summary for experimental swirl combustor

| Case | Swirl number | Reynolds Number | Grid Resolution | Model | Y^+ |
|-------|--------------|-----------------|-----------------|-------|-------|
| Run 1 | 0.43 | 20,000 | 240×180×228 | LES | 1-3 |
| Run 2 | 0.43 | 20,000 | 192×120×192 | LES | 1-5 |
| Run 3 | 0.43 | 20,000 | 148×80×164 | WMLES | 20-40 |
| Run 4 | 0.43 | 20,000 | 128×80×144 | WMLES | 20-40 |
| Run 5 | 0.43 | 20,000 | 128×80×144 | LES | 20-40 |

5.6 Figures

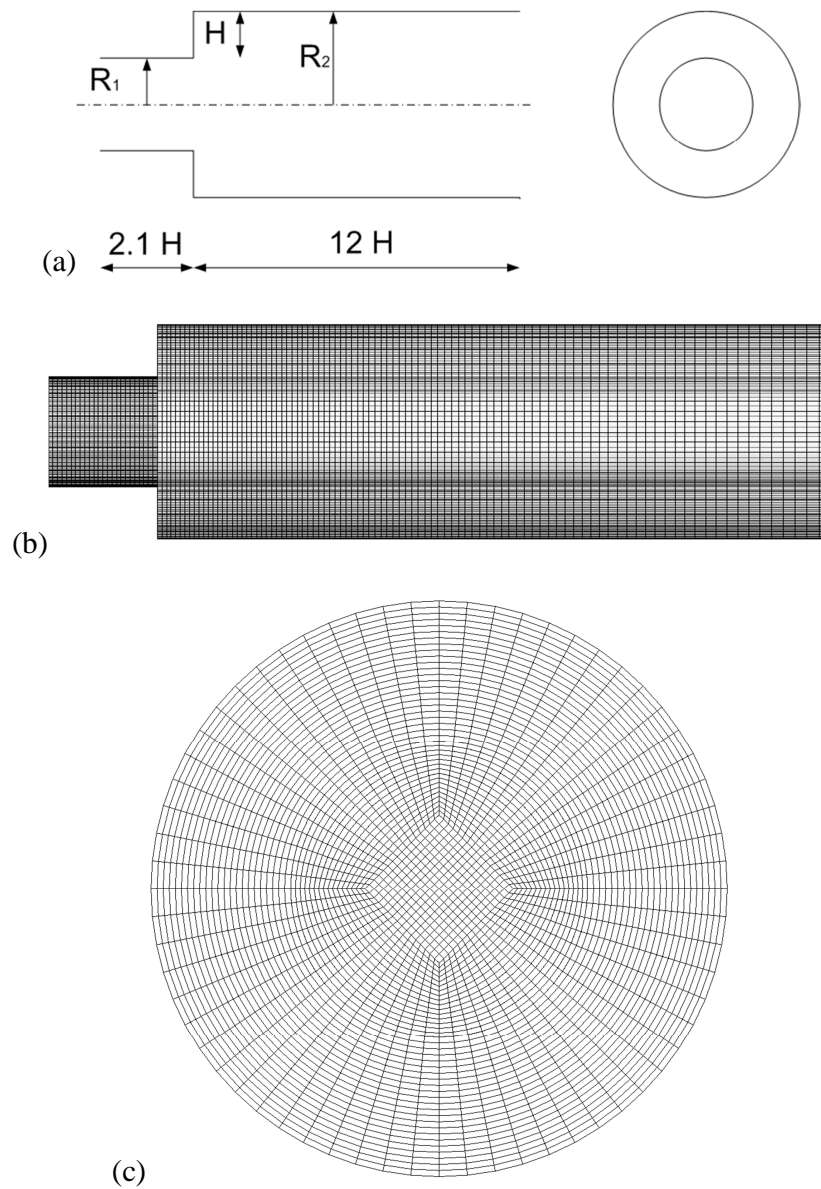


Figure 5.1 Computational domain for experimental swirl combustor (a) sketch with dimensions (R_1 is the reference length scale, $R_2=1.94R_1$, $H=0.94R_1$) (b) frontal view, and (c) side view of the mesh in 3D computational mesh

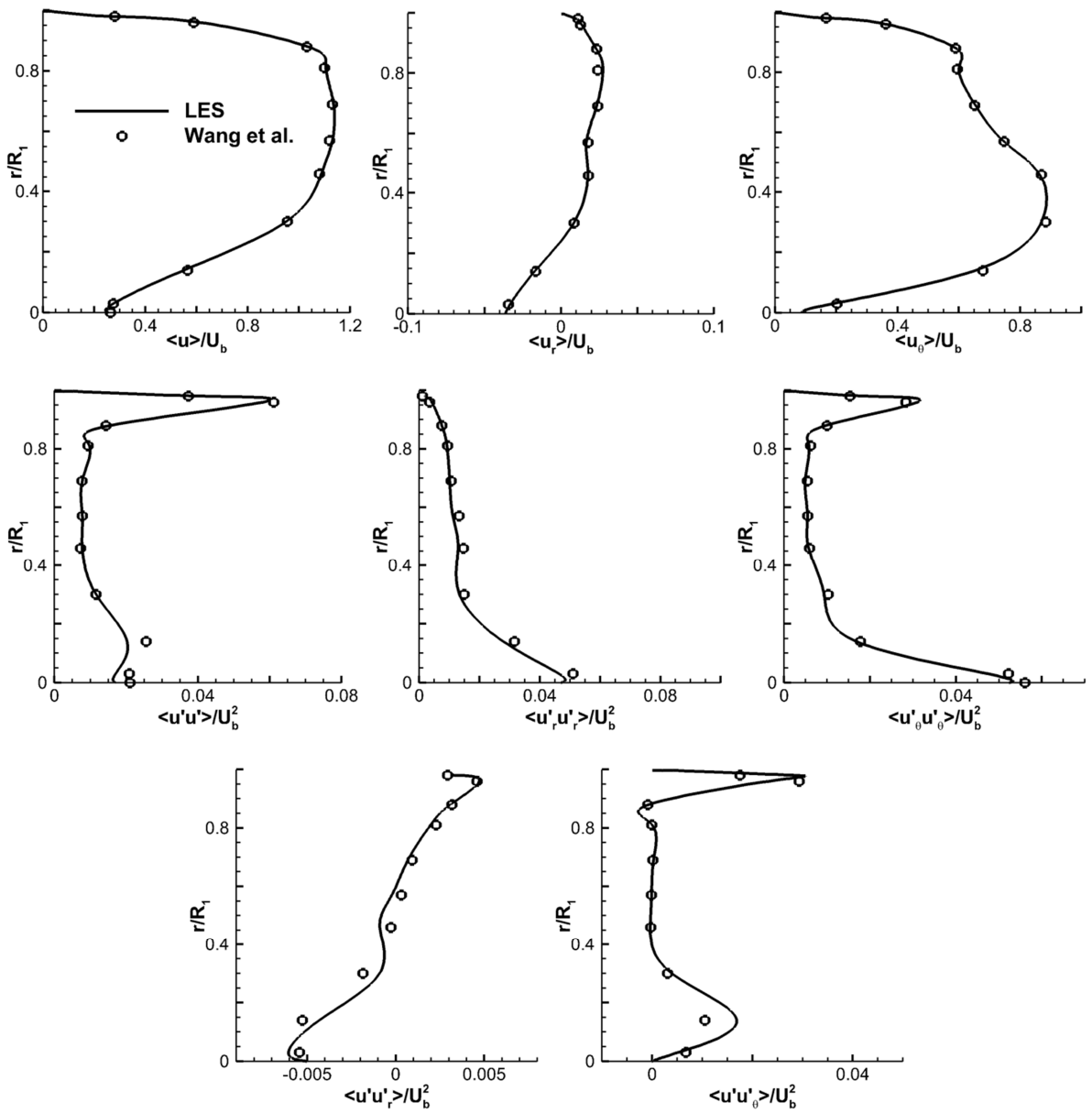


Figure 5.2 Measured and predicted mean velocity and turbulent stress profiles at inlet of the computational domain ($x/H=-2.1$)

($Re=20,000$, $S=0.43$)

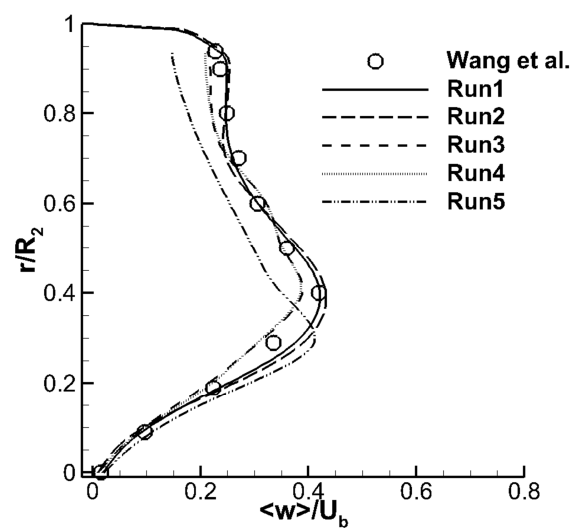


Figure 5.3 Grid sensitivity study : Time averaged mean swirl velocity at streamwise location $x/H=2.1$ ($Re=20,000$ $S=0.43$)

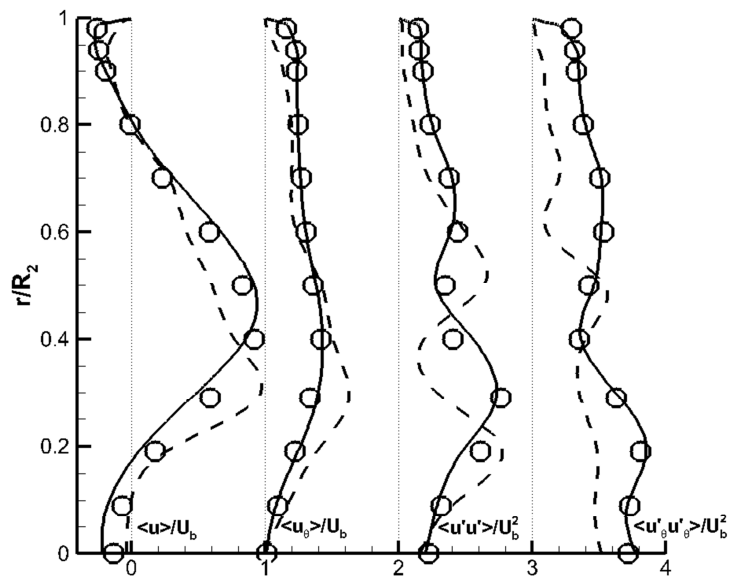


Figure 5.4 Effect of inlet turbulence : Time averaged profiles of axial velocity (scale 1:1), swirl velocity (scale 1:1), variance of axial velocity (scale 1:4), and variance of swirl velocity (scale 1:10) at representative axial location ($x/H=2.1$)

(Circles represent LDV data, solid lines represent LES predictions with SEM at inlet, and dashed lines represent LES predictions with laminar velocity profile at inlet)

($Re=20,000$ $S=0.43$)
104

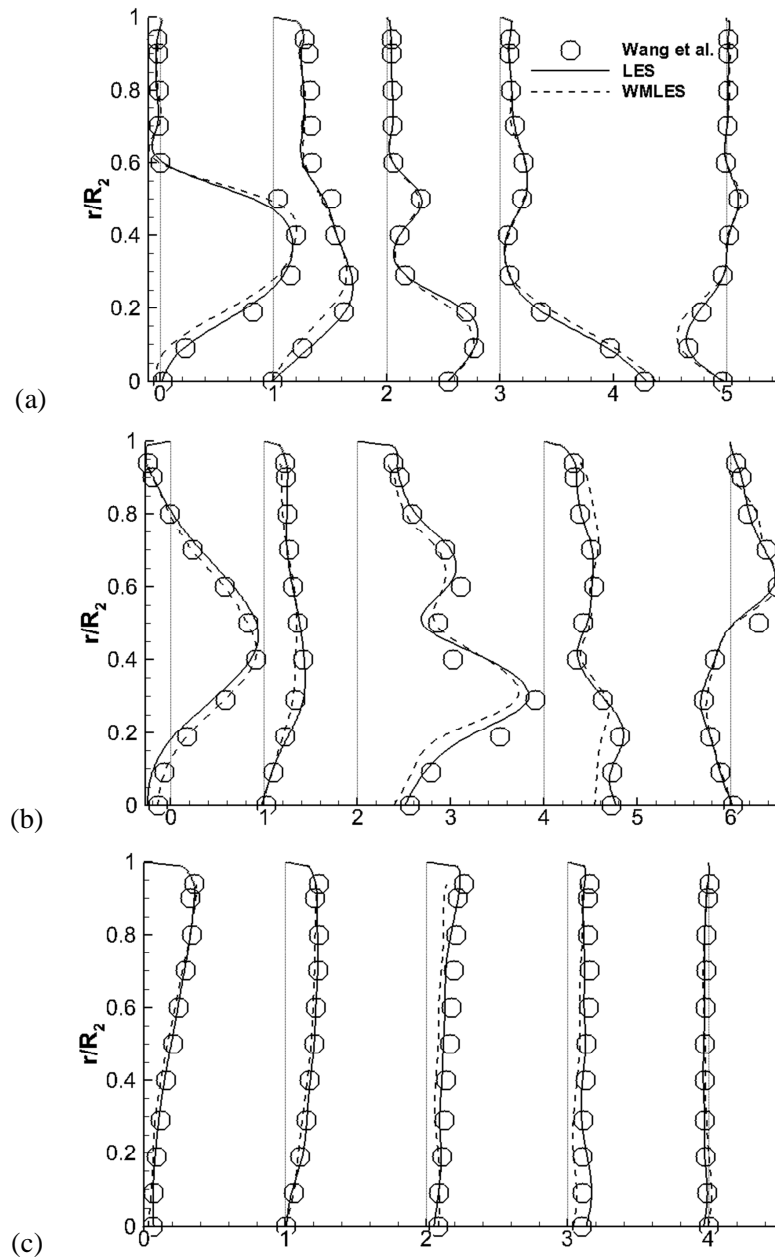


Figure 5.5 Time averaged profiles of (from left to right) axial velocity $\langle u \rangle / U_b$, swirl velocity $\langle u_\theta \rangle / U_b$, variance of axial velocity $\langle u'u' \rangle / U_b^2$, variance of swirl velocity

$\langle u'_\theta u'_\theta \rangle / U_b^2$, Reynolds shear stress $\langle u'_r u'_r \rangle / U_b^2$ for $Re=20,000$ and $S=0.43$ at (a) $x/H=0.17$,

(b) $x/H=2.1$, and (c) $x/H=6.3$

(Reynolds stresses are scales up by a factor of 10)

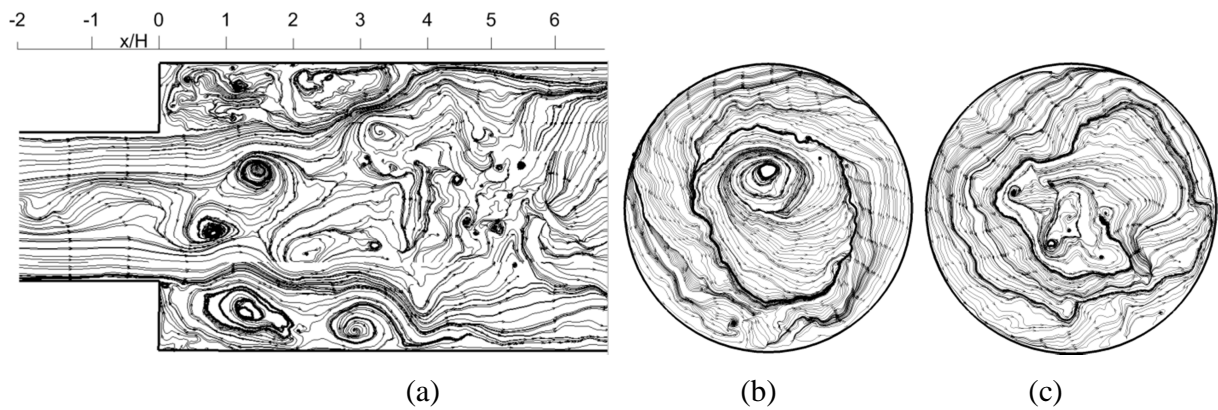


Figure 5.6 Instantaneous streamlines in (a) azimuthal plane ($z/H=0$), (b) $x/H=1$, and (c)

$x/H=5$

($Re=20,000$ $S=0.43$)

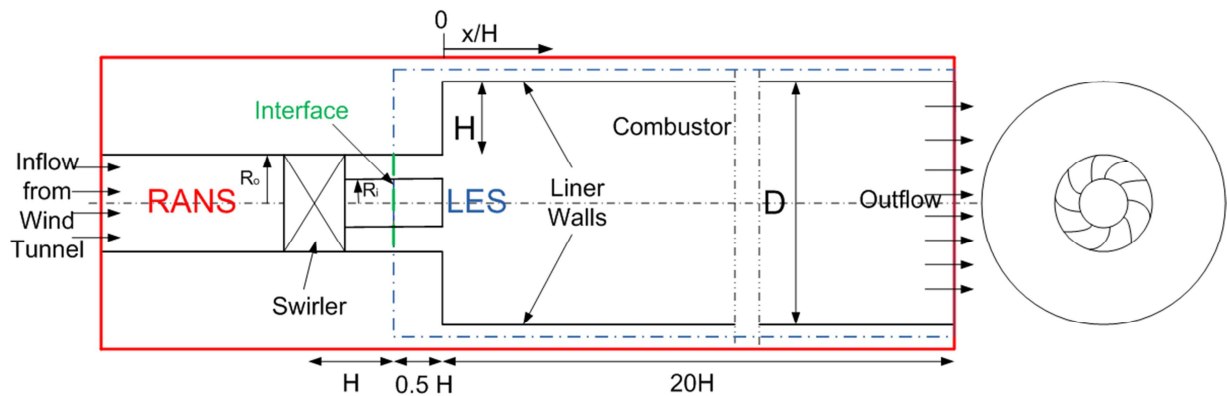


Figure 5.7 Schematics of experimental setup of Patil et al. [82]. From left to right: swirler, nozzle extension channel, can combustor

(RANS domain is shown in red. LES domain is shown in blue and the interface between RANS and LES is shown by green line. ($D=203$ mm, $H=0.3D$, $R_1=0.2D$) (Swirl nozzle: $R_i=0.11D$,

$$R_o=0.2))$$

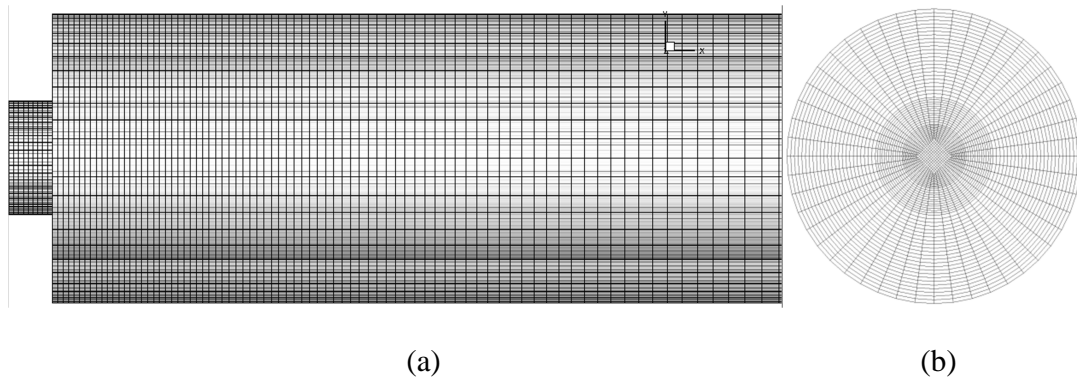


Figure 5.8 3D computational domain for LES of an industrial can combustor (a) frontal view, and (b) side view of the 3D mesh

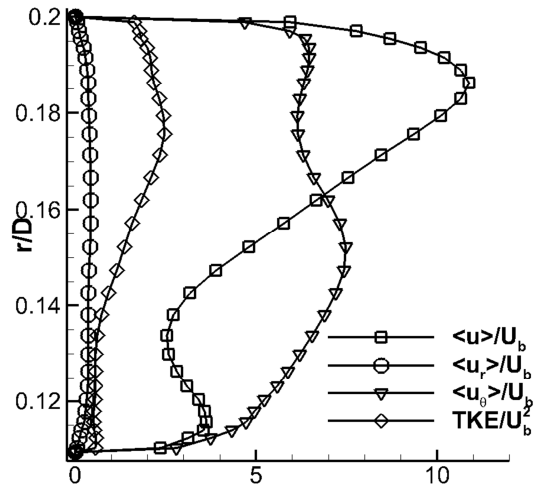
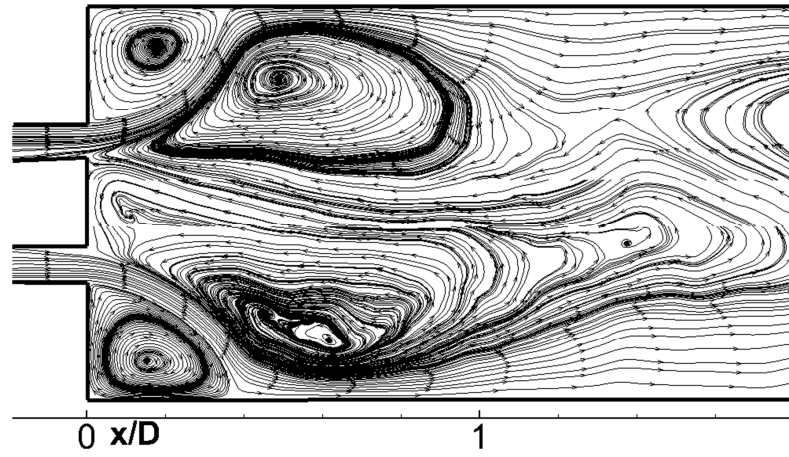
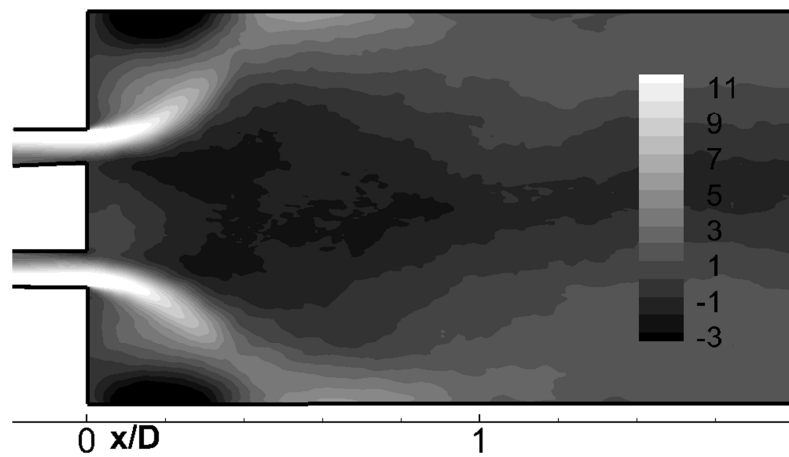


Figure 5.9 Profiles of mean velocity (normalized by bulk mean velocity in combustor) and turbulent kinetic energy (normalized by square of bulk mean velocity in combustor) at the inlet plane of the LES computational domain ($x/H=-0.5$)

($Re=50,000$, $S=0.7$)



(a)



(b)

Figure 5.10 (a) Mean flow streamlines in the azimuthal plane ($z=0$) (b) contours of axial velocity (normalized by bulk mean combustor velocity) in azimuthal plane ($z=0$)

($Re = 50,000$, $S = 0.7$)

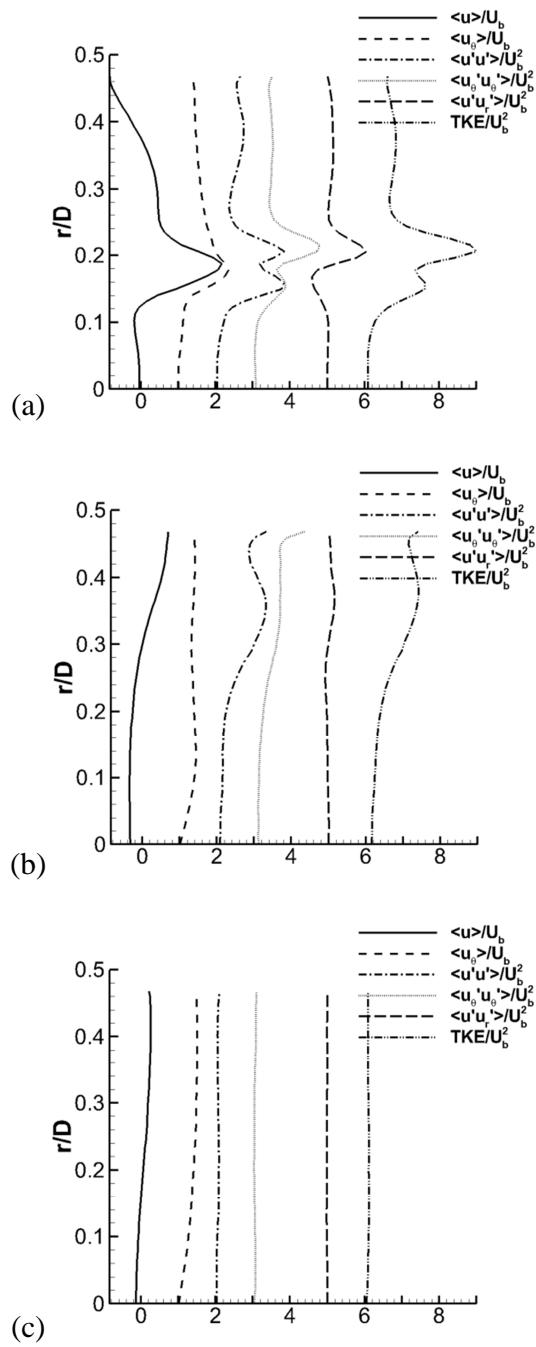


Figure 5.11 Variation of normalized mean velocity components and Reynolds stresses at
(a) $x/D=0.1$ (b) $x/D=0.45$ (c) $x/D=2$ (scale 6:1)

(Re = 50,000, S = 0.7)

(All quantities are circumferentially averaged and plotted along the radial direction. Mean velocities are normalized by the bulk mean combustor velocity while the Reynolds stresses are normalized by the square of the bulk mean combustor velocity. Values are plotted at stations located at x-axis value of 0,1,2,3,5, and 6.)

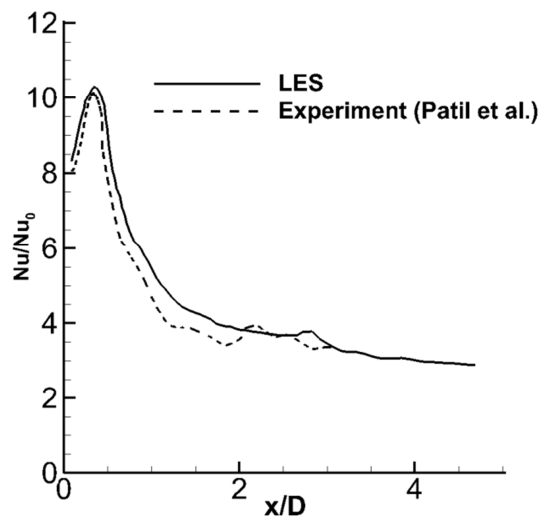
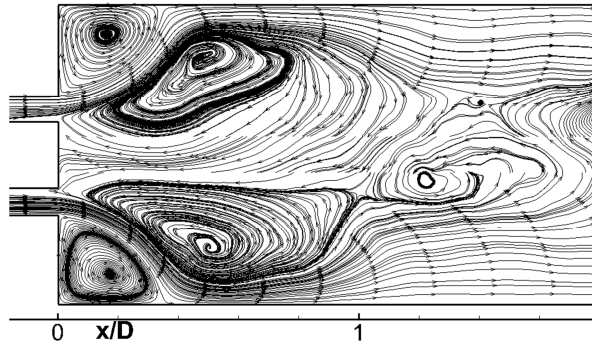


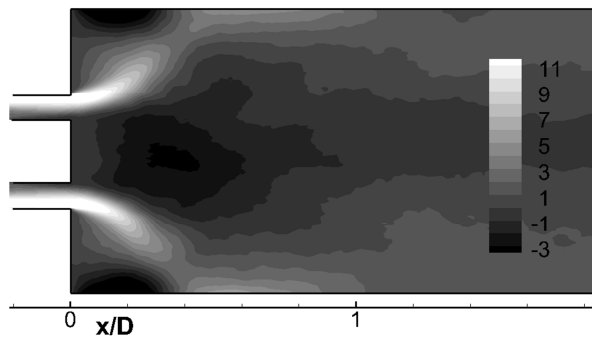
Figure 5.12 Heat transfer augmentation ratio (Nu/Nu_0) along the liner wall

(Re = 50,000, S=0.7)

($x/D = 0$ represent the start of the combustor at the step expansion. Base Nusselt number (Nu_0) is calculated using Dittus-Boelter correlation in Equation (5.5) for fully developed pipe flows)



(a)



(b)

Figure 5.13 (a) Mean flow streamlines in the azimuthal plane ($z=0$) (b) contours of axial velocity (normalized by bulk mean combustor velocity) in azimuthal plane ($z=0$)

($Re = 80,000, S = 0.7$)

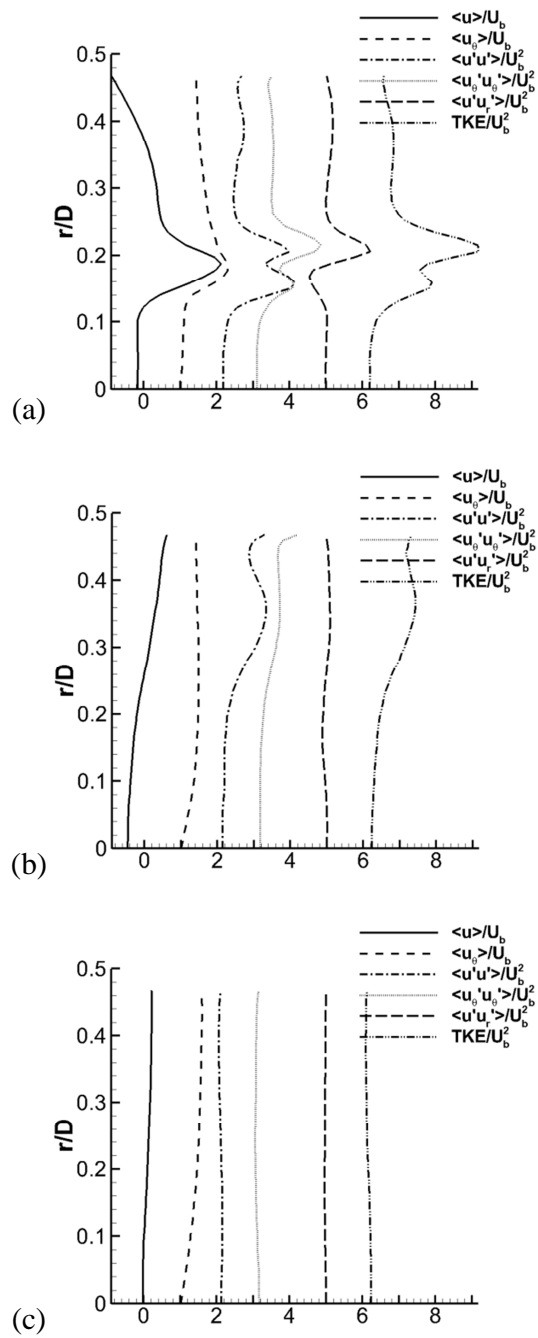


Figure 5.14 Variation of mean velocity components and Reynolds stresses at (a) $x/D=0.1$
 (b) $x/D=0.45$ (c) $x/D=2$ (scale 6:1)

(All quantities are circumferentially averaged and plotted along the radial direction. Mean velocities are normalized by the bulk mean combustor velocity while the Reynolds stresses are normalized by the square of the bulk mean combustor velocity. Values are plotted at stations located at x-axis value of 0,1,2,3,5, and 6.)

(Re = 80,000 S = 0.7)

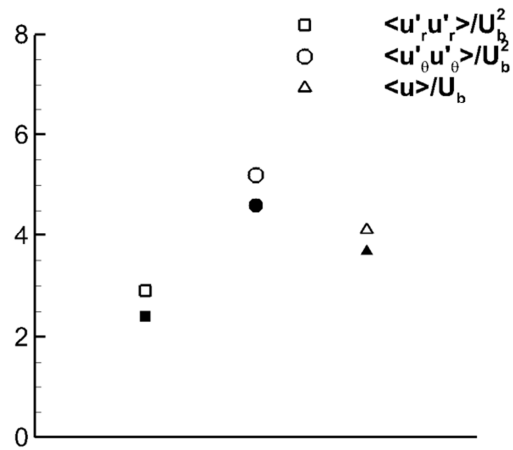


Figure 5.15 Normalized Reynolds normal stresses and axial velocity in the shear layer near the peak heat transfer location

(Empty symbols are for Re=50,000 and filled symbols are for Re=80,000. Axial location = (x/D=0.45). Radial location = (r/D=0.45))

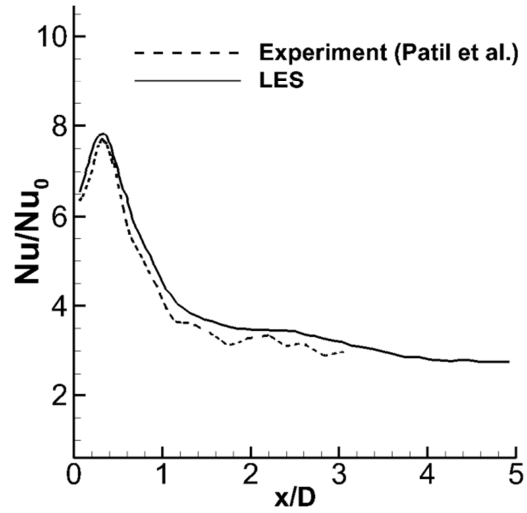


Figure 5.16 Heat transfer augmentation ratio (Nu/Nu_0) along the liner wall

($Re = 80,000$ $S = 0.7$)

($x/D = 0$ represent the start of the combustor at the step expansion. Base Nusselt number (Nu_0) is calculated using Dittus-Boelter correlation in Equation (5.5) for fully developed pipe flows)

Chapter 6

Large Eddy Simulation with Zonal near Wall Treatment of Rib Roughened

Ducts and Channels

This chapter presents wall modeled LES in a ribbed duct geometry used in internal cooling passages of gas turbine blades. Two different configurations are studied with rib height to hydraulic diameter of 0.1 and 0.05 and rib pitch to rib height ratio of 10 and 20 respectively. Reynolds numbers based on the hydraulic diameter of the duct and bulk mean velocity were 20,000 and 60,000 respectively for these two configurations. Predictions with the wall modeled LES calculations are compared with the available experimental data Rau et al. [99], and Han et al. [100], and wall resolved LES data of Tafti [101] for Reynolds number of 20,000. This is a first study where an integrated zonal velocity and temperature wall model is used to study a complex statistically three dimensional flow. It is shown that zonal wall model provides at least an order of magnitude savings in computational resources without any significant loss of accuracy.

The wall model is then extended to the simulation of rough surfaces. A computational methodology to account for the effects of roughness in the two-layer zonal model LES framework is presented. Simulations of rod roughened channels at high Reynolds numbers are performed with the roughness modified wall modeled LES. Good predictions of mean velocity and turbulent statistics compared with the experimental data of Bakken et al. [102] illustrates that the proposed modification in two layer model can account for roughness effects in high Reynolds

numbers flows. This is the first study which has integrated roughness modeling with a LES zonal wall model.

6.1 Internal Cooling Rib Ducts

6.1.1 Introduction

Ribbed internal cooling duct configurations are being used in modern powerful and fuel efficient gas turbines. Ribs or turbulators act as roughness elements enhancing the heat transfer coefficient and cooling capacity. Flow in these ribbed ducts involves many complex features like flow separation, curved shear layer, primary and secondary recirculation, reattachment of the boundary layer and recovery. Rotation of turbine blades introduces Coriolis forces while high thermal gradients introduce centrifugal buoyancy. In the past three decades, several experimental studies have been performed to characterize the heat transfer in rib roughened passages. Several researchers at Texas A&M (Han [103, 104], Chandra et al. [105], Lau et al. [106], Han and Zhang [107], Han et al. [108], Ekkad and Han [110]) have studied the effects of different rib angles, different sections, different rib orientations, full and discrete ribs, different rib height/hydraulic diameter ratios, different rib pitch/height ratios, different aspect ratio channels, and variable temperature and flux boundary condition in a Reynolds number range from 10,000 to 100,000. Taslim et al. [111], Korotky and Taslim [112], Taslim and Lengknong [113], Taslim and Korotky [114] have performed similar studies.

Many researchers have reported computational studies on the internal cooling channels. Many of these studies relied heavily on RANS approach for modeling turbulence. Saidi and

Sunden [115], Jia et al. [116], Iacovides et al. [117], Ooi et al. [118], and Prakash and Zerkle [119] have performed three dimensional RANS calculations on stationary duct while Jang et al. [120], Chen et al. [121], and Iacovides [122] carried out RANS studies on rotating ducts. Due to the anisotropic nature of the turbulent flow in these ribbed internal cooling passage, the investigated RANS model have had varying degree of success. The models based on eddy-viscosity [119] which assume flow isotropy do not perform well, while more complex models which solve for Reynolds stresses [116, 120, 123] have been found to perform reasonably well. RANS based models also suffer from lack of repeatability and low level of accuracy in predicting complex flow features in ribbed internal cooling ducts. Though computational expense has limited most of the studies to RANS approach, in recent years, a significant numbers of researchers have reported large-eddy simulations in internal cooling passages. Murata and Mochizuki [124] reported a LES calculation of a stationary duct for a low Reynolds number without any experimental validation. Excellent comparisons between LES calculations and experiments have been shown in fully developed stationary ducts by Tafti [101], in fully developed rotating ducts by Abdel-Wahab and Tafti [125], in fully developed stationary ducts with 45° ribs by Abdel-Wahab and Tafti [126], and in developing flow in stationary and rotating ducts by Sewall and Tafti [127]. Vishwanathan and Tafti [48] carried out DES of fully developed flow and heat transfer in internal cooling ribbed duct geometry.

Though many LES calculations have been reported in the literature, most of them are limited to either fully developed assumption or to a low Reynolds number, while most of the gas turbine applications have high operating Reynolds numbers. Also, most of the applications of

wall layer modeling in the LES framework have been applied to fluid flow problems without heat transfer. In the current study, the integrated zonal two layer model for velocity and temperature is used to represent the near wall flow and heat transfer on relatively coarse meshes. It is shown that this integrated zonal wall model results in at least order of magnitude savings in computational resources as well as time without any significant loss in accuracy as compared with wall resolved calculations.

6.1.2 Computational Domain

Figure 6.1 describes the computational domain for two different Reynolds number used for the current investigation. Geometries investigated for both the Reynolds number had a square cross section and ribs normal to flow direction. Ratio of rib height to the hydraulic diameter of the duct (e/D_h) was 0.1 and 0.05 while ratio of rib pitch to height was 10 and 20 for Reynolds number of 20,000 and 60,000 respectively. The computational methodology discussed in Chapter 3 assumes the flow and heat transfer to be fully developed for the current study. Hence the computational domain length in streamwise (x) direction is taken to be a periodic segment between the two adjacent ribs in actual experimental geometry of Rau et al. [99] and Han et al. [100]. All the walls of the duct including ribs were treated as no-slip boundaries with constant heat flux.

6.1.3 Grid resolution

Table 6.1 summarizes the calculations performed. Two different Reynolds numbers were investigated with wall modeled LES (WMLES) and LES without wall model. The Reynolds

number is based on the duct hydraulic diameter and the bulk mean velocity inside it. Grid sensitivity study is reported for Reynolds number of 20,000. All the grids were designed to perform the wall modeled LES calculations; but a calculation without wall model was performed on the same grid to evaluate the benefit of using the wall model in predicting the skin friction and surface heat transfer coefficient on a coarse mesh. LES calculations with zonal near wall treatment on grid 1 and 2 resulted in similar predictions without any significant difference. Further coarsening of grid 2 uniformly in all directions resulted in prediction of Nusselt number significantly different from experimental values.

Table 6.2 summarizes the results for Reynolds number of 20,000 for different grids. Grids for case 1 and 2 resulted in similar predictions. It's clear from Table 6.2 that the zonal two-layer formulation presented in Chapter 3 is able to predict the surface heat transfer coefficient in very close agreement with the experimental data and wall resolved LES calculations of Tafti [101] which utilized 128^3 grid. The predictions of the skin friction is also in close agreement with data and wall resolved calculation of Tafti [101] indicating that the zonal two-layer formulation presented in Chapter 3 works well in modeling the near wall region.

The benefit of using the wall model becomes evident in case 3 in which LES calculations with wall model are performed on a coarse mesh. It is clear that using a coarse mesh for LES calculations without wall model results in significant under prediction of skin friction. Also, the LES calculation without heat transfer wall model results in large under predictions of the surface heat transfer coefficient. This indicates that the use of constant heat flux (Neumann) boundary condition in the current study is inappropriate for coarser near wall mesh and results in

inaccurate wall temperature. The same argument can be made for constant wall temperature (Dirichlet) boundary condition, in which case the use of the wall temperature as boundary condition for outer LES may result in inaccurate near wall temperature profile which will further result in inaccurate calculation of surface heat transfer coefficient. In contrast, use of the heat transfer wall model helps in predicting the near wall temperature profile or wall heat flux accurately resulting in better prediction of surface heat transfer coefficient.

6.1.4 Computational Details

All the calculations for the bulk Reynolds number of 20,000 and 60,000 were performed at $Re_\tau = 6667$ (based on friction velocity) and 12355, respectively with a non-dimensional mean pressure gradient of unity applied in the flow direction. The non-dimensional time step in these calculations was set to 5×10^{-4} which is order of magnitude higher than the one used by Tafti [101] for his wall resolved calculation on the same geometry and Reynolds number. The viscous terms are treated implicitly. The average L_1 residual norm of global mass balance is converged to 1×10^{-8} , while the momentum and energy equations in the implicit treatment are converged to 1×10^{-7} . Calculations were initialized assuming an initial mass flow rate and integrated in time until the flow rate adjusts to the balance between internal losses and specified mean pressure gradient. After this point when the flow rate reaches an asymptotic value, data sampling was initiated to extract the mean flow and turbulent statistics. Total sampling interval was 10 non-dimensional time units. The local Nusselt number is calculated as

$$Nu = \frac{1}{\theta_s - \theta_{ref}}$$

where θ_s is the surface temperature and θ_{ref} is the reference temperature defined as

$$\theta_{ref} = \frac{\iint |u_1| \theta dA_x}{\iint |u_1| dA_x}$$

The surface-averaged Nusselt number is obtained by averaging the local Nusselt number as

$$\langle Nu \rangle = \frac{1}{\iint_{\Omega} ds} \left[\iint_{\Omega} \frac{1}{\theta_s - \theta_{ref}} ds \right]$$

where s denotes the surface under consideration. Based on the non-dimensional mean pressure gradient of unity, the Fanning friction factor is calculated as

$$f = \frac{1}{2u_b^2}$$

All calculations were performed on four Apple Xserve G5 compute nodes with 2.3 GHz PowerPC 970FX processor. For integrating over one non-dimensional time unit, about two hours of wall clock time is required for Case 1 in Table 6.1, while about one hour of wall clock time is required for Case 2 and Case 3. Inner layer calculations require less than 10% of the outer LES calculation time. Comparing the spatial resolution (128^3) for wall resolved LES of Tafti [101] and a time step of 5×10^{-5} , Case 1 reduces the computational complexity by a factor of 63, whereas Case 2 reduce the complexity of the computation by a factor of 140.

6.1.5 Ribbed Duct Flow at $Re_{DH}=20,000$

Figure 6.2 shows the mean streamline pattern at the center of the duct ($z = 0.5$) for case 1. All three cases for bulk Reynolds number of 20,000 showed the presence of the leading edge

vortex at the rib-wall junction , the counter-rotating vortex in the wake region of the rib and the recirculation region downstream of the rib. For case 1 and case 2 the reattachment length is found to be 4.1 rib heights downstream of the rib, which is in exact agreement with the wall resolved calculation of Tafti [101]. Rau et al. [99] also reported this value to be in the range of 4.0 to 4.2 rib heights. On the other hand, the reattachment length for case 3 of LES without wall model was over predicted to be around 4.7 rib heights.

Figure 6.3 represents the spanwise velocity distribution in the vicinity of side smooth wall for case 1. The flow predicted by the WMLES has three dimensional behavior near smooth wall with mean spanwise (w_b) velocity reaching up to 25% of the mean streamwise velocity ($\overline{u_b}$). The localized phenomenon of strong spanwise velocity moving toward and impinging on the smooth wall within the confines of the shear layer at the leading edge of the rib is a result of unsteady vorticity which is produced and transported at the junction of the rib with the smooth wall. This phenomenon is captured well with the WMLES calculation, whereas many RANS models fail to capture this secondary flow.

Figure 6.4 shows contours of time averaged Reynolds normal stresses (u_{rms} , v_{rms} , w_{rms}) and Reynolds shear stress ($\overline{u'v'}$) at the center plane of the duct ($z = 0.5$). Reynolds normal stresses are normalized by the bulk mean velocity while the Reynolds shear stresses are normalized by the square of the bulk mean velocity in the duct for comparisons with the experimental data. The time averaged variance of the streamwise velocity (u_{rms}) in Figure 6.4(a) has maximum values in the separated shear layer at the leading edge of the rib, with values between 40% and 50%. They are lowest in the stagnating flow at the rib and in the recirculation

immediately behind the rib as observed by Tafti [101]. Figure 6.4(e) represents the distribution of variance of streamwise velocity (u_{rms}) between the two ribs ($\frac{x'}{e} = 4.5$). This location is in the recovery region downstream of the reattachment point. The maximum values of u_{rms} in the shear layer behind the ribs and at the duct center ($y = 0.5$) were predicted to be around 38% and 15% respectively, which are in close agreement with the experimental values of 35% and 14% respectively in the shear layer and center, reported by Rau et al. [99].

The time averaged variance of transverse velocity (v_{rms}) at the center plane of the duct ($z = 0.5$) is plotted in Figure 6.4(b). The maximum value of v_{rms} in the separated shear layer downstream of the rib and at center of the duct ($y = 0.5$) are predicted to be 24% and 11%, respectively. These values compare in exact agreement with the experimental values of Rau et al. [99]. Figure 6.4(c) presents the time averaged variance of spanwise velocity (w_{rms}) at the center plane of the duct ($z = 0.5$). w_{rms} has a maximum value of about 38% at the top leading edge of the rib. High spanwise intensities are observed because of the impingement of eddies at the leading edge of the rib. This phenomenon is further explained in detail by Tafti [101]. The spanwise fluctuation are also high in the shear layer downstream of the rib with a maximum value of about 30% as shown in Figure 6.4(e).

Figure 6.4(d) shows the distribution of the time averaged Reynolds shear stress ($\overline{u'v'}$) in the center plane of the duct ($z = 0.5$). Distribution of $\overline{-u'v'}$ is shown in Figure 6.4(e) in the wall normal direction. The Reynolds shear stress reaches a maximum value of about -5% in the separated shear layer downstream of the rib. Rib shear layer dominance can be observed in

Figure 6.4(e). Similar to cross-stream fluctuations, the Reynolds shear stress distribution does not show a near wall maximum feature of typical boundary layer flow.

Figure 6.5 shows the distribution of the time averaged turbulent kinetic energy (tke) at the center of the duct. The augmentation in tke because of the ribs compared with the plane channel flows is predicted well in WMLES calculations. Also, the maximum value (14%) of tke in the shear layer is predicted well as compared to the LES of Tafti [101].

Figure 6.6 shows the Nusselt augmentation distribution for the WMLES calculation. The augmentation ratio is calculated in terms of the Dittus-Boelter correlation. Heat transfer is maximum on the front of the wall as a result of the highly unsteady energetic secondary eddies formed in that region. These eddies result in enhanced mixing which further results in an increase in the surface heat transfer coefficient. As inferred by the distribution of the turbulence intensities plotted in Figure 6.4, the momentum in the flow downstream of the recirculation region of the rib reduces significantly, resulting in lower heat transfer augmentation values. Further downstream, the heat transfer augmentation increases and reaches a maximum value near the reattachment point. The augmentation decreases as the smooth wall is approached with values close to unity at the corners. On the smooth wall, higher heat transfer augmentation occurs in the vicinity of the rib junction. This is a result of lateral flow impingement on the wall as shown in Figure 6.3. Maximum heat transfer occurs on the leading edge of the ribs with values as high as 5.2. This can be attributed to strong flow acceleration in this region.

Figure 6.7 compares the predicted heat transfer augmentation by WMLES calculations with the experimental data of Rau et al. [99] at the center of the ribbed wall ($z = 0.5$) and at a

location $0.5e$ upstream of the rib along the smooth wall. The predictions match in close agreement with the data. Both the trends and the values of heat transfer augmentation predicted by WMLES agrees with the experimental data. The experimental traverse stops at $y = 0.4$ and does not go to the center. The surface averaged values are tabulated in Table 6.2 for the ribbed and smooth walls. WMLES calculations predict the heat transfer augmentation within the experimental uncertainty. The trends in the prediction accuracy of the Nusselt number are consistent with observation of Tafti [101]. The same consistent trends are observed in friction coefficient, which is predicted to within 10% of the experimental data. On the other hand, the LES calculation without wall model on a coarse mesh under predicts both the friction coefficient and Nusselt augmentation significantly. This is consistent with the observation made with the validation case. It is clear that the LES without zonal near wall treatment fails to predict the wall temperature correctly which further results in inaccurate prediction of the Nusselt number augmentation. Under prediction of friction factor using LES on a coarse mesh is also reported in previous studies [128].

6.1.6 Ribbed Duct Flow at $Re_{DH}=60,000$

A grid of $88 \times 88 \times 88$ was used in the computational domain with Y^+ values in the range of 20-40. Predictions with WMLES calculations are compared with the limited experimental data of Han et al. [100]. Experimental data for flow measurement is not provided but the overall friction factor is reported. Measured distribution of Nusselt number on the ribbed wall along the centerline ($z = 0.5$) and on smooth wall is reported.

Figure 6.8 represents the mean streamline structure at the center plane ($z = 0.5$) of the duct. The major flow structures are similar to that for $Re=20,000$. The reattachment length is found to be about three times the rib height. Figure 6.9 and Figure 6.10 represent the turbulent intensities and the mean turbulent kinetic energy variation along the duct height. Comparing the values with $Re=20,000$ case, it can be observed that the values of these turbulence quantities are significantly lower. This indicates that the configuration of $Re=60,000$ case with lower values of ratio of rib height to the hydraulic diameter of the duct and higher ratio of pitch to height results in producing less amount of turbulence compared with $Re=20,000$ case.

Figure 6.11 compares the predictions of Nusselt augmentation ratio at the center line of duct ($z = 0.5$) on the ribbed wall with measured values from Han et al. [100]. WMLES captures the trends in the heat transfer augmentation as well as the values of Nusselt augmentation in close agreement with the experimental data of Han et al. [100]. Distribution of Nusselt augmentation on the smooth wall, rib, and ribbed wall is shown in Figure 6.12. The trends in the surface heat transfer coefficient distribution on the ribbed and smooth walls are similar to the one observed for $Re=20,000$ case. The maximum value of the Nusselt augmentation occurs at the leading edge of the rib facing the flow. Highly energetic unsteady eddies upstream of the rib are responsible for the flow acceleration and hence higher magnitudes of the heat transfer augmentation. In the region immediately downstream of the rib, the flow is weak resulting in very low values of the heat transfer augmentation approaching a value of unity. The Nusselt augmentation value slowly recovers and peaks near the flow reattachment length after which it drops slightly leading up to the next rib. It is also important to note that the values of the Nusselt

augmentation are significantly lower compared to the $Re=20,000$ case. This can be attributed to the lower turbulent intensities observed in Figure 6.10 and discussed previously. The lower production of turbulence results in less mixing and hence results in significantly lower values of surface heat transfer coefficient on the duct walls.

Han et al. [100] also reported values of heat transfer augmentation distribution on the centerline ($y= 0.5$) on the smooth wall along the length of the duct. They reported these values in the range of 1.35 to 1.45. Predictions from the WMLES calculation also agree with this observation with values in the range 1.4 to 1.55. The average value of the Nusselt augmentation on smooth walls predicted by WMLES is 1.5 which is slightly higher than the value of 1.4 reported by Han et al. [100]. The average value of Nusselt augmentation on the ribbed wall was predicted to be 2.15 by WMLES. This value is slightly overpredicted compared to the reported value of 2.0 by Han et al. [100]. The overall friction factor augmentation is predicted to be 4.1 by the WMLES calculations, which matches in exact agreement with the value reported by Han et al. [100]. The base friction factor (f_{FD}) was calculated using

$$f_{FD} = 0.079 \times Re^{-0.25}$$

It is important to mention that the LES calculation without any wall model on the same grid for $Re=60,000$ results in significantly different predictions than experiments and hence are not reported for brevity. The under prediction of the friction factor was significant resulting in major differences with experimental observation of flow patterns and Nusselt augmentation.

6.2 Two Layer Wall Model for Large Eddy Simulations of Flow over Rough surfaces

The following section investigates various approaches for modeling the effects of roughness, followed by a methodology proposed to modify the two layer wall model presented in Chapter 3 to account for wall roughness. Predictions with roughness modified wall modeled LES at high Reynolds number in a rod roughened channel are presented at the end.

6.2.1 Background and Introduction

Many practical industrial flows involve flow over rough walls. Roughness influences the mean velocity profile in the inner layer near the wall by shifting it in comparison to the smooth wall. This shift can be characterized by a roughness function which depends on the roughness frontal area, height, and the nature of the roughness. Similar to smooth wall flows, the total mean shearing stress with roughness is constant near the wall as convective terms are small in the mean momentum equation. Hence the mean flow sufficiently distant from the roughness elements can be represented as

$$U^+ = \frac{1}{\kappa} \ln(y^+) + B - \Delta U^+ \quad (6.1)$$

where U is the mean streamwise velocity, y is the distance from the surface, and constants B and κ continue to hold the value for the logarithmic law of the wall for smooth surfaces. The superscript $+$ represents normalization by shear velocity $u_\tau = \sqrt{\tau_w/\rho}$, where τ_w is the wall shear stress and ρ is the density. ΔU^+ is the roughness function representing a shift in the mean velocity and can be correlated to the roughness length scale k , which represents the roughness geometry. A convenient and more popular alternative to k is the use of an equivalent sand grain

roughness, which is a modified length scale producing the same roughness function ΔU^+ as if the surface was covered by sieved sand. The relationship between the roughness function and equivalent sand grain roughness reads as,

$$\Delta U^+ = \frac{1}{\kappa} \ln(k_s^+) + B - C \quad (6.2)$$

where C is a constant which reflects the wall boundary condition and hence depends on the roughness geometry (its value is found to be 8.5 for sand-grain roughness) and k and k_s are related using Equation (6.3) [129].

$$\frac{k_s}{k} = \frac{\exp[\kappa(\Delta U^+ - B + C)]}{k^+} \quad (6.3)$$

Roughness effects on the outer layer can be modeled by changing the effective position of the wall and hence artificially increasing the shear stress near the wall. Rotta [130] demonstrated that the roughness effects can be achieved by increasing the Prandtl mixing length near the wall. The shift in mean velocity described by the roughness function can be obtained by modifying the mixing length as

$$l^+ = \kappa(y^+ + \Delta y^+) \{1 - \exp[-(y^+ + \Delta y^+)/A^+]\} \quad (6.4)$$

where Δy is the required shift in the wall location and can be directly related to the roughness length scale. The rightmost term in Equation (6.4) is the van Driest damping function in which $A^+ = 26$. Rotta [130] provided a generic expression which can correlate this shift in the wall location with the roughness geometry details. Cebeci and Chang [131] proposed the following generic expression, correlating the shift in wall location to roughness Reynolds number in terms of equivalent sand grain roughness.

$$\Delta y = 0.9 \left(\frac{\nu}{u_\tau} \right) \left[\sqrt{k_s^+} - k_s^+ \exp \left(-\frac{k_s^+}{6} \right) \right] \quad (6.5)$$

Equation (6.5) is valid in a wide range ($4.5 < k_s^+ < 2000$) of sand grain roughness covering hydraulically smooth surfaces, transitional, and fully rough regimes. The correlations which link the shift in wall position (Δy) to equivalent sand grain roughness also need to have a relationship between the roughness geometry and the equivalent sand grain roughness. Schlichting [132] has experimentally determined the values for equivalent sand grain roughness for a large number of roughnesses arranged in a regular fashion. Dvorak [133] has established a correlation between the velocity shift and roughness density for two dimensional rectangular rough elements from which the equivalent sand grain roughness can be determined. Simpson [134] proposed a more generalized form of the Betterman and Dvorak correlation for roughness density effects on the turbulent boundary layer. For the roughness elements other than those investigated by Schlichting [132] and Dvorak [133], the equivalent sand grain roughness needs to be determined from experimental or empirical methods.

Other mixing length models [135] have been proposed where the effects of roughness are modeled by reducing the van Driest damping as k^+ increases. All these models are based on the fact that flows with the same effective k^+ , and hence the same shift in velocity profile, should have similar mixing properties. This fact is based on the Townsend's [136] hypothesis stating that the turbulent flow in the region outside the roughness sub layer is independent of the wall roughness at sufficiently high Reynolds numbers. Several different experiments [137-140] performed on different kinds of rough geometries support this hypothesis. Hence Townsend's hypothesis can be used to successfully model the effects of roughness in a simplistic way.

Another way to account for the effect of roughness is known as the discrete element method in which form drag term is added to the governing momentum equations to account for blockage effect of the roughness elements on flow near the wall. Christoph and Pletcher [141] added a sink term in the momentum equation for the form drag and employed a mixing-length model including the roughness effect. Taylor et al. [142] modified both mass conservation and momentum equation to account for blockage effects of the roughness and added a form drag term to the momentum equation and employed a smooth wall van Driest mixing length model. Gilkson and Aupoix [143] proposed similar modifications for RANS based $k - \varepsilon$ and $k - \omega$ models. These discrete element models attempt to connect roughness geometry to roughness effects rather than depending on a single roughness length scale, though, these models are developed for only regular array of elements like cones and spheres. Also, these models are not applicable to sand grain or similar random roughness.

There have been very few studies reported with LES or DNS of rough wall flows at high Reynolds numbers. As the mesh size needs to be much smaller than the roughness height k , LES of such flows needs very dense grids and has been limited to comparatively low Reynolds numbers. Leonardi et al. [144] performed the DNS and LES of a turbulent channel flow with transverse square bars on one wall at a Reynolds number of 6900. They used both, Van Driest damping, and the dynamic subgrid model, and obtained good agreement between the two simulations for pressure and skin friction on the wall. Cui et al. [145] investigated turbulent channel flow with transverse rib roughness on one wall using LES. They varied the spacing of the roughness elements to reproduce d-type and k-type roughness defined by Perry et al. [146].

Their LES results were in good agreement with laboratory data and provide more insights into the effect of roughness on the mean flow as well as turbulent structures. Juneja and Brasseur [147] characterized subgrid-resolved-scale dynamics for atmospheric boundary layers. Cui et al. [148] proposed a force field model to simulate turbulent flow over a surface with arbitrary roughness. They decomposed roughness into a resolved and subgrid-scale roughness similar to the flow decomposition in LES.

Wall modeled LES of turbulent flows over rough surfaces has not been used in engineering applications while some work has been done in working with atmospheric boundary layers. Thomas and Williams [149] developed a synthetic rough wall boundary condition based on the Schumann [36] wall model. They treated the instantaneous stress as a linear combination of the mean and fluctuating components, where the fluctuating part responds less to the roughness and consequently contributes less to the local shear stress compared with the original Schumann [36] wall model. Moeng [150] reported a wall boundary condition by specifying the SGS vertical fluxes at the wall. This condition took in to account more fluctuations compared to the Schumann model. Mason and Gallen's [151] rough wall model also manages to take into account more fluctuations. Xie et al. [152] proposed a family of wall models which exhibit better performance than its predecessor models for LES. At present, no LES wall model exists which possesses the capability to simulate different kinds of complex engineering flows on rough walls at high Reynolds number.

Here a new roughness modified two-layer LES wall model for modeling the near wall region in flow over rough surfaces is proposed. Equivalent sand grain roughness is used to

correlate the amplification in wall shear stress with the roughness geometry. Calculations are performed in a rod roughened channel geometry of Bakken et al. [102] at high Reynolds number in the range of 6000 to 56000 in the fully rough regime. The roughness wall model predicts the skin friction coefficient accurately and predicts the mean velocity profile and turbulent statistics in good agreement with the experiments.

6.2.2 Roughness Modification to Two Layer Wall Model

The two layer wall model presented in Chapter 3 is modified to account for surface roughness effects. Roughness effects on the outer layer are modeled by changing the effective position of the wall and hence artificially increasing the shear stress near the wall. The turbulent viscosity, $(1/Re_t)$ in Equation (3.20) is modeled based on Rotta's [130] approach of changing the effective position of the wall as follows

$$1/Re_t = \kappa/Re(d^+ + \Delta d^+)\{1 - \exp[-(d^+ + \Delta d^+)/A^+]\}^2 \quad (6.6)$$

where, κ is von-Karman constant, d is normal distance from the wall, $A^+ = 26$ and,

$$d^+ = \frac{u_\tau d}{\nu} \quad (6.7)$$

$$u_\tau = \sqrt{\frac{\tau_w}{\rho}} \quad (6.8)$$

$$\tau_w = \left(\frac{1}{Re} + \frac{1}{Re_t} \right) \frac{d(u_t)}{dn} \Big|_{\text{wall}} \quad (6.9)$$

For sufficiently high Reynolds number in the fully rough regime, the wall displacement Δd can be related to equivalent sand grain roughness (k_s) as [130]

$$\Delta d = 0.035k_s \quad (6.10)$$

If the roughness Reynolds number doesn't fall in the fully rough regime, Cebeci and Chang's [131] expression presented in Equation (6.5) is used.

6.2.3 Computational Details

All simulations are performed in the fully developed region of the experimental geometry of Bakken et al. [102] which is shown in Figure 6.13. As shown in Figure 6.13, both the top and bottom walls of the channel are covered by square rods extending in the spanwise direction. Ratio of roughness height (k) to channel half width (h) is 0.034 and ratio of roughness height to roughness pitch (center to center rod spacing, λ) is 0.125. Bakken et al. [102] calculated the equivalent sand grain roughness using Equation (6.3) with the experimentally calculated value of the roughness function through comparison of mean velocity distribution with the logarithmic law of the wall for smooth flows. The ratio of equivalent sand grain roughness to roughness element height was experimentally found to be about 7.8 for Reynolds numbers (based on shear velocity and half channel width) of 600 to 6000.

The computational domain is chosen to be $2\pi h \times 2h \times \pi h$ in streamwise, wall normal, and spanwise direction respectively, where h is half width of the rod roughened channel. Periodic flow conditions are used in streamwise (x) and spanwise (z) direction. Table 6.3 summarizes the calculations performed. The calculations are performed in the bulk flow Reynolds number range of 6000 to 56000 with roughness falling in the fully rough regime. The grid was taken to be uniform in streamwise and spanwise direction. Table 6.3 represents the grid spacing in wall co-ordinates. The first grid point in the wall normal direction was taken at least

two roughness heights away from the wall. (The y^+ value in Table 6.3 represents the distance of the first grid node from the wall in wall coordinates).

6.2.4 Mean Flow Velocity Prediction

Mean velocity predictions are compared with experimental measurements in Figure 6.14 to Figure 6.17 for Reynolds number range of $Re_\tau=600$ to 6000. For all Reynolds numbers the predictions of mean velocity profile is in close agreement with the experiments except for $Re_\tau=6000$ for which the prediction error is slightly higher. The rough-wall profiles also show the downward shift in mean velocity (ΔU^+) as seen in Figure 6.14. This shift is observed to follow the logarithmic dependency with roughness height in wall co-ordinates with change in Reynolds number. This behavior is consistent with k-type roughness behavior. Variation of skin friction coefficient is shown in Figure 6.18. These values are a very weak function of Reynolds number, indicative of a fully rough regime. In comparison, Dean's empirical correlation [153] is plotted for smooth walls, the value of which decreases with Reynolds number. The predicted values match the experimental measurements in close agreement.

6.2.5 Reynolds Stress Prediction

Bakken et al. [102] experimentally observed some important differences in Reynolds stress distribution between rough and smooth wall flows. The peak value of streamwise Reynolds normal stress for rough wall flows was found to be attenuated (up to 50%) and to move away from the wall compared with the smooth wall flow. The peak position shifted outward approximately by the corresponding value of k^+ . In rough wall flows, there is dominance of

pressure forces near the wall in contrast to strong viscous forces for smooth wall flows, which are expected to be negligible in the fully rough regime [154]. Bakken et al. [102] also observed that the integral length scale in the streamwise direction to be shorter than for smooth wall flows indicating the break-up of the near wall streamwise vortices over the rough wall. This seems to be the main mechanism responsible for the significant attenuation of streamwise Reynolds normal stress for rough walls. Bakken et al. [102] also observed that the Reynolds normal stresses in the spanwise and wall normal direction also get attenuated but this attenuation is not significant compared with Reynolds normal stress in the streamwise direction. They also reported that shear stress measurement above the rough surface reaches a reduced peak level compared to smooth wall flow.

The predicted Reynolds normal stresses and Reynolds shear stress are plotted in Figure 6.19 through 6.21 for Reynolds number (based on shear velocity) $Re_\tau=600$ to 6000. All the Reynolds stresses are predicted with reasonable accuracy considering the large savings in computational cost afforded by this procedure as compared to a wall resolved LES in which the roughness elements would have to be resolved. The streamwise Reynolds normal stress ($\overline{u'^2}$) is significantly overpredicted at the lowest Reynolds number, $Re_\tau=600$, in contrast to the experiments which indicate a larger attenuation over a smooth wall distribution. A DNS of a similar geometry at this Reynolds number [129] also showed this discrepancy. DNS predictions were also not able to capture the large attenuation shown by experiments.

Predictions slightly underpredict the value of transverse near wall Reynolds normal stress for all Reynolds numbers. Still, the levels of ($\overline{v'^2}$) in the outer layer tend to follow the Reynolds

number rather than the boundary condition for both the experiments and predictions. This indicates that the flow over smooth as well as rough walls have similar transport mechanisms for wall normal Reynolds normal stresses.

The experiments involved significant (>10%) uncertainty in spanwise Reynolds normal stress ($\overline{w'^2}$), measurements, which are not available for all Reynolds numbers. Predictions show similar trends and are within the experimental uncertainty for Reynolds numbers where the measurement data is available. Reynolds shear stress is predicted in close agreement with experiments for all Reynolds numbers. The peak values in Reynolds shear stress are found to be slightly lower than smooth wall flows for the same Reynolds numbers.

6.3 Conclusions

WMLES calculations are conducted in a ribbed duct at $Re=20,000$ and $60,000$ for two different rib geometries. The calculations predict the friction factor and Nusselt number augmentation in close agreement with the experimental data for both Reynolds numbers investigated. The major flow features corresponding to the unsteady energetic eddy near the rib wall, the recirculation zone behind the rib and corner eddy, reattachment location are predicted in close agreement with the experimental observations and wall resolved LES predictions. Trends in the surface heat transfer coefficient distribution as well as values of Nusselt augmentation were predicted well within the experimental uncertainty for both the Reynolds numbers. It was also observed that these LES calculations without any wall model under predict the friction factor and Nusselt augmentation significantly.

The advantage of using the wall model both for flow and heat transfer becomes prominent at higher Reynolds number. It is noteworthy to mention that the time step used in the current calculations is an order of magnitude higher than the time step required for a wall resolved LES. This, in conjunction with the coarser grid, results in significant savings in overall computational cost. These savings are critical especially for developing flow calculations which involve several ribs in serpentine channels.

The two-layer wall model is extended to simulate flow over rough surfaces. The approximate boundary condition provided by the wall model in terms of shear stress is modified by shifting the position of the wall to account for roughness. Shift in the wall position is linked to the roughness geometry through the equivalent sand grain roughness. Calculations are performed

in a rod roughened channel geometry at high flow Reynolds number in the range of 6000 to 56000 in the fully rough regime. The roughness wall model predicts the skin friction coefficient accurately and predicts the mean velocity profile and turbulent statistics in good agreement with the experiments. The proposed roughness modified two-layer wall model can be applied to any complex flow geometry with rough walls and can provide a cost effective way for numerical investigation at practical Reynolds numbers.

6.4 Tables

Table 6.1 Ribbed duct calculation summary

| Case | Re_τ | Re_b | grid resolution | Y^+ | near wall treatment |
|------|-----------|--------|-----------------|-------|---------------------|
| 1 | 6667 | 20000 | 72×72×64 | 15-30 | Zonal |
| 2 | 6667 | 20000 | 56×56×48 | 20-30 | Zonal |
| 3 | 6667 | 22200 | 56×56×48 | 20-30 | No-slip |
| 4 | 12533 | 60000 | 88×88×88 | 20-40 | Zonal |

Table 6.2 Heat transfer and friction data comparison with Rau et al. [99] (Re=20,000)

| LES calculations, $\frac{e}{D_h} = 0.1, \frac{p}{e} = 10$ | | | | Experimental | |
|--|-------------|-------------|------------|--------------|-----------------|
| | case1 | case 2 | case 3 | Tafti [101] | Rau et al. [99] |
| Re_τ | 6667 | 6667 | 6667 | 6667 | - |
| Re_b | 20,000 | 20,000 | 22,200 | 20,000 | 30,000 |
| % form loss | 90 | 90 | 95 | 91 | 85 |
| Reattachment length (x_r/e) | 4.2 | 4.2 | 4.5 | 4.1 | 4.0-4.25 |
| $\langle Nu \rangle / Nu_0$ ($Nu_0 = 0.023 \cdot Re_b^{0.8} \cdot Pr^{0.4}$) | | | | | |
| Rib | 2.49 | 2.46 | 1.96 | 2.89 | - |
| Ribbed Wall | 2.20(7.9%) | 2.21 (7.9%) | 1.82 (24%) | 2.4 | 2.40 |
| Smooth Wall | 1.91 (6 %) | 1.92 (6%) | 1.48 (28%) | 1.89 | 2.05 |
| Overall with rib | 2.13 | 2.14 | 1.76 | 2.23 | - |
| Overall w/o rib | 2.05 (6.8%) | 2.06 (6.9%) | 1.69 (23%) | 2.14 | 2.21 |
| f/f_0 ($f_0 = 0.046 \cdot Re_b^{-0.2}$) | | | | | |
| Overall | 8.5 (10%) | 8.5 (10%) | 7.25 (24%) | 8.6 | 9.5 |

Experimental uncertainty is $\pm 5\%$

Table 6.3 Calculation and grid resolution summary for flow in rod roughened channel

| Re_τ | Re_b | Δ_x^+ | y^+ | Δ_z^+ | C_f | $C_{f,expt}$ | k_s |
|-----------|--------|--------------|-------|--------------|--------|--------------|--------|
| 600 | 5927 | 117 | 60 | 60 | 0.0205 | 0.02 | 0.2241 |
| 1200 | 11494 | 157 | 120 | 80 | 0.0212 | 0.0218 | 0.2689 |
| 3200 | 30650 | 314 | 300 | 160 | 0.0218 | 0.02276 | 0.2689 |
| 6000 | 57869 | 600 | 600 | 320 | 0.0215 | 0.02296 | 0.2689 |

6.5 Figures

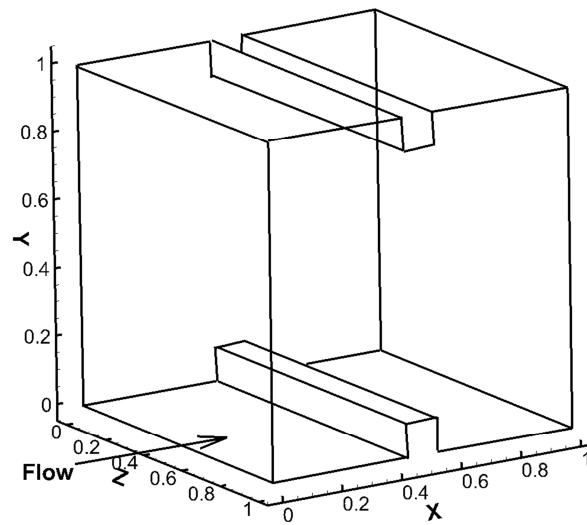


Figure 6.1 Computational domain for ribbed duct

(Re=20,000)

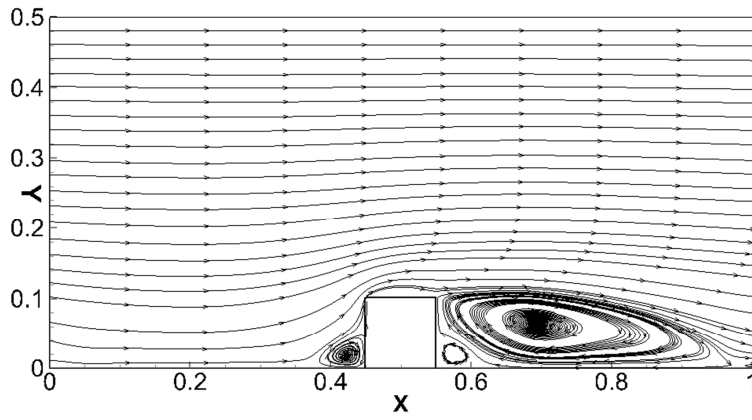


Figure 6.2 Mean flow streamline distribution in the z-symmetry ($z=0.5$) plane

($Re=20,000$)

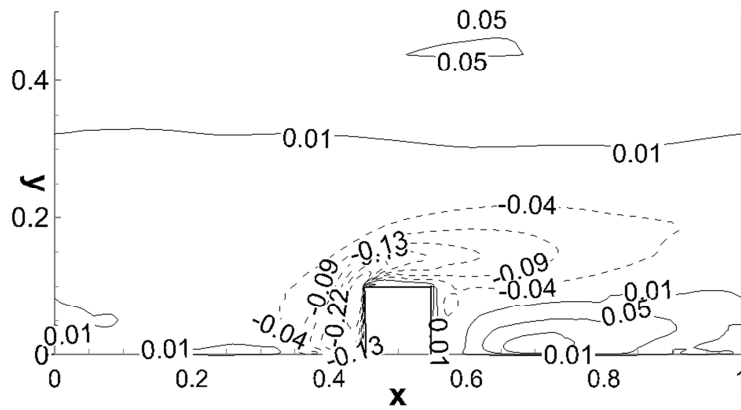
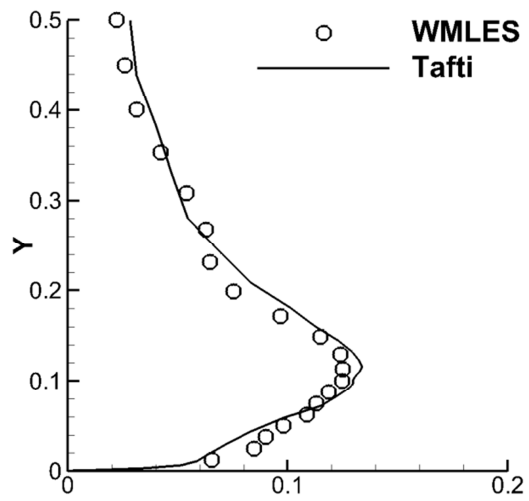


Figure 6.3 Contours of mean spanwise flow velocity near smooth wall ($z=0.05$)

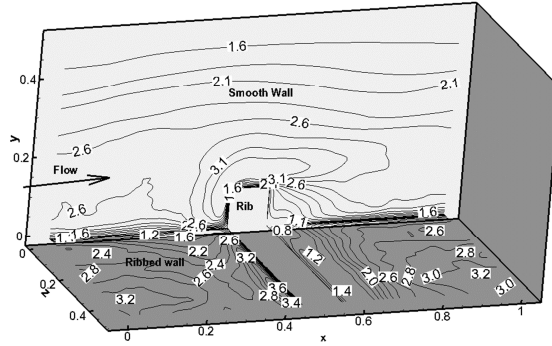
($Re=20,000$)



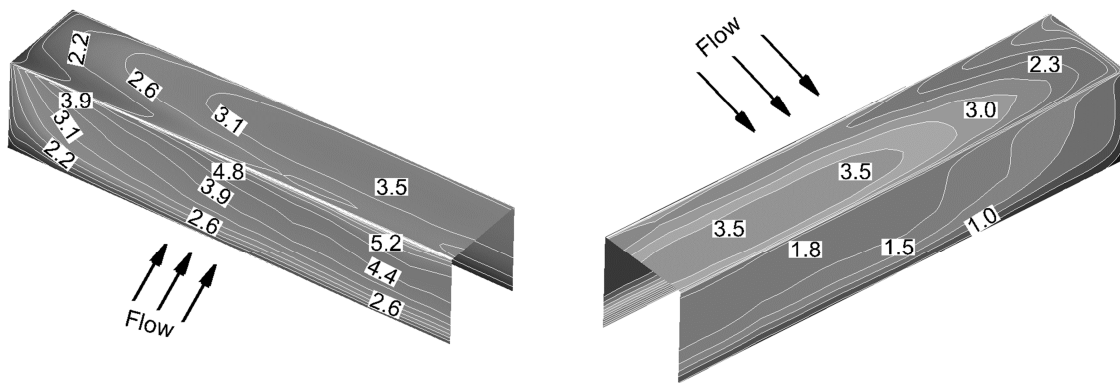
(b)

Figure 6.5 Turbulent kinetic energy at center plane ($z = 0.5, x'/e=4.5$)

(Re=20,000)



(a)

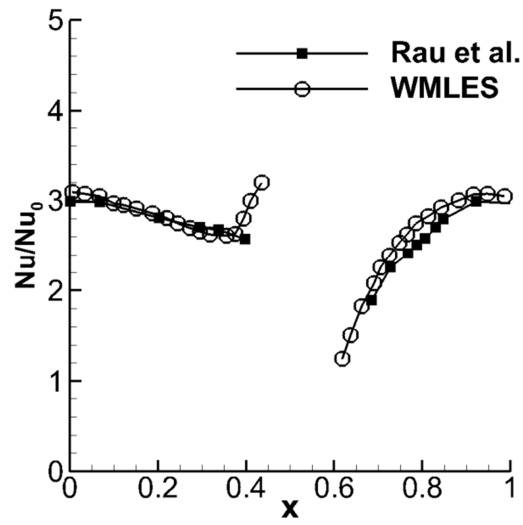


(b)

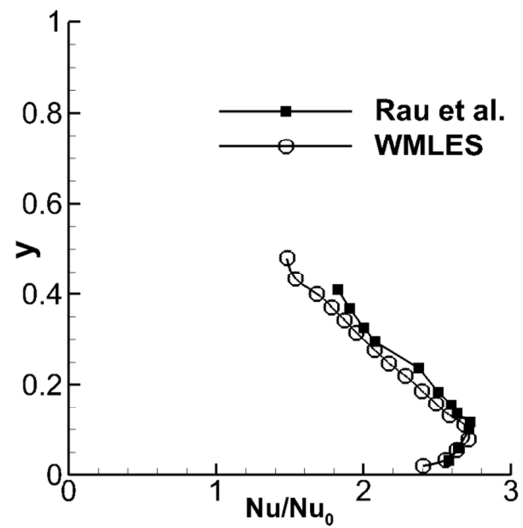
Figure 6.6 Contours of Nusselt augmentation on (a) smooth wall, and ribbed wall, and (b)

ribs

(Re=20,000)



(a)



(b)

Figure 6.7 Comparison of Nusselt augmentation with experimental data of Rau et al. [99]

on (a) ribbed wall at center plane, $y=0$, $z=0.5$ (b) smooth wall at $e/2$ upstream of the rib,

$z=0$, $x=0.4$

($Re=20,000$)

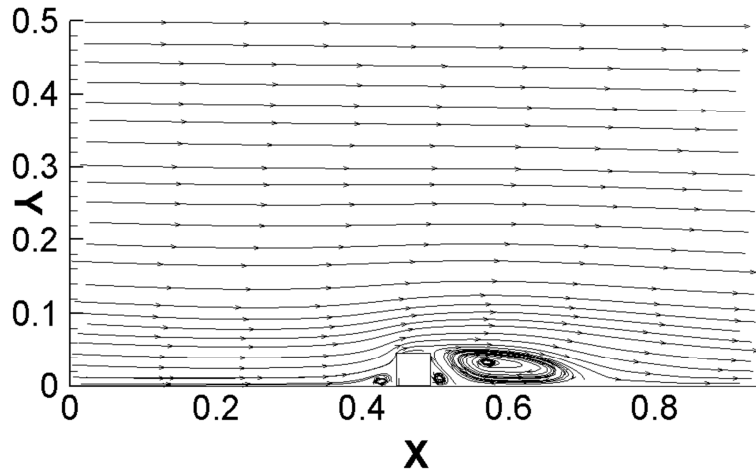


Figure 6.8 Mean flow streamline distribution in the z-symmetry plane ($z=0.5$)

($Re=60,000$)

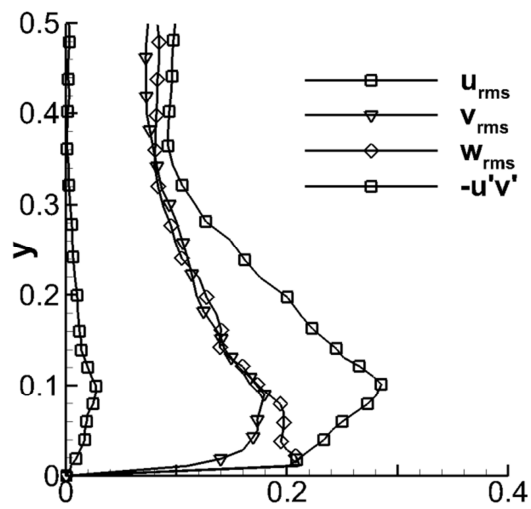


Figure 6.9 Reynolds stresses at center plane of the duct ($z = 0.5, x'/e = 8.5$)

($Re=60,000$)

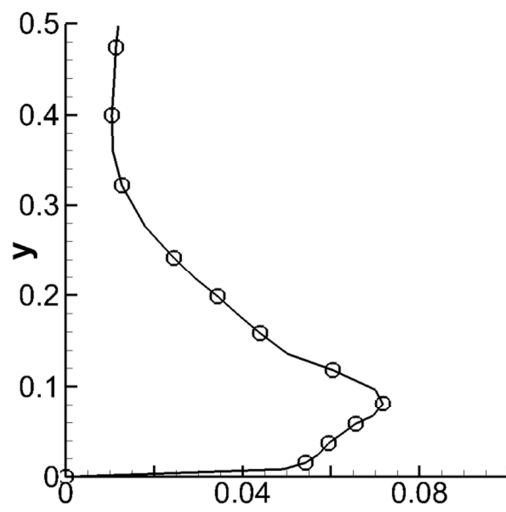


Figure 6.10 Turbulent kinetic energy at center plane of the duct ($z = 0.5, x'/e=8.5$)

(Re=60,000)

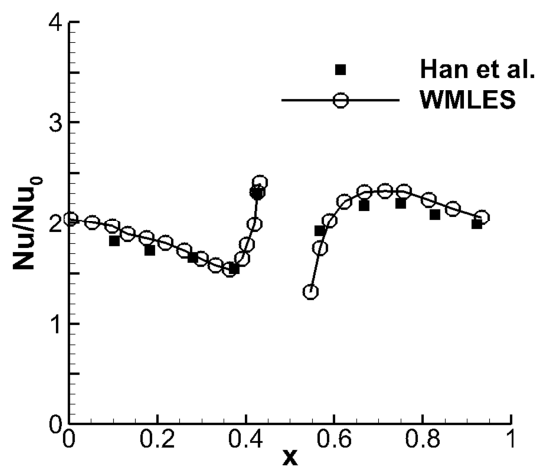


Figure 6.11 Comparison of Nusselt augmentation with experimental data of Han et al.

[100] at center plane of the duct ($z=0.5, y=0$)

(Re=60,000)

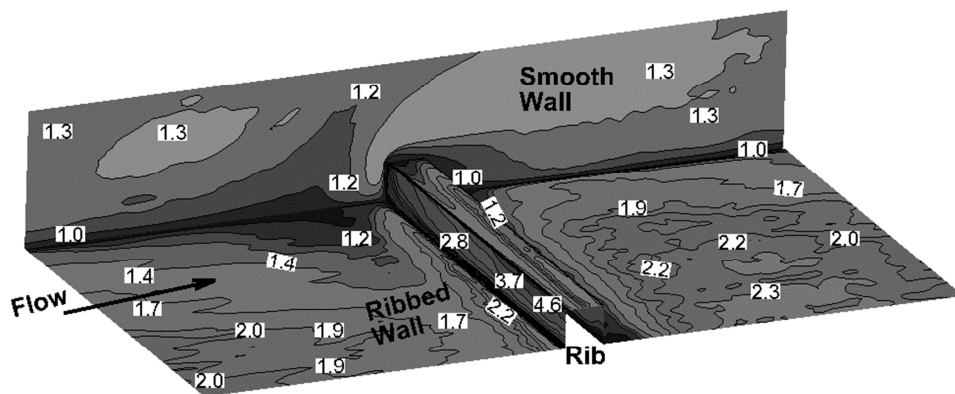


Figure 6.12 Contours of Nusselt augmentation on smooth wall, rib, and ribbed wall

(Ribbed bottom wall is shown from smooth wall till z symmetry plane)

($Re=60,000$)

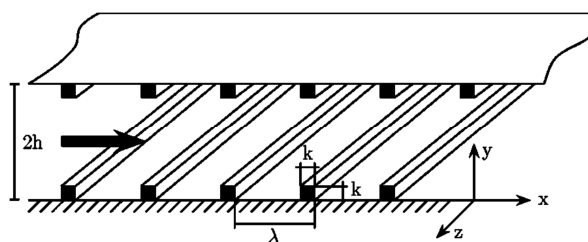


Figure 6.13 Experimental rod roughened geometry of Bakken et al. [102]

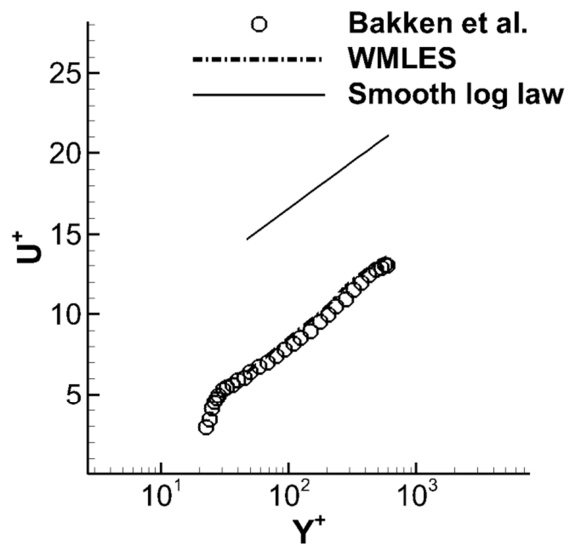


Figure 6.14 Comparison of predicted mean flow velocity from WMLES with experimental data of Bakken et al. [102] and smooth log law ($Re_{\tau}=600$)

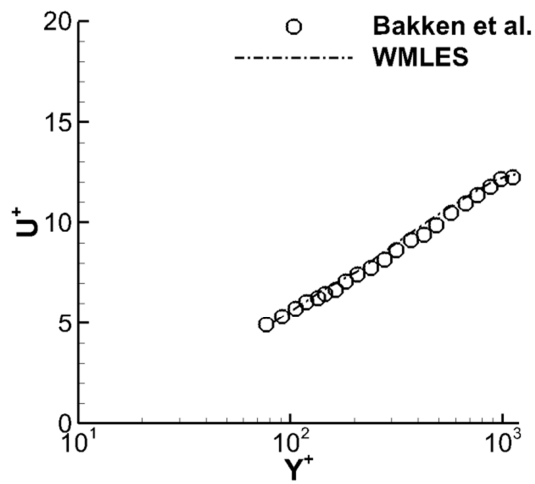


Figure 6.15 Comparison of predicted mean flow velocity from WMLES with experimental data of Bakken et al. [102] ($Re_{\tau}=1200$)

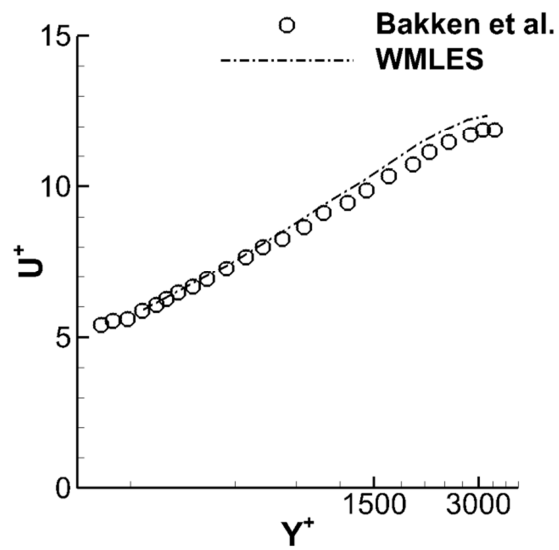


Figure 6.16 Comparison of predicted mean flow velocity from WMLES with experimental data of Bakken et al. [102] ($Re_\tau=3200$)

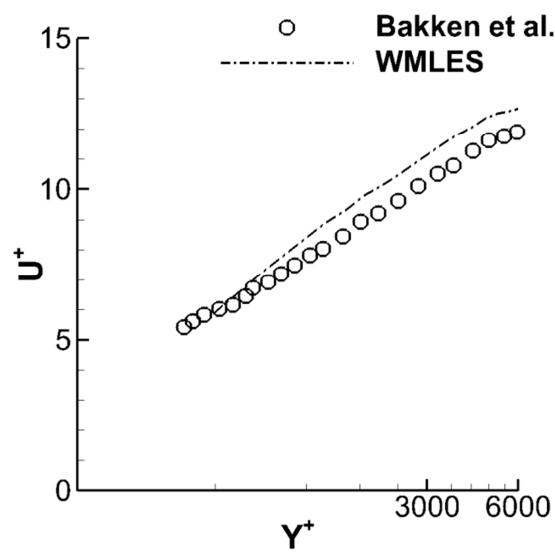


Figure 6.17 Comparison of predicted mean flow velocity from WMLES with experimental data of Bakken et al. [4] ($Re_\tau=6000$)

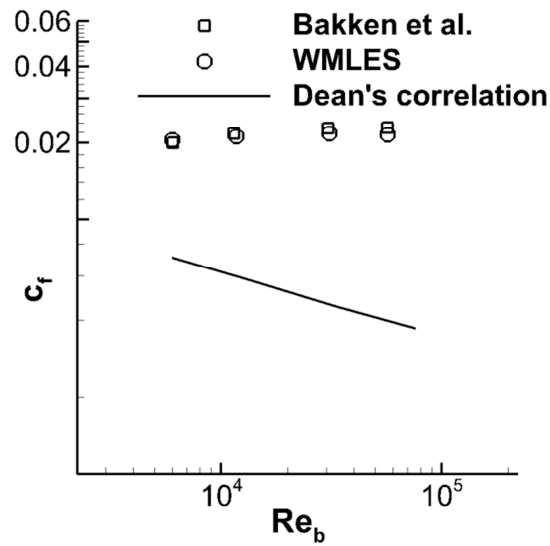


Figure 6.18 Skin friction coefficient variation with Reynolds number

(Circles represent WMLES predictions, squares – experimental data of Bakken et al [102], and straight line represent Dean's correlation for smooth channels)

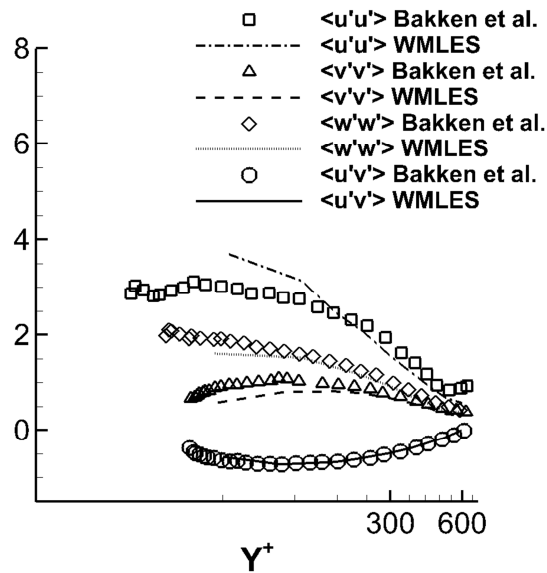


Figure 6.19 Reynolds normal stress and shear stress distribution ($Re_\tau=600$)

(All variables are normalized by square of shear velocity u_τ)

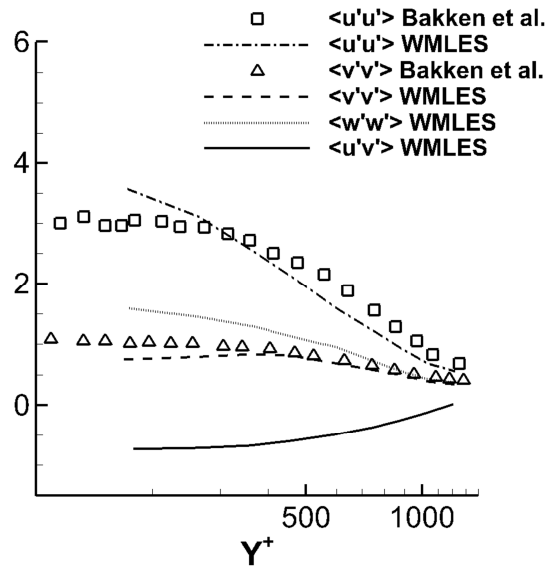


Figure 6.20 Reynolds normal stress and shear stress distribution ($Re_\tau=1200$)

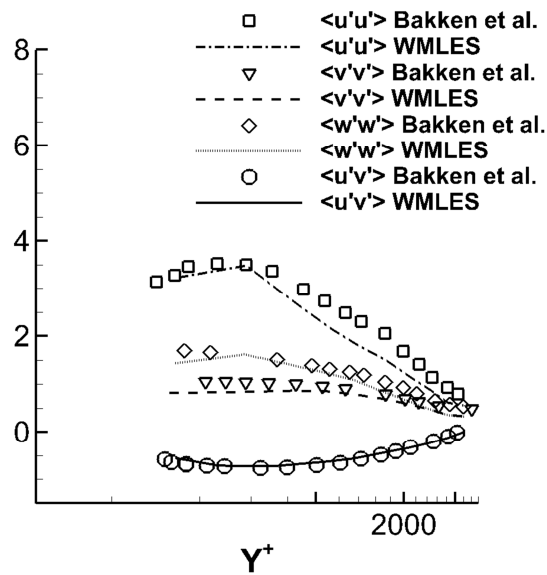


Figure 6.21 Reynolds normal stress and shear stress distribution ($Re_\tau=3200$)

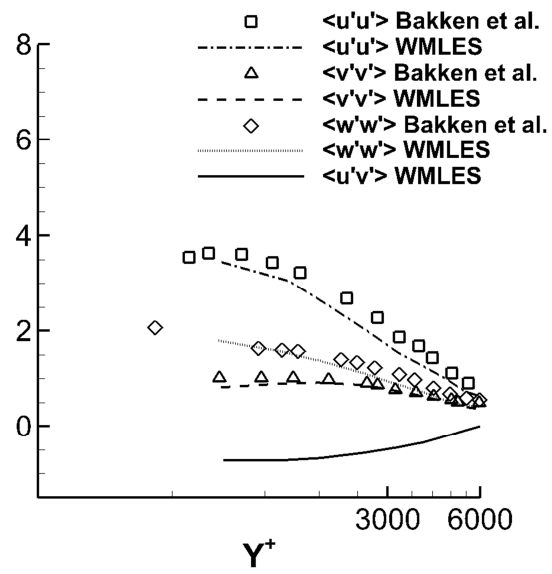


Figure 6.22 Reynolds normal stress and shear stress distribution ($Re_\tau=6000$)

Chapter 7

Summary and Conclusions

The research presented in this thesis was motivated by the desire to use LES in complex high Reynolds number flows. There were two major challenges identified in performing large eddy simulations of these complex flows. First, the very high near wall mesh resolution required at high Reynolds numbers, and second, the need for an accurate and computationally simple method to generate inlet turbulent boundary conditions for developing flows. These challenges led to the development of the wall modeling and inlet turbulence generation capability in the in-house LES code GenIDLEST.

Large eddy simulations of complex high Reynolds number flows are carried out with the near wall region modeled with a zonal two layer model in this dissertation. A novel formulation for solving the turbulent boundary layer equation for the effective tangential velocity in a generalized co-ordinate system is presented and applied in the near wall zonal treatment. This formulation reduces the computational time in the inner layer significantly compared to the conventional two layer formulations present in the literature and is most suitable for complex geometries involving body fitted structured and unstructured meshes.

The synthetic eddy method, which is a stochastic procedure based on the classical view of turbulence as a superposition of coherent structures is implemented to generate the turbulence at the inlet plane of the computational domain of developing flow problems. This method is designed to develop instantaneous velocity signals based on experimental, reduced RANS, or any precursor simulation input data.

The zonal two layer wall model and the synthetic eddy method are validated individually in turbulent channel flows and together in flow over a backward facing step at very high Reynolds numbers. The effectiveness of combining these two techniques is systematically shown in an experimental swirl combustor and an industrial scale gas turbine can combustor in the Reynolds number range of 20,000 to 80,000 with corresponding Swirl number in the range of 0.43 to 0.7. The synthetic eddy method reduces the computational complexity and provides accurate inlet turbulent specification, while the zonal wall model represents the near wall region accurately on a relatively coarse mesh in the complex swirling flows. Furthermore, the synthetic eddy method was used in a hybrid RANS-LES simulation in a dry low emission can combustor by using the upstream flow conditions from RANS to generate inlet turbulence for the embedded LES domain in the region of interest.

The integrated zonal near wall approach for velocity and temperature is then successfully used to investigate complex three dimensional flow and heat transfer in a ribbed duct passage for internal turbine blade cooling. The zonal wall model is further modified to take in to account the effects of surface roughness. The roughness modified two layer wall model was able to predict the mean flow and turbulent quantities in a rod roughened channel in good agreement with experimental data at high Reynolds numbers.

The wall model approach results in significant savings in computational resources by virtue of the coarser grids that can be used in wall bounded flows. This also enables the use of larger time steps, both of which together lead to at least an order of magnitude savings in computational cost. The synthetic eddy method provides a cost effective and robust approach to

accurately specify inlet turbulence data for complex flows and helps in reducing the size of the computational domain by limiting it to the immediate domain of interest. This thesis establishes that the synthetic eddy method and wall modeled LES provide a powerful avenue for investigating complex engineering flows at high Reynolds numbers.

Appendix A

Nomenclature

| | |
|---------------|---|
| \bar{a}^i | Contravariant basis vector |
| C_p | Specific heat |
| D_h | Hydraulic diameter |
| e | Rib height |
| f | Fanning friction factor |
| g^{ij} | Contravariant metric tensor |
| \sqrt{g} | Jacobian of the transformation |
| $\sqrt{g}U^j$ | Contravariant flux vector |
| k | Thermal conductivity |
| L_x | Domain length in streamwise (x) direction |
| \vec{n} | Surface normal vector |
| Nu | Nusselt number |
| P | Rib pitch or total pressure |
| p | Fluctuating pressure |
| Pr | Prandtl number |
| q'' | Heat flux |
| Q_x | Flow rate in x direction |
| Re | Reynolds number |

| | |
|-------------|---|
| Re_b | Reynolds number based on bulk velocity($= \frac{\bar{u}_b D_h}{\nu}$) |
| Re_τ | Reynolds number based on shear velocity($= \frac{u_\tau D_h}{\nu}$) |
| Re_t | Inverse of turbulent viscosity |
| S | Swirl number |
| T | Temperature |
| \vec{u} | Cartesian velocity vector |
| x' | Distance from downstream of the rib |
| \bar{x} | Physical space coordinate |
| $\bar{\xi}$ | Computational space coordinate |
| ν | Kinematic viscosity |
| ρ | Density |
| τ | Shear stress |
| β | Mean pressure gradient |
| γ | Mean temperature gradient |
| θ | Fluctuating, modified or homogenized temperature |
| Ω | Total heat transfer surface area |

Subscripts

| | |
|-----|----------------------------------|
| S | Surface |
| b | Bulk mean time averaged velocity |
| 0 | Smooth duct or channel |

rms Root mean square

Appendix B

Large Eddy Simulation of in Fully Developed Turbulent Channel Flow with Heat Transfer at $Re_\tau=590$

In this section, a wall resolved LES is carried out in a fully developed turbulent channel flow at $Re_\tau=590$ (Reynolds number based on shear velocity and channel half width). A grid resolution of $196 \times 196 \times 196$ is used in the computational domain spanning in $2\pi\delta \times 2\delta \times \pi\delta$ in streamwise (x), wall normal (y), and spanwise (z) directions respectively, where δ is half channel width. The grid spacing in streamwise and spanwise direction is taken to be uniform resulting in $\Delta x^+ = 19$ and $\Delta z^+ = 9.5$. (superscript + denotes wall coordinates, i.e. normalization by shear velocity u_τ). Y^+ of the first off wall grid point was taken to be 0.8 and then grid was stretched in wall normal direction resulting in total 196 grid points. Dynamics Smagorinski model is used to model the effects of eddies smaller than the grid size. Periodic boundary conditions were applied in streamwise and spanwise directions, while channel walls were treated as no-slip boundaries with constant heat flux.

Flow predictions with the LES are compared with the reference DNS of Kim et al. [76]. Figure B.1 shows comparison of time averaged mean streamwise velocity with the DNS [76]. It is observed that the mean velocity is predicted in exact agreement with DNS. Figure B.2 represents that the predicted Reynolds normal stresses and Reynolds shear stresses are in very good agreement with DNS. The maximum error in Reynolds stress prediction is 7% compared with the DNS.

The Nusselt number predicted from the LES calculation comes out to be 106.0. This values matches in close agreement with the value of 105.6 from Dittus-Boelter correlation for

fully developed pipe flows. With this detailed flow and heat transfer validation, the temperature profile predicted from wall resolved LES simulation is used for validation of heat transfer wall model in Chapter 4.

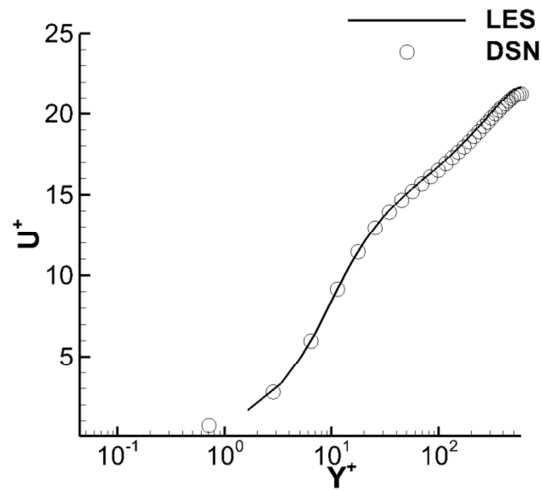


Figure B.1 Comparison of predicted mean velocity with DNS [76]

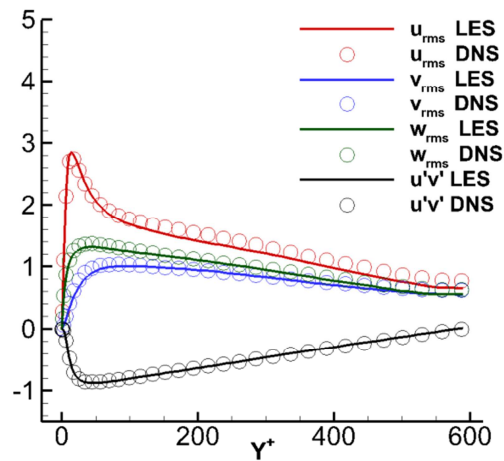


Figure B.2 Comparison of predicted Reynolds stresses with DNS [76]

Appendix C

Large Eddy Simulations of Confined Weakly Swirling flows with Synthetic Inlet Turbulence

This section presents the results from wall resolved as well as wall modeled LES on confined weakly swirling flows at Reynolds number of 10,000 and characteristic Swirl number of 0.33. Computational details are given in Chapter 5 including the geometry, computational domain, grid resolution, and boundary conditions. Numerical procedure described for $Re=20,000$ and $S=0.43$ described in Chapter 5 is followed for performing LES simulations in this section. Figure C.1 compares input experimental mean flow and turbulent stresses and reproduced profiles of these quantities from LES with SEM used at the inlet plane of the computational domain.

C.1 Flow predictions

Time averaged mean velocity profiles at various streamwise locations in the computational domain are plotted in Figure C.2. LES calculations were able to predict the higher swirl velocity near the axis as well as steep gradients in the swirl velocity in the shear layer as observed in experiments accurately. It is important to note that the LES calculation with the wall model is able to reproduce near wall velocities in all regions of the combustor immediately after expansion as well as further downstream of it in good agreement with the experiments.

Wall resolved as well as wall modeled LES calculations were able to predict the variances of all three velocity components at all twelve stations in good agreement with the LDV data. It is important to note that each variance has significantly different values than the other

two indicating strong anisotropies in the flow-field. Figure C.2 represents that the LES calculations are able to simulate anisotropic turbulence in the flow-field accurately. Also, they predict the turbulent kinetic energy distribution in the shear layer as well as near the axis of the combustor accurately. Higher magnitude of variances of streamwise and circumferential velocity at the beginning of combustor section, which is one of the characteristics of the swirling flows are captured well by the computations. Reynolds shear stresses are also predicted accurately with LES. Both LES calculations were able to predict the turbulence production in the shear layer as well in core region where the vortex breakdown process occurs. Predictions were able to capture the trends especially the peaks in the Reynolds stress profile in fairly good agreement with the data.

Figure C.3 represents instantaneous streamlines from wall modeled LES calculation. These streamlines shows the typical characteristics of weak to moderate swirl flows. The streamlines exhibit curvature in the inflow section as against to straight flow in non-swirling flow. A vortex breakdown can be observed in the region of $2.5 < x/H < 3.3$ in Figure C.3.a where streamlines show flow reversal. An internal recirculation zone is created as a result of this breakdown process. This internal recirculation zone is not axisymmetric and has bubble shape. The streamlines shown in the Figure C.3.b and C.3.c represent some more important features of swirling flows. Figure C.3.b represents highly swirling flow in the upstream region of the combustor at a streamwise section at $x/H=1$. The streamlines at this section represent a large swirling flow structure. As it can be noticed from this figure that the center of this swirling flow is off the combustor axis. This further results in nonzero swirl and radial velocity components in

this region. The oscillatory motion of the coherent structures near the combustor axis represents the presence of the precessing vortex core. The swirl strength reduces in the downstream region of the combustor section. Figure C.3.c represent decayed swirl flow region at a streamwise location $x/H=5$ downstream of the sudden expansion. The streamline structure at this section also shows the presence of the several smaller coherent structures.

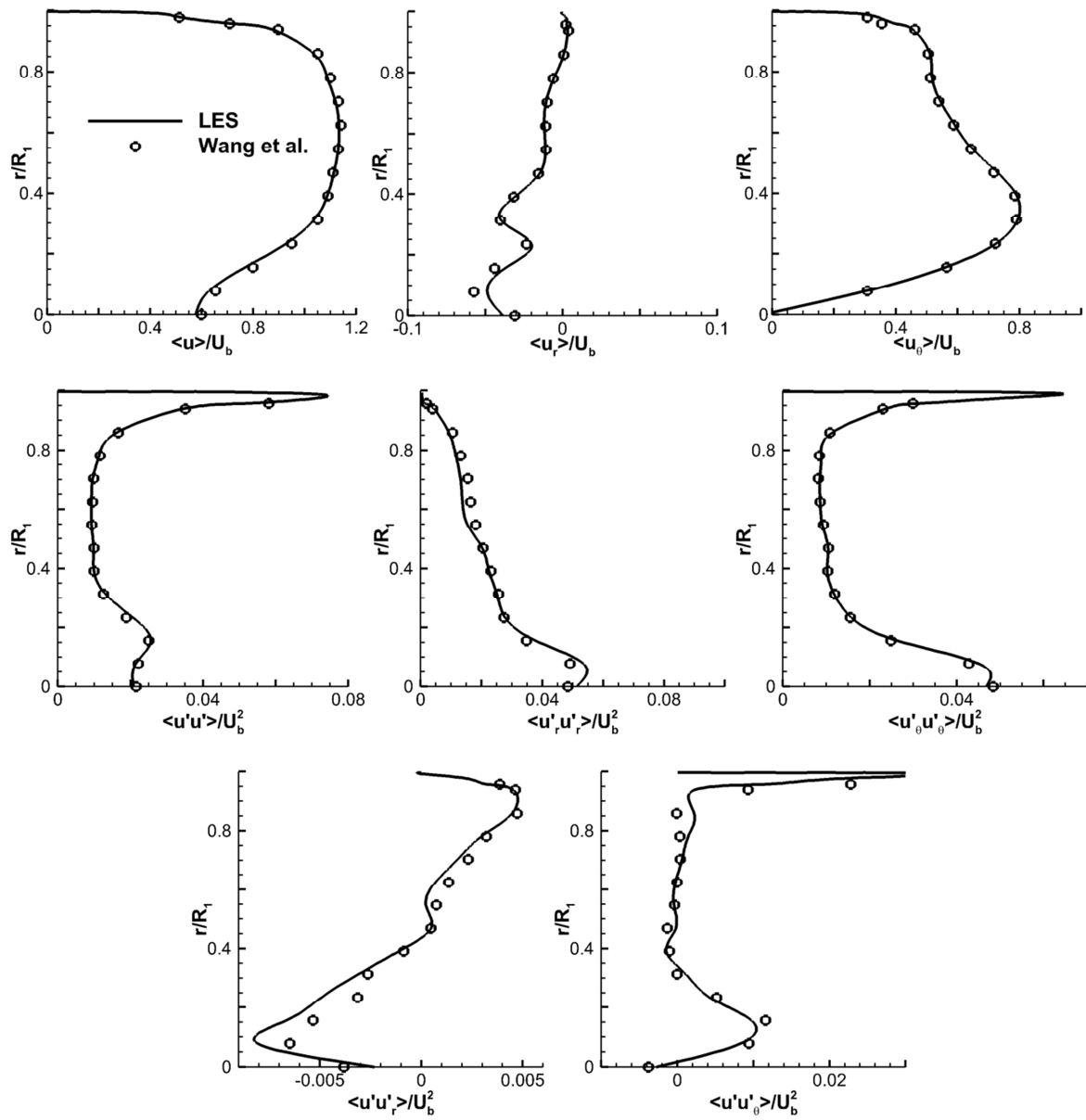
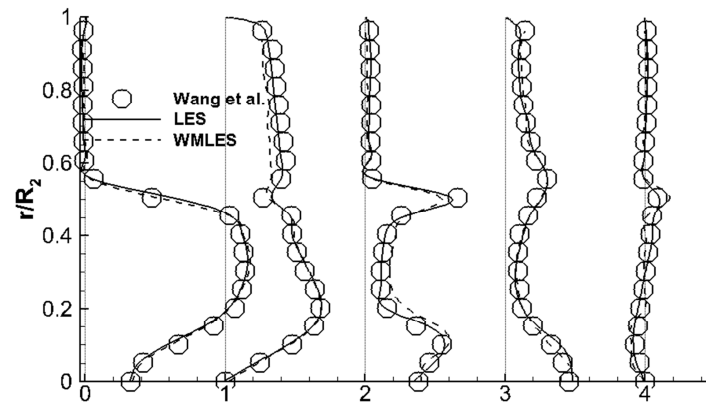
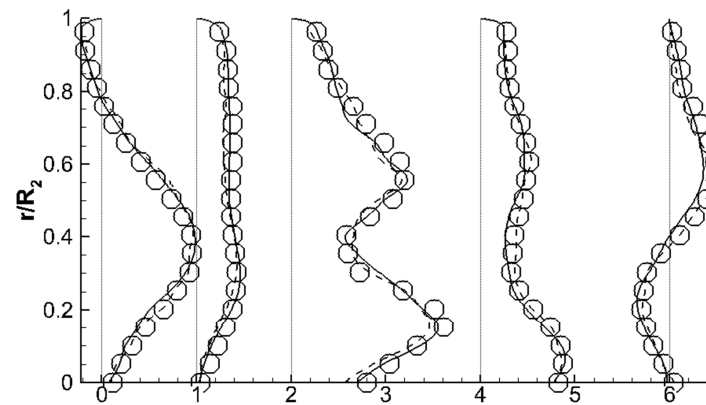


Figure C.1 Measured and predicted mean velocity and turbulent stress profiles normalized by bulk mean velocity at inlet of the computational domain ($x/H=-2.1$) at $Re=10,000$, $S=0.33$



(a)



(b)

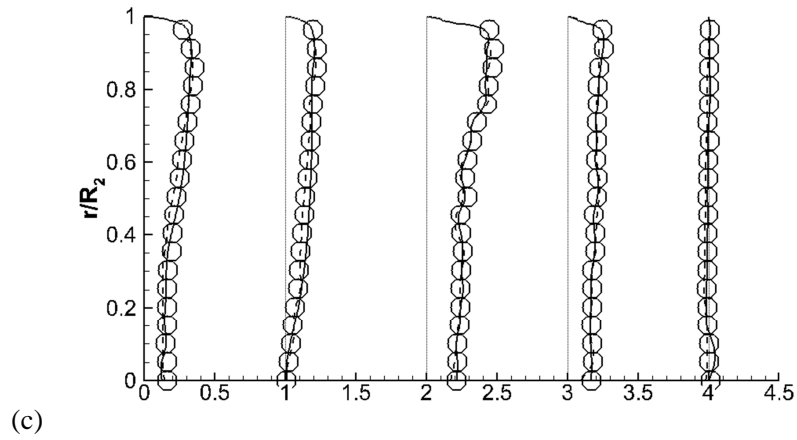


Figure C.2 Time averaged profiles of (from left to right) axial velocity ($\langle u \rangle / U_b$), swirl velocity ($\langle u_\theta \rangle / U_b$), variance of axial velocity ($\langle u' u' \rangle / U_b^2$), variance of swirl velocity ($\langle u'_\theta u'_\theta \rangle / U_b^2$), Reynolds shear stress ($\langle u' u'_r \rangle / U_b^2$) for $Re=10,000$ and $S=0.33$ at (a)

$$\frac{x}{h} = 0.17, \text{ (b) } \frac{x}{h} = 2.1, \text{ and (c) } \frac{x}{h} = 6.3$$

(Reynolds stresses are scales up by a factor of 10)

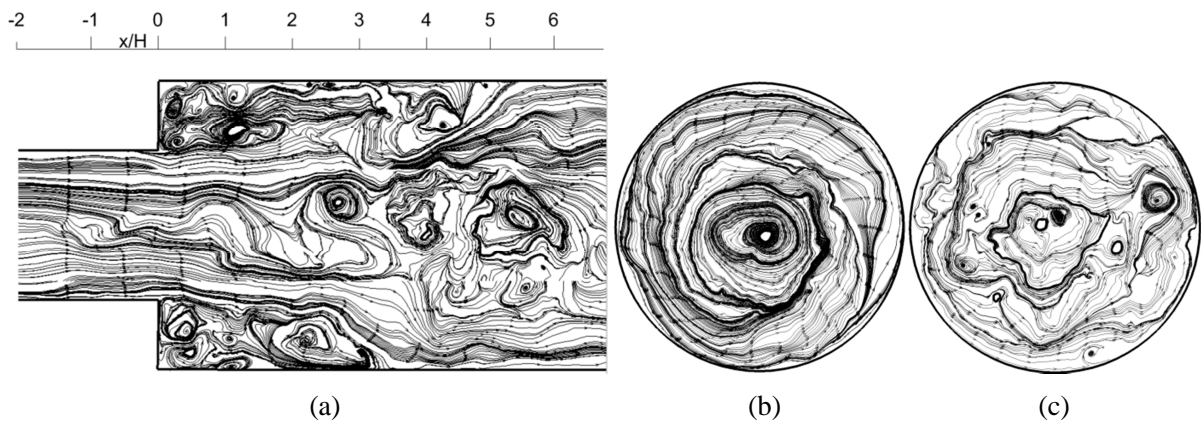


Figure C.3 Instantaneous streamlines ($Re=10,000$ $S=0.33$) in, (a) azimuthal plane ($z/H=0$), (b) $x/H=1$, and (c) $x/H=5$

Appendix D

Detailed Flow Predictions in Experimental Swirl Combustor

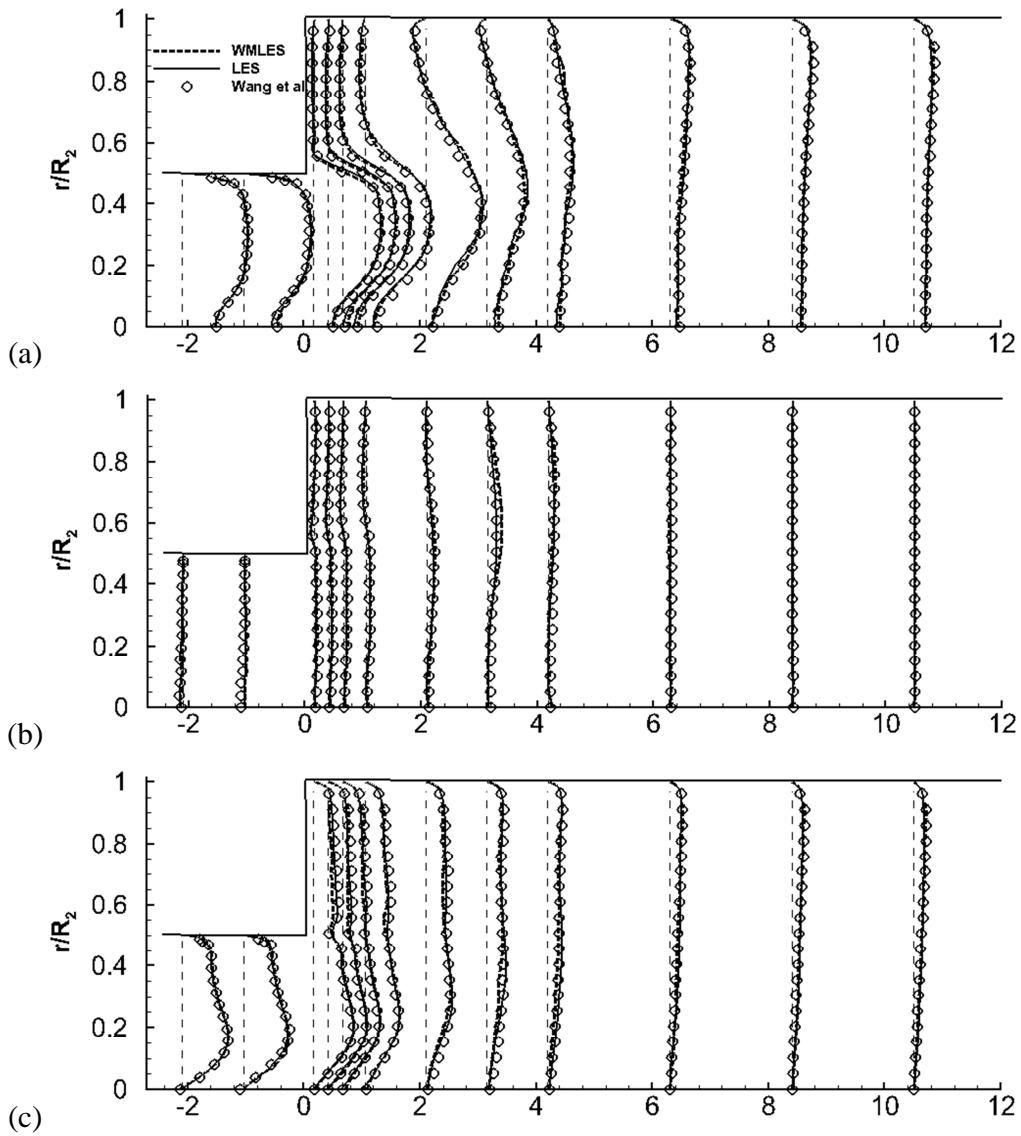


Figure D.1 Time averaged normalized mean velocity profiles at various streamwise locations ($Re=10,000$ $S=0.33$), (a) axial velocity $\langle u \rangle / U_b$, (b) radial velocity $\langle u_r \rangle / U_b$, (c) circumferential velocity $\langle u_\theta \rangle / U_b$

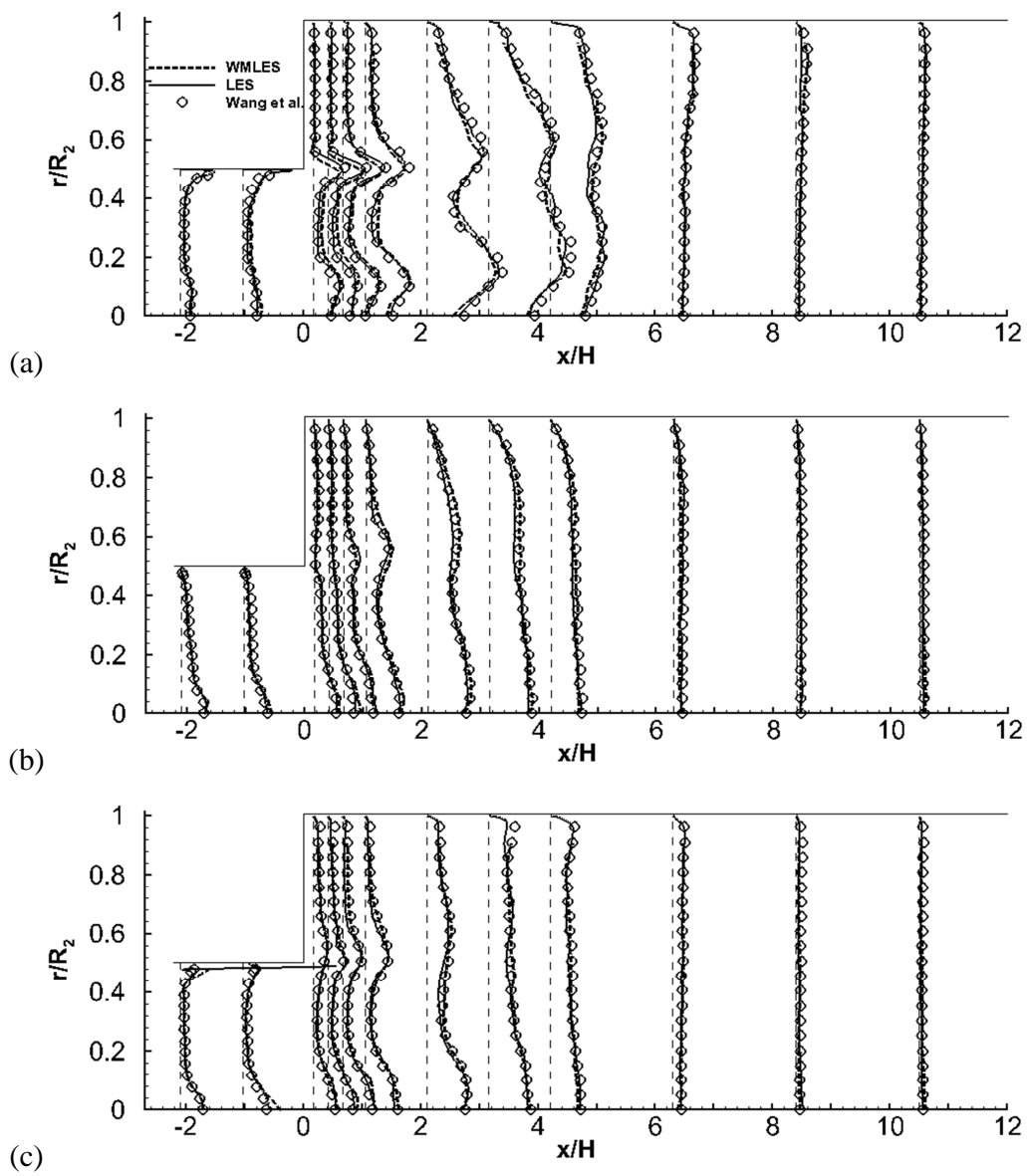


Figure D.2 Time averaged normalized profiles of variances of velocity components at various streamwise locations ($Re=10,000$ $S=0.33$) (a) $\langle u'u' \rangle / U_b^2$, (b) $\langle u_r'u_r' \rangle / U_b^2$, (c) $\langle u_\theta'u_\theta' \rangle / U_b^2$, (scale=1:8)

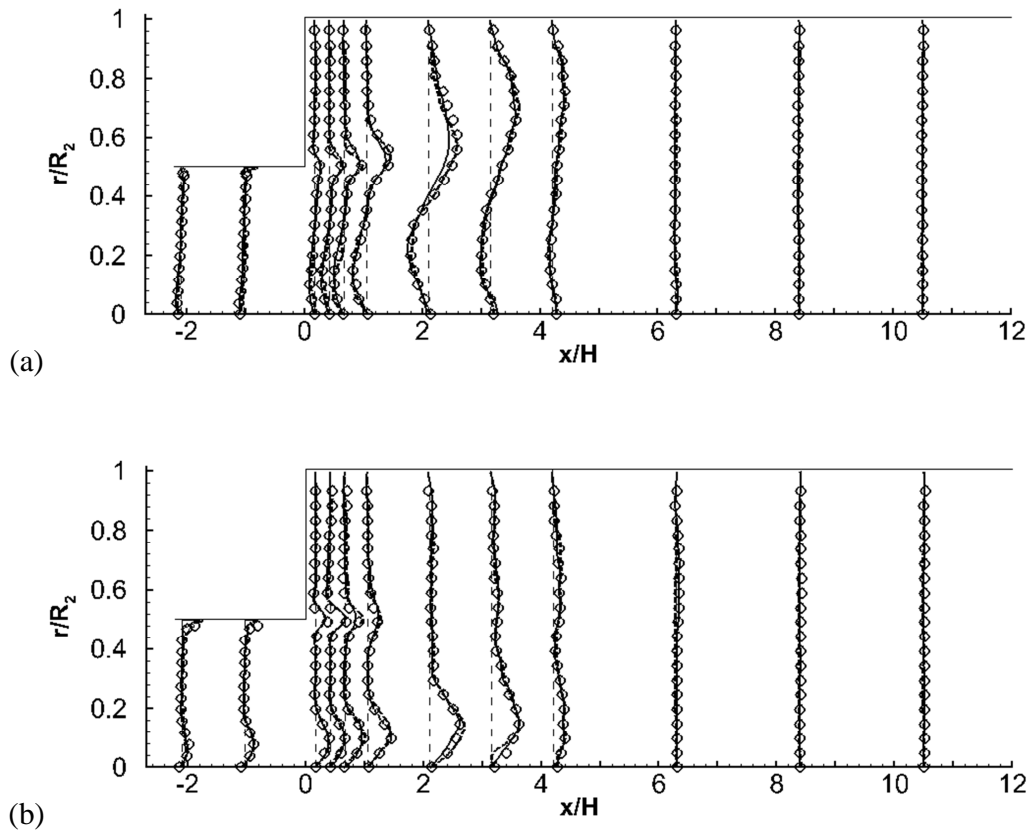


Figure D.3 Time averaged Reynolds shear stress profiles at various streamwise locations

($Re=10,000$ $S=0.33$), (a) $\langle u'u'_r \rangle / U_b^2$, (b) $\langle u'u'_\theta \rangle / U_b^2$, (scale=1:10)

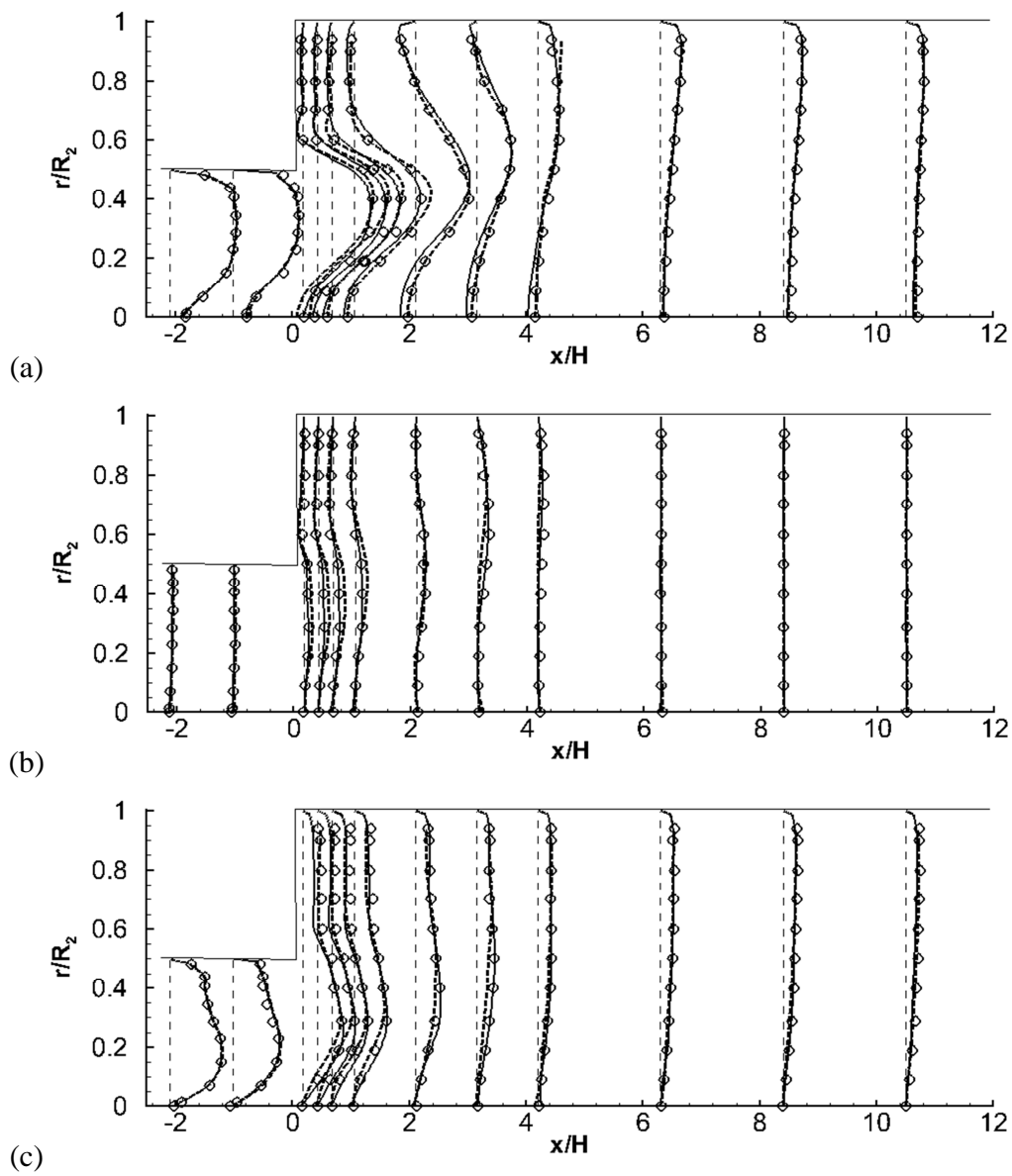


Figure D.4 Time averaged normalized mean velocity profiles at various streamwise locations ($Re=20,000$ $S=0.43$), (a) axial velocity $\langle u \rangle / U_b$, (b) radial velocity $\langle u_r \rangle / U_b$, (c) circumferential velocity $\langle u_\theta \rangle / U_b$

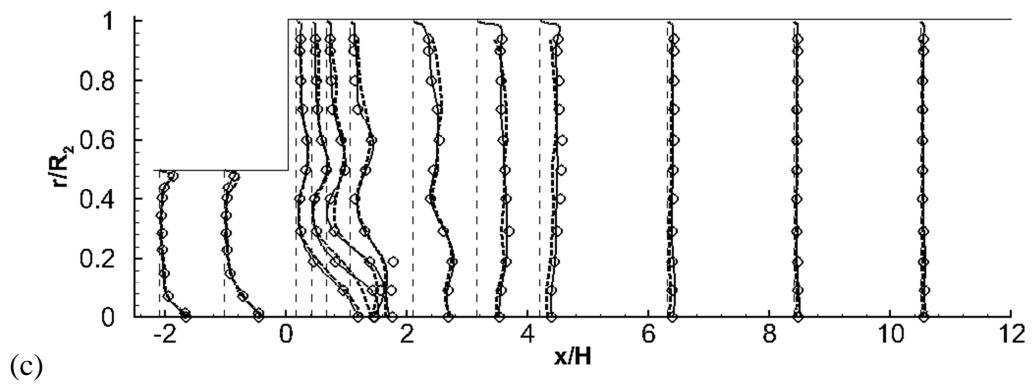
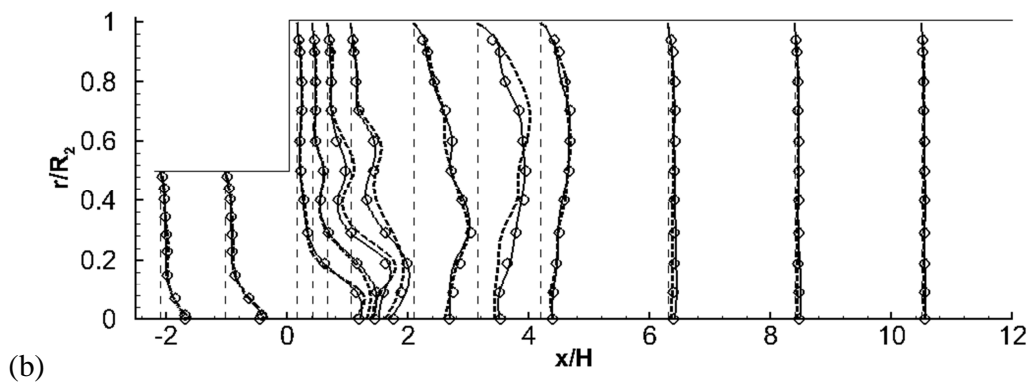
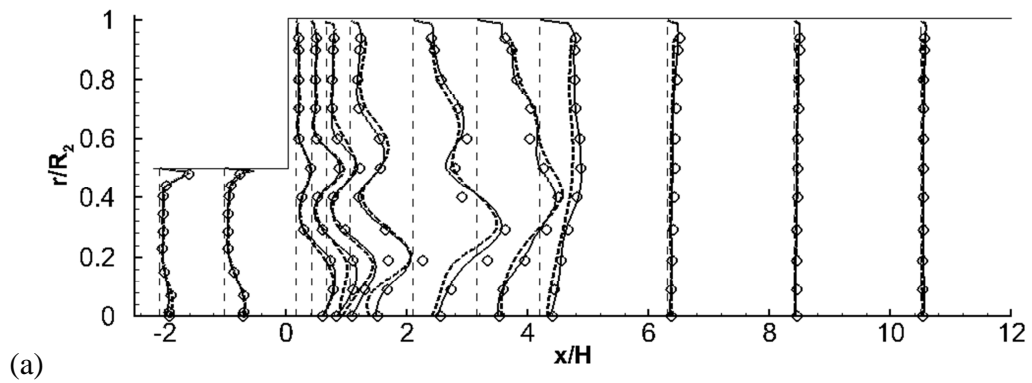


Figure D.5 Time averaged normalized profiles of variances of velocity components at various streamwise locations (Re=20,000 S=0.43) (a) $\langle u' u' \rangle / U_b^2$ (b) $\langle u_r' u_r' \rangle / U_b^2$ (c) $\langle u_\theta' u_\theta' \rangle /$

$$U_b^2 \text{ (scale=1:8)}$$

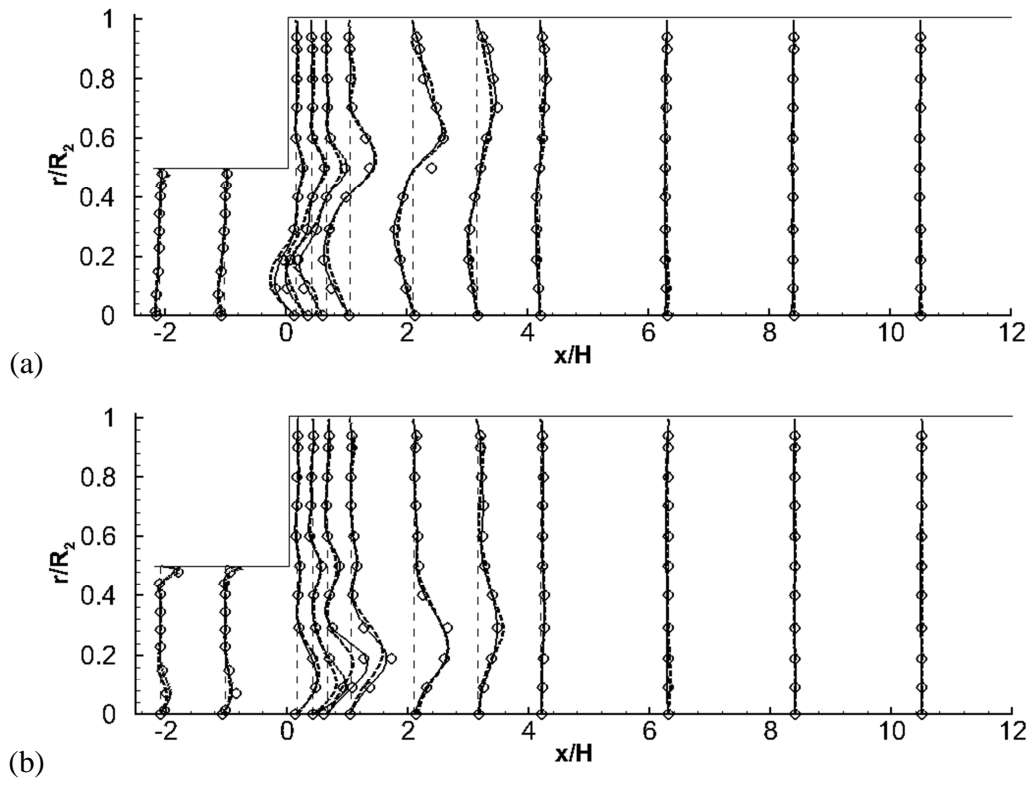
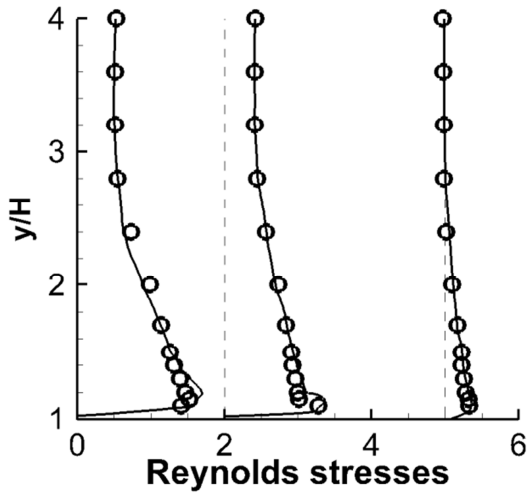


Figure D.6 Time averaged Reynolds shear stress profiles at various streamwise locations

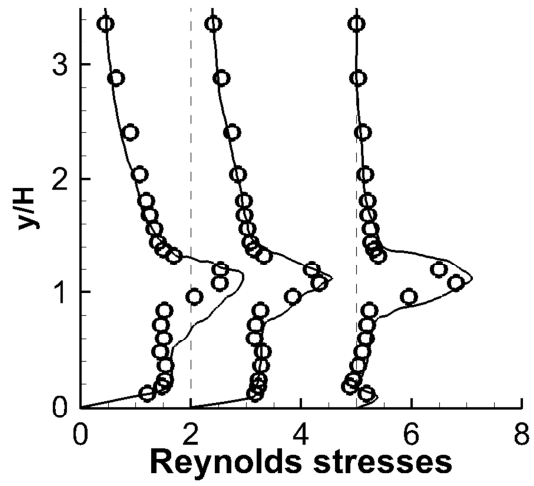
(Re=20,000 S=0.43) (a) $\langle u'u'_r \rangle / U_b^2$ (b) $\langle u'u'_\theta \rangle / U_b^2$ (scale=1:10)

Appendix E

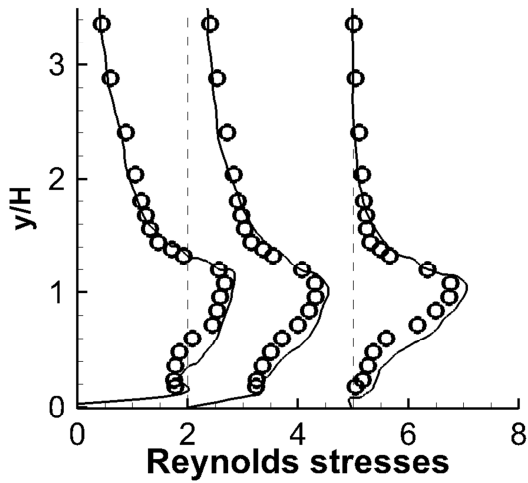
Additional Flow Predictions in Backward Facing Step



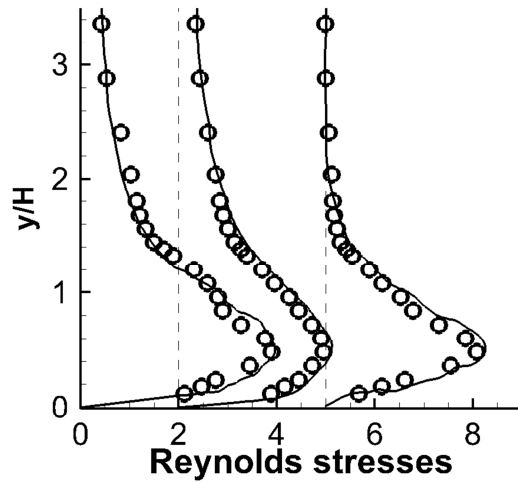
(a)



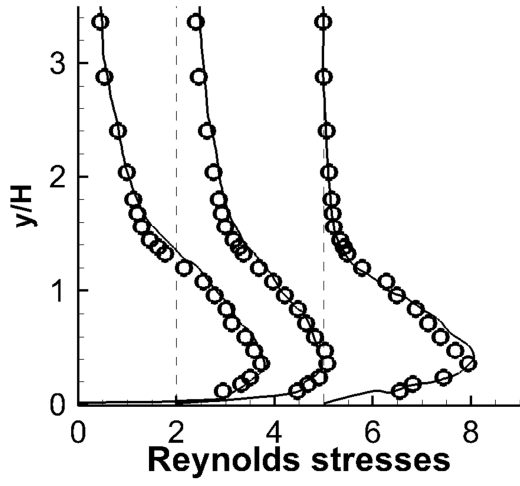
(b)



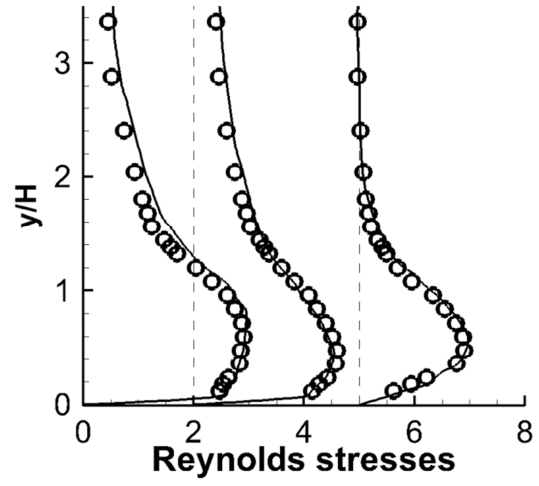
(c)



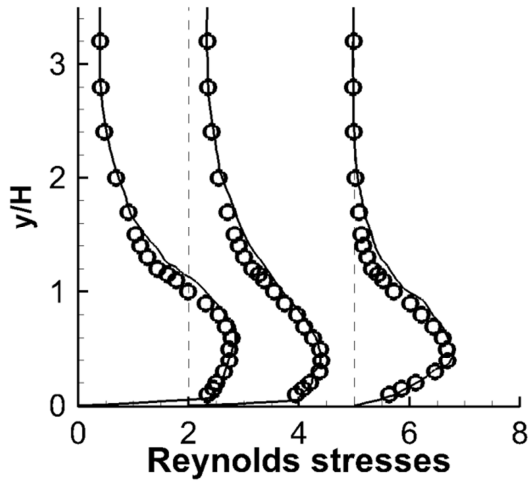
(d)



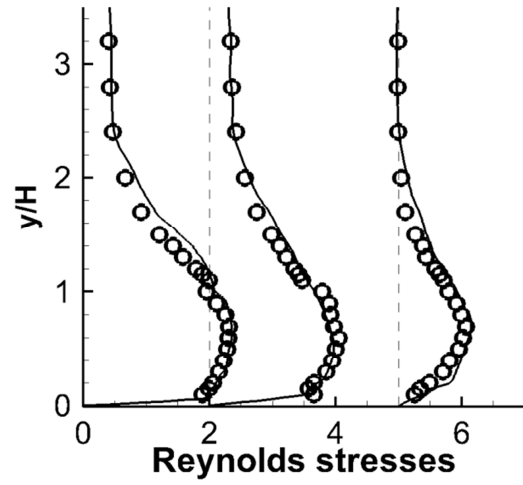
(e)



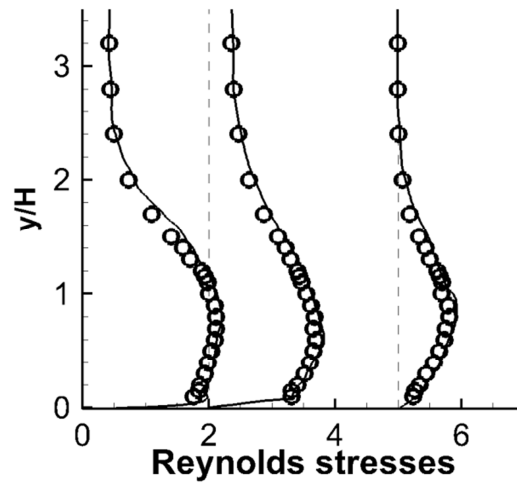
(f)



(g)



(h)



(i)

Figure E.1 Time averaged normalized profiles of variances of velocity components at various streamwise locations (a) $x/H=0$ (b) $x/H=1$ (c) $x/H=2$ (d) $x/H=4$ (e) $x/H=5$ (f) $x/H=7$ (g) $x/H=8$ (h) $x/H=12$ (i) $x/H=16$

(From left to right u_{rms} (scale 1: 30), v_{rms} (scale 1: 30), $u'v$ (scale 1: 500)')

Appendix F

Simulation Code GenIDLEST

The code GenIDLEST (Generalized Incompressible Direct and Large Eddy Simulation of Turbulent flows) has been applied and validated in a number of turbulent flows ranging from canonical geometries to complex configurations. Some examples calculations are: turbulent channel flow, separating and reattaching flows, DNS of transitional vorticity dynamics in complex fin configurations in compact heat exchangers, LES of high Reynolds number turbine blade internal cooling applications and LES of leading edge film cooling. Some important elements of the software are summarized below.

- Hybrid structured mesh with unstructured block topology. Capability to handle non-matching block interfaces, which allow local refinement in blocks and zonal embedding of grids in critical regions.
- Can be used for RANS, URANS, LES, DNS and hybrid LES-URANS or DES.
- Moving dynamic meshes with spring analogy and trans-finite interpolation (TFI) for mesh redistribution under large displacements.
- Structural membrane model coupled to the fluid solver
- Dispersed Phase modeling capability.
- Conjugate Heat Transfer modeling capability.
- Discretizations range from second-order central difference, to third-order upwind biased or QUICK which can be used with or without limiters.

- Dynamic Smagorinsky Model for subgrid stress modeling in LES calculations
- RANS models based on the $k-\omega$ model and Menter's baseline and shear stress transport models are implemented.
- LES wall models for calculations of high Reynolds number wall bounded flows.
- Synthetic Eddy Method for specifying inlet turbulence boundary condition.
- Range of boundary conditions: periodic, walls with blowing or suction, constant temperature or flux boundary conditions, inlet, outflow, symmetry, and pressure boundary conditions.
- Modified equations for fully-developed flow and heat transfer assumptions.
- Solid blockages with no-slip, blowing, suction, constant temperature or flux boundary conditions can be interspersed in the computational domain.
- Scalable linear systems solver based on Krylov Methods, CG for symmetric systems and BiCGSTAB and GMRES(m) for non-symmetric. Multi-level additive/multiplicative Schwarz preconditioners are available with Jacobi, SSOR, and Stones strongly Implicit method (similar to ILU(0)) relaxers in each cache block.
- Tools for extracting mean and turbulent statistics; vortex extraction and identification techniques based on the $\nabla \bar{u}$ and λ_2 method are also available.
- Highly parallelizable and scalable to 100's of processors for quick turnaround times on high fidelity computations.

Bibliography

- [1] Chin J., Skirvin S., Hayes L., and Burggraf F., 1961. "Film cooling with multiple slots and louvers – Part 1: Multiple continuous slots," *Journal of Heat Transfer*, **83**, 281-286.
- [2] Metzger D., Takeuchi D., and Kuenstler P., 1973. "Effectiveness and heat transfer with full-coverage film cooling," *Journal of Engineering for Power*, **95**, 180-184.
- [3] Andrews G. E., Khalifa I. M., Asere A. A., and Bazdidi-Tehrani F., 1995. "Full coverage effusion film cooling with inclined holes," Paper 95-GT-274, IGTI Turbo Expo, Houston.
- [4] Fric T. F., Campbell R. P., and Rettig M. G., 1997. "Quantitative visualization of full-coverage discrete-hole film cooling," Paper 97-GT-328, IGTI Turbo Expo, Orlando.
- [5] Schulz A., 2001. "Combustor liner cooling technology in scope of reduced pollutant formation and rising thermal efficiencies," In *Heat Transfer in Gas Turbine Systems*, *Annals of the New York Academy of Sciences*, **934**, 135-146.
- [6] Arellano L., Smith K., and Fahme A., 2001. "Combined back side cooled combustor liner and variable geometry injector technology," ASME Paper 2001-GT-0086.
- [7] Smith K. and Fahme A., 1999. "Backside cooled combustor liner for lean-premixed combustion," Paper 99-GT-239, IGTI Turbo Expo, Indianapolis.
- [8] Smith K. O., Angello L. C., and Kurzynske F. R., 1986. "Design and testing of an ultra-low NO_x gas turbine combustor," ASME Paper 86-GT-263, 1986.

- [9] Smith K. O., Holsapple A. C., Mak H. H., and Watkins L., 1991. "Development of a natural gas-fired, ultra-low NO_x can combustor for a 800kW gas turbine," ASME Paper 91-GT-303.
- [10] Smith K. O., and Cowell L. H., 1989. "Experimental evaluation of liquid fuel, lean premixed gas turbine combustor," ASME Paper 89-GT-264.
- [11] Vandervort C.L., 2000. "9 PPM NO_x/CO combustion system for "F" class industrial gas turbines", ASME Paper 2000-GT-0086.
- [12] White D. J., Batakis A., Le Cren R., and Yacabucci H., 1982. "Low NO_x combustion systems for burning heavy residual fuels and high fuel-bound nitrogen fuels," Journal of Engineering Turbines and Power, **104**, 377-385.
- [13] Roberts P. B., Kubasco A. J., and Sekas N. J., 1982. "Development of a low NO_x Lean premixed annular combustor", Journal of Engineering Turbines and Power, **104**, 28-35.
- [14] Behrendt T., and Hassa C., 2008. "A test rig for investigations of gas turbine combustor cooling concepts under realistic operating conditions," Journal of Aerospace Engineering, **222**, 169-177.
- [15] Lu Y., Esposito E., and Ekkad S.V., 2008. "Predictions of flow and heat transfer in low emission combustors," Heat Transfer Engineering, **29**, 375-384.
- [16] Gore R. W., and Ranz W. E., 1964. "Backflow in rotating fluids moving axially through expanding cross sections," A.I.Ch.E. Journal, **10**, 83-88.
- [17] Chigier N., and Chervinsky A., 1967. "Experimental investigation of swirling vortex motion in jets," Transactions of ASME, Journal of Applied Mechanics, **34**, 443-450.

- [18] Brum R. D., and Samuelson G. S., 1987. "Two-component laser Anemometry measurements of non-reacting and reacting complex flows in a swirl-stabilized model combustor," *Experiments in Fluids*, **5**, 95-102.
- [19] Vu B. T., and Gouldin F. C., 1982. "Flow measurement in a model swirl combustor," *AIAA Journal*, **20**, 642-651.
- [20] Rhode D. L., Lilley D. G., and McLaughlin D. K., 1983. "Mean flow-fields in axisymmetric combustor geometries with swirl," *AIAA Journal*, **21**, 593-600.
- [21] Ferrell G. B., Abujelala M. T., Busnaina A. A., and Lilley D.G., 1984. "Lateral jet injection into typical combustor flow-fields," *AIAA Paper 84-0374*, 22nd Aerospace Sciences Meeting, Reno, Nevada.
- [22] Bailey J. C., Intile J., Fric T. F., Tolpadi A. K., Nirmalan N. V., and Bunker R. S., 2003. "Experimental and numerical study of heat transfer in a gas turbine combustor liner," *ASME Journal of Engineering for Gas Turbines and Power*, **125**, 994-1002.
- [23] Raj T., and Ganeshan V., 2008. "Study on the effect of various parameters on flow development behind vane swirlers," *International Journal of Thermal Sciences*, **47**, 1204-1225.
- [24] Fernando F., Grinstein T., Young R., Gutmark E., Li G., Hsiao G., and Mongia H., 2002. "Flow dynamics in a swirl combustor," *Journal of Turbomachinery*, **3**, 1-19.
- [25] Grinstein F., and Fureby C., 2005. "LES studies of the flow in a swirl gas combustor," *Proceedings of Combustion Institute*, **30**, 1791-1798.

- [26] Paik, J., and Sotiropoulos F., 2010. "Numerical simulation of strongly swirling turbulent flows through an abrupt expansion," *International Journal of Heat and Fluid Flow*, **31**, 390-400.
- [27] FLUENT 6.3 User's Guide. Fluent Inc., 2007.
- [28] Goh Y., 2006. "Heat transfer and flow characteristics inside a gas turbine combustor," MS Thesis, Department of Mechanical Engineering, Louisiana State University.
- [29] Germano M., Piomelli U., Moin P., and Cabot W., 1991. "A dynamic subgrid-scale eddy viscosity model," *Physics of Fluids A*, **3**, 1760-1765.
- [30] Lilly D. K., 1992. "A proposed modification of the Germano subgrid scale closure method," *Physics of Fluids*, **A4**, 633-635.
- [31] Najjar F., and Tafti D. K., 1996. "Study of discrete test filters and finite difference approximations for the dynamic subgrid-scale stress model," *Physics of Fluids*, **8(4)**, 1076-1088.
- [32] Tafti D. K., 2010. "Time-accurate techniques for turbulent heat transfer analysis in complex geometries, *Advances in Computational Fluid Dynamics and Heat Transfer*;" Eds: Ryo Amano and Bengt Sundén, Series: *Developments in Heat Transfer*, WIT PRESS, Southampton, UK, in press.
- [33] Tafti D. K., 2001. "GenIDLEST—A scalable parallel computational tool for simulating complex turbulent flows," In: *Proceedings of the ASME Fluids Engineering Division, FED, ASME-IMECE, November 2001, New York*.

- [34] Chapman D. R., 1979. "Computational aerodynamics, development and outlook," *AIAA Journal*, **17**, 1293–313.
- [35] Deardorff J. W., 1970. "A numerical study of three-dimensional turbulent channel flow at large Reynolds numbers," *Journal of Fluid Mechanics*, **41**, 453–480.
- [36] Schumann U., 1975. "Subgrid-scale model for finite difference simulation of turbulent flows in plane channels and annuli," *Journal of Computational Physics*, **18**, 376–404.
- [37] Grotzbach G., 1987. "Direct numerical and large eddy simulation of turbulent channel flows," In *Encyclopedia of Fluid Mechanics*, ed. NP Cheremisinoff, 1337–91, West Orange, NJ: Gulf Publications.
- [38] Werner H., and Wengle H., 1993. "Large-eddy simulation of turbulent flow around a cube in a plane channel," In *Selected Papers from the 8th Symposium on Turbulent Shear Flows*.
- [39] Piomelli U., Moin P., Ferziger J., and Kim J., 1989. "New approximate boundary conditions for large-eddy simulations of wall-bounded flows," *Physics of Fluids A*, **101**, 61–68.
- [40] Hoffmann G., and Benocci C., 1995. "Approximate wall boundary conditions for large-eddy simulations," In: Benzi, R. (Ed.), *Advance in Turbulence V*, 222–228.
- [41] Temmerman L., Leschziner M. A., and Hanjalic K., 2002. "A-priori studies of a near-wall RANS model within a hybrid LES/RANS scheme," In: Rodi, W., Fueyo, N. (Eds.), *Engineering Turbulence Modelling and Experiments*, Elsevier, 317–326.

- [42] Spalart P. R., Jou W. H., Strelets M., and Allmaras S. R., 1997. "Comments on the feasibility of LES for wings and on a hybrid RANS/LES approach," *Advances in DNS/LES*, 137–48, Columbus, OH.
- [43] Strelets M., 2001. "Detached Eddy Simulation of Massively Separated Flows," AIAA paper 2001-0879, 39th AIAA Aerospace Sciences Meeting and Exhibit, 2001.
- [44] Spalart P., and Allmaras S., 1994, "A one-equation turbulence model for aerodynamic flows," *La Recherche Aérospatiale*, **1**, 5-21.
- [45] Lyons D. C., Peltier L. J., Zajaczkowski F. J., and Paterson E. G., 2009. "Assessment of DES models for separated flow from a hump in a turbulent boundary layer," *Journal of Fluids Engineering*, **131**, 111-203.
- [46] Saric S., Kniesner B., Mehdizadeh A., Jakirlic S., Hanjalic K., and Tropea C., 2008. "Comparative assessment of Hybrid LES/RANS models in turbulent flows separating from smooth surfaces," In: *Advances in Hybrid RANS-LES Modelling, Notes on Numerical Fluid Mechanics and Multidisciplinary Design*, **97**, S.-H. Peng and W. Haase (Eds.), Springer-Verlag, Berlin, 142-151.
- [47] Viswanathan A.K., and Tafti D.K., 2007. "Capturing the effects of rotation in sudden expansion ducts using Detached Eddy Simulation," *AIAA Journal*, **45(8)**, 2100-2102.
- [48] Viswanathan A.K., and Tafti D.K., 2006, "A comparative study of DES and URANS for flow prediction in a two-pass internal cooling duct," *ASME Journal Fluids Engineering*, **128(6)**, 1336-1345.

- [49] Viswanathan A.K., and Tafti D.K., 2006. "Detached eddy simulation of turbulent flow and heat transfer in a two-pass internal cooling duct," *International Journal of Heat and Fluid Flow*, **27(1)**, 1-20.
- [50] Balaras E., and Benocci C., 1994. "Subgrid-scale models in finite-difference simulations of complex wall bounded flows," AGARD CP 551, 2.1–2.5, Neuilly-Sur-Seine, France: AGARD.
- [51] Balaras E., Benocci C., and Piomelli U., 1996. "Two layer approximate boundary conditions for large-eddy simulations," *AIAA Journal*, **34**, 1111–1119.
- [52] Cabot W., and Moin P., 1999. "Approximate wall boundary conditions in the large eddy simulation of high Reynolds number flow," *Flow, Turbulence and Combustion*, **63**, 269–291.
- [53] Wang M., and Moin, P., 2002. "Dynamic wall modeling for large-eddy simulation of complex turbulent flows," *Physics of Fluids*, **14 (7)**, 2043–2051.
- [54] Tessicini F., Li N., and Leschziner M. A., 2007. "Large-eddy simulation of three-dimensional flow around a hill-shaped obstruction with a zonal near-wall approximation," *International Journal of Heat and Fluid Flow*, **28**, 894-908.
- [55] Kays W. M., 1992. "Turbulent Prandtl number – where we are?," Max Jacobs Memorial Award Lecture, 1-12.
- [56] Kaltenbach H., Fatica M., Mittal R., Lund T.S., and Moin P., 1999. "Study of flow in a planar asymmetric diffuser using large-eddy simulation," *Journal of Fluid Mechanics*, **390**, 151-185.

- [57] Friedrich R., and Arnal M., 1990. "Analyzing turbulent backward-facing step flow with the lowpass-filtered Navier-Stokes equation," *Journal of Wind Engineering and its Applications*, **35**, 101-128.
- [58] Rozati A., and Tafti D. K., 2008. "Large-eddy simulation of leading edge film cooling," *Journal of Turbomachinery*, **130**, 1-7.
- [59] Lund T., Wu X., and Squires D., 1998. "Generation of turbulent inflow data for spatially-developing boundary layer simulations," *Journal of Computational Physics*, **140**, 233-258.
- [60] Aider J., and Danet A., 2006. "Large-eddy simulation study of upstream boundary condition influence upon a backward-facing step flow," *Comptes Rendus Mecanique*, **334**, 447-453.
- [61] Wang M., and Moin P., 2000. "Computation of trailing-edge flow and noise using large-eddy simulation," *AIAA Journal*, **38**, 2201-2209.
- [62] Sagaut P., Garnier E., Tromeur E., Larcheveque L., and Labourasse E., 2004. "Turbulent inflow conditions for LES of compressible wall bounded flows," *AIAA Journal*, **42(3)**, 469-477.
- [63] Batten P., Goldberg U., and Chakravarthy S., 2004. "Interfacing statistical turbulence closures with large-eddy simulation," *AIAA Journal*, **42(3)**, 485-492.
- [64] Smirnov A., Shi S., and Celik I., 2001. "Random flow generation technique for large-eddy simulations and particle-dynamics modeling," *Journal of Fluids Engineering*, **123**, 359-371.

- [65] Davidson L., 2007. "Using synthetic isotropic fluctuations as inlet boundary conditions for unsteady simulations," *Advances and Applications in Fluid Dynamics*, **1(1)**, 1–35.
- [66] Jarrin N., Benhamadouche S., Laurence D., and Prosser R., 2007. "A synthetic-eddy method for generating inflow conditions for large-eddy simulations," *International Journal of Heat and Fluid Flow*, **27**, 585-593.
- [67] Press W. H., Flannery B. P., Teukolsky S. A., and Vetterling W. T., 1992. "Numerical recipes in FORTRAN : The art of scientific computing," 2nd ed., Cambridge University Press, Cambridge, England.
- [68] Driver D.M., and Seegmiller H.L., 1985. "Features of a reattaching turbulent shear layer in divergent channel flow," *AIAA Journal*, **23(2)**, 163-171.
- [69] Toschi F., Kobayashi H., Piomelli U., and Iaccarino G., 2006. "Backward-facing step calculations using the shear improved Smagorinsky model," *Center for Turbulence Research, Proceedings of the Summer Program 2006*, 87-97.
- [70] Avancha R., and Pletcher R., 2002. "Large eddy simulation of the turbulent flow past a backward-facing step with heat transfer and property variations," *International Journal of Heat and Fluid Flow*, **23(5)**, 601-614.
- [71] Chan D. C., and Mittal R., 1996. "Large eddy simulation of backward facing step flow using least square spectral element method," *Proceedings of Summer Program 1996, Center for Turbulence Research*, 1-12.
- [72] Neumann J., and Wengle H., 2002. "DNS and LES of passively controlled turbulent backward-facing step flow," *Flow, Turbulence and Combustion*, **71(1)**, 297-310.

- [73] Dejoan A., and Leschziner M. A., 2004. "Large eddy simulation of periodically perturbed separated flow over a backward-facing step," *International Journal of Heat and Fluid Flow*, **25(4)**, 581-592.
- [74] Jovic S., and Driver D. M., 1994. "Backward-facing step measurement at low Reynolds number, $Re_H = 5000$," NASA Tech. Mem. 108807.
- [75] Kasagi N., and Matsunaga A., 1995. "Three-dimensional particle-tracking velocimetry measurement of turbulences statistics and energy budget in a backward-facing step flow," *International Journal of Heat and Fluid Flow*, **16**, 477-485.
- [76] Kim J., Moser R., and Mansour N., 1989. "Direct numerical simulation of turbulent channel flow up to $Re_\tau = 590$," *Physics of Fluids*, **11(4)**, 943-945.
- [77] Piomelli U., 1993. "High Reynolds number calculations using the dynamic subgrid-scale stress model," *Physics of Fluids A*, **5**, 1484-1490.
- [78] Wilcox D. C., 2002. "Turbulence modeling for CFD," DCW industries, Second Edition.
- [79] Simpson R. L., 1989. "Turbulent boundary-layer separation," *Annual Review of Fluid Mechanics*, **21**, 205-234.
- [80] Yoder D. A., and Georgiadis N. J., 1999. "Implementation and Validation of the Chien k-epsilon Turbulence Model in the WIND Navier-Stokes Code," AIAA Paper 99-0745.
- [81] Wang P., Bai X., Wessman M., and Klingmann J., 2004. "Large eddy simulation and experimental studies of a confined turbulent swirling flow," *Physics of Fluids*, **16(9)**, 3306-3324.

- [82] Patil S., Abraham S., Tafti D., Ekkad S., Kim Y., Dutta P., Moon H., and Srinivasan R., 2011. "Experimental and numerical investigation of convective heat transfer in gas turbine can combustor," *Journal of Turbomachinery*, **133**(1).
- [83] Gupta A. K., Lilley D. G., and Syred N., 1984. "Swirl flows," ABACUS press.
- [84] Sloan D. G., Smith P. J., and Smoot L.D., 1986. "Modeling of swirl in turbulent flow systems," *Progress in Energy Combustion Science*, **12**, 163-250.
- [85] Syred, N., and Beer, J. M., 1974. "Combustion in swirling flows : A review," *Combustion and Flame*, **23**, 143-201.
- [86] Starkey P. A., and Yim M. J., 2007. " Experimental and numerical investigation of a swirl stabilized premixed combustor under cold-flow conditions," *Journal of Fluids Engineering*, **129**, 942-953.
- [87] Nejad A. S., Vanka S. P., and Favaloro S. C., 1989. "Application of laser velocimetry for characterization of confined swirling flow," *Journal of Engineering Gas Turbines Power*, **111**(1), 36-45.
- [88] Weber R., Visser B. M., and Boysan F., 1990. "Assessment of turbulence modeling for engineering prediction of swirling vortices in the near burner zone," *International Journal of Heat and Fluid Flow*, **11**(3), 225-235.
- [89] Kitoh O., 1991. "Experimental study of turbulent swirling flow in a straight pipe," *Journal of Fluid Mechanics*, **225**, 445-479.
- [90] Ahmed S. A., 1998. "Velocity measurements and turbulence statistics of a confined isothermal swirling flow," *Experimental Thermal Fluid Sciences*, **17**, 256-264.

- [91] Kubo I., and Gouldin F. G., 1975. "Numerical calculations of turbulent swirling flow," *Journal of Fluids Engineering*, **97**, 310-315.
- [92] Sharif M. A. R., and Wong Y. K. E., 1995. "Evaluation of the performance of three turbulence closure models in the prediction of confined swirling flows," *Computers and Fluids*, **24**, 81-100.
- [93] Xia J. L., Yadigaroglu G., Liu Y. S., Schmidli J., and Smith B. L., 1998. "Numerical and experimental study of swirling in a model combustor," *International Journal of Heat and Mass Transfer*, **41**, 1485-1497.
- [94] Jakirlic S., Volkert J., Pascal H., Hanjalic K., and Tropea C., 2000. "DNS, experimental and modeling study of axially compressed in-cylinder swirling flow," *International Journal of Heat and Fluid Flow*, **21(5)**, 627-369.
- [95] Wang S., Yang V., Hsiao G., Hsieh S., and Mongia H., 2007. "Large-eddy simulation of gas-turbine swirl injector flow dynamics," *Journal of Fluid Mechanics*, **583**, 99-122.
- [96] Pierce C. D., and Moin P., 1998. "Large eddy simulation of a confined coaxial jet with swirl and heat release," *AIAA 98-2892*, 29th AIAA Fluid Dynamics Conference, 15–18 June 1998.
- [97] Kim W. W., Menon S., and Mongia H. C., 1999. "Large-eddy simulation of a gas turbine combustor flow," *Combustion Science and Technology*, **143**, 25-62.
- [98] Garcia-Villalba M., and Frohlich J., 2006. "LES of a free annular swirling jet – Dependence of coherent structures on a pilot jet and the level of swirl," *International Journal of Heat and Fluid Flow*, **27**, 911-923.

- [99] Rau G., Cakan M., Moeller D., and Arts T., 1998. "The Effect of periodic ribs on the local aerodynamic and heat transfer performance of a straight cooling channel," ASME Journal of Turbomachinery, **120**, 368–375.
- [100] Han J. C., Park J. S., and Ibrahim M. Y., 1986. "Measurement of heat transfer and pressure drop in rectangular channels with turbulence promoters," NASA report 4015.
- [101] Tafti D. K., 2005. "Evaluating the role of subgrid stress modeling in a ribbed duct for the internal cooling of turbine blades," International Journal of Heat and Fluid Flow, **26**, 92–104.
- [102] Bakken O. M., Krogstad P-A., Shrafian A., and Andersson A., 2005. "Reynolds number effects in the outer layer of the turbulent flow in a channel with rough walls," Physics of Fluids, **17**, 101-117.
- [103] Han J. C., 1984. "Heat transfer and friction in channels with two opposite rib-roughened walls," ASME Journal of Heat Transfer, **106**, 774–781.
- [104] Han J. C., 1988. "Heat transfer and friction characteristics in rectangular channels with rib turbulators," ASME Journal of Heat Transfer, **110**, 321–328.
- [105] Chandra P. R., Han J. C., and Lau S. C., 1988. "Effect of rib angle on local heat/mass transfer distribution in a two-pass rib-roughened channel," ASME Journal of Turbomachinery, **110**, 233–241.
- [106] Lau S. C., McMillan R. D., and Han J. C., 1991. "Turbulent heat transfer and friction in a square channel with discrete rib turbulators," ASME Journal of Turbomachinery, **113**, 360–366.

- [107] Han J. C., and Zhang Y. M., 1991. "Effect of rib-angle orientation on local mass transfer distribution in a three-pass rib-roughened channel," *ASME Journal of Turbomachinery*, **113**, 123–130.
- [108] Han J. C., Zhang Y. M., and Lee C. P., 1992. "Influence of surface heat flux ratio on heat transfer augmentation in square channels with parallel, crossed, and V-shaped angled ribs," *ASME Journal of Turbomachinery*, **114**, 872–880.
- [109] Han J. C., Al-Qahtani M., and Chen H. C., 2002. "A numerical study of flow and heat transfer in rotating rectangular channels with 45° rib turbulators by Reynolds stress turbulence model," In: *Proceedings of the ASME Turbo Expo 2002*, GT-2002-30216.
- [110] Ekkad S. V., and Han J. C., 1997. "Detailed heat transfer distributions in two-pass square channels with rib turbulators," *International Journal of Heat and Mass Transfer*, **40 (11)**, 2525–2537.
- [111] Taslim M. E., Li T., and Spring S. D., 1998. "Measurements of heat transfer coefficients and friction factors in passages rib-roughened on all walls," *ASME Journal of Turbomachinery*, **120**, 564–570.
- [112] Korotky G. J., and Taslim M. E., 1998. "Rib heat transfer coefficient measurements in a rib-roughened square passage," *ASME Journal of Turbomachinery*, **120**, 376–385.
- [113] Taslim M. E., and Lengkong N., 1998. "45° Staggered rib heat transfer coefficient measurements in a square channel," *ASME Journal of Turbomachinery*, **120**, 571–580.
- [114] Taslim M. E., and Korotky G. J., 1998. "Low-aspect ratio rib heat transfer coefficient measurements in a square channel," *ASME Journal of Turbomachinery*, **120**, 831–838.

- [115] Saidi A., and Sunden B., 2001. "On prediction of thermal-hydraulic characteristics of square-sectioned ribbed cooling ducts," *ASME Journal of Turbomachinery*, **123**, 614–620.
- [116] Jia R., Saidi A., and Sunden B., 2002. "Heat transfer enhancement in square ducts with V-shaped ribs of various angles," In: *Proceedings of the ASME Turbo Expo 2002*, Amsterdam, The Netherlands, ASME Paper No. GT-2002-30209.
- [117] Iacovides H., Kelemenis G., and Raisee M., 2003. "Flow and heat transfer in straight cooling passages with inclined ribs on opposite walls: an experimental and computational study," *Experimental Thermal and Fluid Science*, **27**, 283–294.
- [118] Ooi A., Iaccarino G., Durbin P.A., and Behnia M., 2002. "Reynolds averaged simulation of flow and heat transfer in ribbed ducts," *International Journal of Heat and Fluid Flow*, **23**, 750–757.
- [119] Prakash C., and Zerkle R., 1995. "Prediction of turbulent flow and heat transfer in a ribbed rectangular duct with and without rotation," *ASME Journal of Turbomachinery*, **117**, 255–264.
- [120] Jang Y. J., Chen H. C., and Han J. C., 2001. "Flow and heat transfer in a rotating square channel with 45° angled ribs by Reynolds stress turbulence model," *ASME Journal of Turbomachinery*, **123**, 124–132.
- [121] Chen Y., Nikitopoulos D. E., Hibbs R., Acharya S., and Myrum T.A., 2000. "Detailed mass transfer distribution in a ribbed coolant passage with a 180° bend," *International Journal of Heat and Mass Transfer*, **43**, 1479–1492.

- [122] Iacovides H., 1998. "Computation of flow and heat transfer through rotating ribbed passages," *International Journal of Heat and Fluid Flow*, **19**, 393–400.
- [123] Han J. C., Chandra P. R., and Lau S. C., 1988. "Local heat/mass transfer distributions around sharp 180° turns in two-pass smooth and rib roughened channels," *ASME Journal of Heat Transfer*, **110**, 91–98.
- [124] Murata A., and Mochizuki S., 2001. "Comparison between laminar and turbulent heat transfer in a stationary square duct with transverse or angled rib turbulators," *International Journal of Heat and Mass Transfer*, **44**, 1127–1141.
- [125] Abdel-Wahab S., and Tafti D. K., 2004a. "Large eddy simulation of flow and heat transfer in a 90° ribbed duct with rotation: effect of Coriolis and centrifugal buoyancy forces," *ASME Journal of Turbomachinery*, **126**, 627–636.
- [126] Abdel-Wahab S., and Tafti D. K., 2004b. "Large eddy simulation of flow and heat transfer in a staggered 45° ribbed duct," In: *Proceedings of the ASME Turbo Expo 2004*, Vienna, Austria, ASME Paper No. GT2004-53800.
- [127] Sewall E.A., and Tafti D. K., 2004a. "Large eddy simulation of the developing region of a stationary ribbed internal turbine blade cooling channel," In: *Proceedings of the ASME Turbo Expo 2004*, Vienna, Austria, ASME Paper No. GT2004-53832.
- [128] Patil S. S., and Tafti D. K., 2010. "Wall modeled large-eddy simulation of flow over backward facing step with synthetic inlet turbulence," AIAA paper No. 896435, AIAA Aerospace Science meeting, Orlando, FL, USA.

- [129] Krogstad P. A., Andersson, H. I., Bakken O. M., and Ashrafian A., 2005. "An experimental and numerical study of channel flow with rough walls," *Journal of Fluid Mechanics*, **530**, 327–352.
- [130] Rotta J. C., 1962. "Turbulent boundary layers in incompressible flow," In: *Progress in aeronautical sciences*, **2**, 1-220.
- [131] Cebeci T., and Chang K. C., 1978. "Calculation of incompressible rough-wall boundary-layer flows," *AIAA Journal*, **16**, 730-735.
- [132] Schlichting H., 1936. "Experimentelle untersuchung zum rauhgkeitsproblem," *Ingenieur-Archiv* 7 (Band, 1. Heft): 1-34.
- [133] Dvorak F. A., 1969, "Calculation of Turbulent Boundary Layers on Rough Surfaces in Pressure Gradient," *AIAA Journal*, **7(9)**, 1752-1759.
- [134] Simpson R. L., 1973. "A generalized correlation of roughness density effects on the turbulent boundary layer," *AIAA Journal*, **11(2)**, 242-244.
- [135] Krogstad P-A., 1991. "Modification of the van Driest damping function to include the effects of surface roughness," *AIAA Journal*, **29(6)**, 888-894.
- [136] Townsend A. A., 1976. "The structure of turbulent shear flow," Cambridge University Press, Cambridge.
- [137] Acharya M., and Escudier M., 1987. "Turbulent flow over mesh roughness," In: *Turbulent shear flows*, **5**, Berlin: Springer, 176-185.

- [138] Krogstad P-A., Antonia R. A., and Browne L. B., 1992. "Comparison between rough- and smooth-wall turbulent boundary layers," *Journal of Fluid Mechanics*, **245**, 599-617.
- [139] Andreopoulos J., and Bradshaw P., 1981. "Measurements of turbulence structure in the boundary layer on a rough surface," *Boundary-Layer Meteorology*, **20**, 201-213.
- [140] Raupach M. R., 1981. "Conditional statistics of Reynolds stress in rough-wall turbulent boundary layers," *Journal of Fluid Mechanics* **108**, 363-382.
- [141] Christoph G. H., and Pletcher R. H., 1983. "Prediction of Rough-wall skin friction and heat transfer," *AIAA Journal*, **21**, 509-515.
- [142] Taylor R. P., Coleman H. W., and Hodge B. K., 1985. "Prediction on turbulent rough-wall skin friction using a discrete element approach," *ASME Journal of Fluids Engineering*, **107**, 251-257.
- [143] Glikson F., and Aupoix B., 1996. "Modeling of compressible boundary layers over arbitrary rough surfaces," 3rd International Symposium on Turbulence Modeling and measurements, Crete, Greece, May 27-29.
- [144] Leonardi S., Tessicini F., Orlandi P., and Antonia R., 2006. "Direct Numerical and Large-Eddy Simulations of Turbulent Flows over Rough Surfaces," *AIAA Journal*, **44(11)**, 2482-2487.
- [145] Cui J., Patel V.C., and Lin C. L., 2006. "Large-Eddy Simulation of Turbulent Flow in a Channel with Rib Roughness," *International Journal of Heat and Fluid Flow*, **24(3)**, 372-388.

- [146] Perry A. E., Schofield W. H., and Joubert P. N., 1969. "Rough Wall Turbulent Boundary Layers," *Journal of Fluid Mechanics*, **37**, 383-413.
- [147] Juneja A., and Nrasseur J., 1999. "Characteristic of Subgrid-resolved-scale Dynamics in Anisotropic Turbulence, with Application to Rough-wall Boundary Layers," *Physics of Fluids*, **11(10)**, 3054-3068.
- [148] Cui J., Patel V. C., and Lin C., 2003. "Prediction of Turbulent Flow Over Rough Surfaces Using a Force Field in large Eddy Simulation," *Journal of Fluids Engineering*, **125**, 2-9.
- [149] Thomas T. G. and Williams J. R., 1999. "Generation of a Wind Environment for Large-eddy Simulation of Bluff Body Flows," *Journal of Wind Engineering and Industrial Aerodynamics*, **82**, 189-208.
- [150] Moeng C. H., 1984. "A Large-eddy Simulation Model for the study Planetary Boundary Layer Turbulence," *Journal of Atmospheric Science*, **41**, 2052-2062.
- [151] Mason P. J., and Gallen N. S., 1986. "On the Magnitude of the Subgrid-scale Eddy Coefficient in Large-eddy Simulations of Turbulent Channel Flow," *Journal of Fluid Mechanics*, **162**, 439-462.
- [152] Xie Z., Voke P., Hayden P., and Robins A., 2004. "Large-eddy Simulation of Turbulent Flow over a Rough Surface," *Boundary-Layer Meteorology*, **111**, 417-440.
- [153] Dean R. B., 1978. "Reynolds number dependence of skin friction and other bulk flow variables in two-dimensional rectangular duct flow," *Journal of Fluids Engineering*, **100**, 215-223.

- [154] Ligrani P. M., and Moffat R. J., 1986. "Structure of transitionally rough and fully rough turbulent boundary layers," *Journal of Fluid Mechanics*, **162**, 69-98.